# Display and Analysis of Tomographic Reconstructions of Multiple Synthetic Aperture LADAR (SAL) Images

A thesis submitted in partial fulfillment
of the requirements for the degree of
Master of Science in Electrical Engineering

by

Bassirou Seck
B.S.E.E., Wright State University, 2016

2018
Wright State University

Wright State University
GRADUATE SCHOOL

July 26, 2018

I HEREBY RECOMMEND THAT THE THESIS PREPARED UNDER MY SUPERVISION BY Bassirou Seck ENTITLED Display and Analysis of Tomographic Reconstructions of Multiple Synthetic Aperture LADAR (SAL) Images BE ACCEPTED IN PARTIAL FULFILLMENT OF THE REQUIREMENTS FOR THE DEGREE OF Master of Science in Electrical Engineering.

Arnab Shaw, Ph.D.
Thesis Director

Brian D. Rigling, Ph.D.
Chair, Department of Electrical Engineering

Committee on
Final Examination

Arnab Shaw, Ph.D.

Joshua Ash, Ph.D.

Lawrence Barnes, M.S.

Barry Milligan., Ph.D.
Interim Dean of the Graduate School

# ABSTRACT

Seck, Bassirou. M.S.E.E., Department of Electrical Engineering, Wright State University, 2018. *Display and Analysis of Tomographic Reconstructions of Multiple Synthetic Aperture LADAR (SAL) Images.*

Synthetic aperture ladar (SAL) is similar to synthetic aperture radar (SAR) in that it can create range/cross-range slant plane images of the illuminated scatters; however, SAL has wavelengths 10,000x smaller than SAR enabling a relatively narrow real aperture, diffraction limited beam widths. The relatively narrow real aperture resolutions allow for multiple slant planes to be created for a single target with reasonable range/aperture combinations. These multiple slant planes can be projected into a single slant plane projections (as in SAR). It can also be displayed as a 3-D image with asymmetric resolutions, diffraction limited in the dimension orthogonal to the SAL baseline. Multiple images with diversity in angle orthogonal to SAL baselines can be used to synthesize resolution with tomographic techniques and enhance the diffraction limited resolution. The goal of this research is to explore methods to enhance the diffraction limited resolutions with multiple observations and/or multiple slant plane imaging with SAL systems. Specifically, metrics associated with the information content of the tomographic based 3 dimensional reconstructions of SAL intensity imagery will be investigated to see how it changes as a function of number of slant planes in the SAL images and number of elevation observations are varied.

# List of Symbols

## Chapter 2

| | |
|---|---|
| $D_{spot}$ | Illuminating spot size |
| $\theta_x$ | Along-track-cross-range resolution |
| $\theta_y$ | Range Resolution |
| $B$ | Bandwidth |
| $v$ | velocity |
| $\lambda$ | wavelength |
| $\Delta\theta_{az}$ | Azimuth step size |
| $R$ | Range |
| $D_{SA}$ | Synthetic aperture distance |
| $T$ | Time (s) |
| $c$ | speed of light |
| $P_s$ | Signal Power |
| $P_n$ | noise Signal |

## Chapter 3

| | |
|---|---|
| $\theta_{az}$ | Azimuth angle |
| $\theta_{el}$ | Elevation angle |
| $\xi$ | Tilt |
| $D_{LSS}$ | Diffraction limited spot size |
| $D_{lens}$ | Diameter of lens |
| $r$ | Radius of lens |
| $\tau$ | SAL resolution time |
| $a$ | Length of the elliptical IFOV |
| $b$ | Width of the elliptical IFOV |
| $SP_{spacing}$ | Slant plane spacing |
| $SP_{height}$ | Slant plane height |
| $SP_{overlap}$ | Slant plane overlap |
| $Num_D$ | Number of detector |
| $T_x$ | Transmit power |
| $R_x$ | Receive power |
| $\psi$ | Uniformly distribution random phase |
| $S$ | Signal |
| $A$ | Full width half max |
| $\mathcal{F}$ | Fourier Transform |
| $\mathcal{F}^{-1}$ | Inverse Fourier Transform |
| $\bar{n}$ | Number of constant sidelobes |
| $\eta$ | Ratio of the mainlobe over the sidelobes |
| $W_n$ | Noise distribution |
| $\sigma^2$ | Noise variance |
| $\mu$ | Noise mean |
| $I$ | Intensity of the image |
| $M$ | Length of the SAL image |

## Chapter 4

| | |
|---|---|
| $P_\theta$ | Projection angle |

## Chapter 5

| | |
|---|---|
| $I(X,Y)$ | Mutual information between X and Y |
| $H(X)$ | Shannon entropy of X |
| $H(Y)$ | Shannon entropy of Y |
| $H(X,Y)$ | Joint entropy of X and Y |
| $SIM$ | Similarity |
| $JID$ | Joint information density |
| $D(p\|\|q)$ | Kullback-Leibler divergence of p and q |

# Contents

# List of Figures

# List of Tables

# Acknowledgment

I would like to thank my advisors, Dr. Arnab Shaw and Mr. Lawrence Barnes, for their help, guidance, encouragement, and teaching throughout my master program.

I would like to thank the LADAR Branch within the Sensors Directorate of the Air Force Research Laboratory and Leidos for sponsoring this research.

I would like to thank Dr. Rabb, Dr. Dierking and the graduate student team for their help and advice. Finally, I would like to thank my beautiful family for always being there, and encouraging me during difficult times.

I dedicate this work to my father Gora Seck, and my mother Fatou Seck

Dieureudieuf Khadimoul Rassoul

# Chapter 1

# Introduction

Synthetic Aperture Ladar (SAL) is a coherent imaging technique that exploits angular diversity between aperture position and target position to synthesize an aperture much larger than the physical antenna aperture along the baseline created by the angular diversity. It can provide image resolutions beyond the diffraction limit of the real optical aperture up to the diffraction limit of the synthetic aperture for the dimension along the baseline. The dimension orthogonal to the range vector and baseline of the synthetic aperture remains diffraction limited at the physical aperture limit. Baselines can be created through relative motion between the target and aperture or through multiple distributed apertures. The former is a temporal variant of SAL and the latter is the spatial variant. This thesis will address resolution enhancement of temporal SAL's diffraction limited dimension through incoherent tomographic reconstruction.

SAL is the extension of Synthetic Aperture RADAR (SAR) to optical wavelengths. It differs from SAR in scattering phenomenology and changes in wavelength scale the diffraction limits for real and synthetic apertures. As such, it requires much less relative aperture motion (baseline length) due to the scaling of wavelengths. It can support more bandwidth for improved range resolution, and provides more readily interpretable images [1]. In part, the interest in SAL is driven by innovations in high bandwidth modulation of co-

herent Ladar sources and systems including chirped frequency-modulated continuous wave (FMCW) Ladar, coherent pulsed sources, and digital-signal modulation coupled with advanced processing methods that support multiple centimeter to submillimeter- scale-range resolutions [16].

Recent SAL work focuses on reconstructing 3-D images of objects [19]. SAR and temporal SAL produce a slant plane image as a fundamental data product. A range/cross range slant plane image is the projection of the 3-D object into the plane defined by the range vector and baseline. An issue is that the resolution on the cross-tract-cross-range dimension remains diffraction limited. *Diffraction* limit is the minimum angular subtense of two sources that can be distinguished by the sensor and depends on the wavelength of the signal and the spatial sampling of the aperture in the pupil plane of the imaging system [13]. This thesis will measure the information content of a single slant plane image and enhance resolution through multiple diffraction limited slant planes and/or tomographic reconstructions from multiple observations with angular diversity.

In this work, we present methods for enhancing geometric images developed by a SAL imaging system with tomographic synthesis. Point clouds of a facet model are rendered at different collection geometries. The SAL image is generated for each of these point clouds derived from of the 3-D facet model, and a 3-D tomographic reconstruction from a series of SAL images with elevation diversity is generated for both the single, and multiple slant plane SAL images to enhance the resolution in the diffraction limited (cross-track-cross-range) dimension. To quantify the information content of the 3-D reconstructed SAL images, we utilize mutual information and joint information density as a basis for a metric. Mutual information is a technique for measuring the similarity between two random variables, in this case two images. Joint information density measures the amount of useful information in the image. The similarity based on the mutual information between a reference image and the reconstructed images is measured, and analyzed to determine the efficacy of the reconstructed image.

## 1.1 Motivation

Slant plane images suffer from the compression of cross track cross range scatterers into the image plane. This may limit the performance of 3-D automatic target recognition algorithms for identification and classification of targets. This work seeks to exploit the angular diversity through multiple observations of the target and number of slant planes through the range to the target to optimize collection against a target area.

SAL systems are typically designed to have a matched diffraction limited field of view for transmit and receive fields of view (FOV) to achieve maximum performance at range. At long range this diffraction limited FOV may fully illuminate a desired target area enabling image formation with a single coherent processing interval. The image formed would be a single slant plane image. As the range decreases the beam is required to be scanned to fully image the desired target area. This requires multiple coherent processing intervals and image stitching to image the desired target area which lowers the area coverage rate, defined as the amount of time necessary to image an area of the target. Each coherent processing interval forms a SAL slant plane image. An approach to increase the area coverage rate is to shape the illumination beam and populate additional detectors. These detectors may be arranged to increase the receiver FOV matched to the shaped transmitter FOV in a single dimension. These detectors may also have overlapping FOVs if they are smaller than the diffraction limited spot size.

We focus on improving the resolution in the real aperture diffraction limited dimension of SAL images. One solution to this problem that is presented in this work, is to divide the point cloud onto multiple slant planes as shown in table 3.4. At each look angles, instead of using one detector to compress the point cloud onto a single slant plane, multiple detectors are used to resolve the point cloud onto multiple slant planes. The detectors are aligned in the diffraction limited dimension, and are equally spaced. The detectors can have overlap between them if the pixel spacing is sub-diffraction limited. Each of these detectors will receive part of the target data and collapse them into slant planes. Descriptions of this

method is presented in detail in Chapter 3.

Previous work in 3-D image reconstruction has made use of the projection slice theorem, which is the backbone of medical imaging x-ray computer aided tomography (CAT) [11]. Radar experts took the idea of CAT to reconstruct 3-D SAR images, as Charles Jakowatz presented in his publication "*Spotligh-Mode Synthetic aperture Radar: A signal Processing Approach*". In his work, he was able to achieve fine resolution on the diffraction limited dimension (cross-track-cross-range dimension) by increasing the number of observation angles. This approach is effective; however the data collection time is very expensive for SAL. One of the goals of this thesis is to diminish the number of look angles, while improving the resolution of the SAL image in the diffracted limited dimension.

## 1.2 Contributions

This work simulates SAL imagery and incoherently combines multiple SAL images with tomographic reconstructions to measure benefits of angular diversity and multiple slant planes for performing 3D reconstructions of a target. In this work we develop metrics to measure the efficacy of the 3D reconstructions. A similarity metric based on mutual information to calculate the similarity between two images. While developing the similarity function, we developed an entropy function that measures the amount of information content in an image. From the similarity metric, we derived the joint information density metric. Since some of the information in the image is noise, the joint information density metric will track the amount of useful information in the volume as the CNR is being varied. In this work we investigated the way the information content of the reconstructed image, and the similarity between the truth image and the reconstructed image are affected; as we vary certain parameters such as: noise level, sensor position and number of observation angle. The Kullback-Leibler divergence was also compared to the similarity metric.

After reviewing the Tomographic Formulation of Spotlight-Mode SAR [11] and [14],

we implement an algorithm to reconstruct 3-D images of targets using tomographic reconstruction for SAL slant plane imagery and develop techniques for evaluating the efficacy of the reconstructions based upon the mutual information metric. The proposed methods enhance the resolution in the cross-track-cross-range diffraction limited dimension for both the single and multiple slant plane imaging SAL systems. At each observation angle the backscattered signals are compressed into SAL slant plane images consisting of range and along track cross range coordinates prior to projecting it into the tomographic synthesized plane of the 3-D grid in model frame coordinates.

The single slant plane method uses a monostatic setup, with a single transmitter and a single detector sharing the same antenna. The transmitter LADAR illuminates the entire target. The detector receives the backscatterers signal and generates a single slant plane image for the entire scene with a single coherent processing interval (baseline). For this method, the diffraction limited resolution is enhanced as the angular diversity in the number of projection angle is increased. For the multiple slant plane method, multiple transmitters and detectors are used. Each transmitter illuminates part of the target and it's collocated detector receives the backscattered signals which are compressed into slant planes. For this method, the diffraction limited resolution is enhanced as the number of detectors/slant planes are increased, or the number of observation angle is increased.

We model shot noise that we add to the SAL images. At each observation angle, and for each detector a new instance of noise is generated, therefore the random instance of noise is averaged each time a new projection is made to the synthesized plane. As a result, the methods presented in this work are useful in reconstructing 3-D images of targets, because it improves the resolution in the diffraction limited dimension. By enhancing the diffraction limited resolution, the similarity and the amount of useful information between the truth and the reconstructed image is increased.

## 1.3 Thesis Outline

The remainder of the thesis is set as follows. In Chapter 2 we discuss some of the history of SAL and describe SAL theory. The implementations of single and multiple slant plane methods are discussed. Furthermore, we explain in detail the geometry used to render the targets, and the model coordinate geometry used to perform the tomographic reconstructions. In addition, we discuss the penalties of using multiple slant planes and multiple observation angles to define that trade space. In Chapter 3 we describe the targets, and the methodology used to generate the point clouds of the targets. We discuss the SAL simulation of the data and presented exemplary images for the SAL simulation. Chapter 4 explores the application of backprojection, and explains in detail how the incoherent 3-D tomographic reconstruction was performed. Chapter 4 also presents the investigation into the impacts of speckle noise, shot noise, angular diversity and angular sampling on the 3-D reconstructed image. Chapter 5, discusses the metrics for measuring the efficacy of reconstructions, entropy, joint entropy, mutual information, useful information. Finally, we present the results, conclusion and future work in Chapter 6.

# CHAPTER 2

# SAL THEORY

In this chapter, we begin by giving a brief history and background about SAL system in Section 2.1. In Section 2.2, we describe SAL theory and provide the equations fundamental to SAL theory. We described in detail the definition of carrier to noise ratio CNR, and the implementation of single, multiple, and overlapping multiple slant plane SAL systems. Formulas for range\cross range diffraction limited, area coverage rate (ACR) for both single and multiple slant plane are provided. We describe the noise model and discussed its effect on the SAL image. Finally, we discussed about the trade-off and the penalties of multiple slant planes and multiple observation angles.

## 2.1 History\Background

Radio detection and ranging (RADAR) is a system for detecting the range, direction and speed of objects. It transmits pulses of high frequency electro-magnetic waves that are reflected from a target back to the receiver. Those reflected signal is denoted as backscatters. The backscatter signals are then processed by computers to obtain useful information about the target. The idea of RADAR was introduced in the late 1880, by German physicist Heinrich Hertz [18]. Hertz did an experiment that proved that radio waves are

reflected by metallic object and refracted by a dielectric medium, just as light waves can. However, RADAR was not implemented practically until the early 1930's when systems become more advanced, and caught the interest of the military. In the article *Radar* Skolnik states, "There was simply no economic, societal, or military need for radar until the early 1930s, when long-range military bombers capable of carrying large payloads were developed. "During this period, researchers became more interested in RADAR systems and developed it into a more sophisticated device. At the start of WWII several countries had some form of RADAR equipment for military applications [18].

In the mid-1900s, a technological breakthrough came with the invention of the MASER (microwave amplification by stimulated emission of radiation [17]. Charles Townes invented MASER in 1951, and later demonstrated the first MASER in 1954 at Columbia University [17]. In 1958, Charles Townes and lab partner Arthur Schawlow published a paper in *Physical Review Letters* to show the MASERS could be implemented in the optical and infrared domain [17]. They also proposed how it could be accomplished in the optical spectrum, this is known as LASER (light amplification by stimulated emission of radiation) [17]. The acronym LASER was coined by an American physicist Gordon Gauld; in his famous note book he describes the procedure of building a LASER [17]. Since the invention of LASER many applications that positively impact the communities have been developed. One such application is combining LASERs with RADAR and this is known as laser radar (LADAR) [2]. LADAR and RADAR are fundamentally similar however, they operate at vastly different wavelengths. LADAR operates in the optical region, and has very short wavelengths. These short wavelengths allow LADAR to produce higher image resolution than RADAR with similar aperture. These innovations have been further advanced to achieve a much finer resolution images by using aperture synthesis technique.

*Aperture Synthesis* is the technique of using the changes in the target platform geometry, and coherently collecting and processing data to increase the effective size of the resolution limiting aperture in one-dimension defined by the change in the geometry. Typ-

ically, this technique utilizes the path of the platform to create an effective aperture much larger than the physical aperture of the sensor in the direction of the motion. This is known as Synthetic Aperture Ladar (SAL). The range resolution of a SAL image is limited by the bandwidth of the waveforms processed, and the cross-range resolution is limited by the aperture synthesized. The dimension orthogonal to the platform motion remains real aperture diffraction limited.

Mathematically, SAL and SAR are identical. However, SAL operates in the micrometer ($um$) wavelength, which is $10^{4-5}$ shorter than SAR wavelengths which are 100s of millimeter ($mm$) wavelength [12]. The difference in wavelengths is approximately 5 orders of magnitude, and causes differing phenomenology in the electromagnetic radiation properties of the atmosphere transmission and scattering. Transmit beam width and resolution are dependent on the aperture and wavelength, thus SAL has the potential to produce higher resolution real aperture diffraction limited images than SAR and requires shorter synthetic aperture\aperture synthesis baselines for similar resolutions. For SAR imagery, the real aperture diffraction limited transmit beamwidth is on the order of km and for SAL it is on the order of m's for typical apertures [3]. Due to the real aperture resolution of SAL, it has the ability to create multiple diffraction limited slant planes for multiple detectors for a single target. These multiple slant planes can be projected into a single ground plane projection, and can also be displayed as a 3-D image with asymmetric resolution. Dividing a target into multiple slant planes will help resolve the data by increasing the real aperture diffraction limited resolution.

## 2.2 Theory

Figure 2.1 shows a simple geometry where the aircraft is illuminating a target on the ground plane. The sensor is mounted to the side of the aircraft, where the ray of the sensor is illuminating the target in the direction orthonormal to the flight path of the aircraft and

closest approach to the target; that direction is referred to as the target range. The direction parallel to the flight path of the aircraft is referred to as the along-track-cross-range and is parallel to the SAL baseline for aperture synthesis. The direction normal to both the range and along-track-cross-range in this case out of the screen is referred to as the cross-track-cross-range. Two common data collection modes for radar imaging are strip-map mode, and spotlight-mode.

In strip-map mode, the sensor is fixed at the direction perpendicular to the flight path of the aircraft. The aircraft transmits and receives pulses periodically as it goes across the flight path [11]. The longer the length of the region of integration is, the narrower the synthesize beam will became which yield to higher resolution on the cross-track dimension. Strip-map mode requires a long synthetic aperture (SA) time to produce a high-resolution image [11]. Figure 2.1 represents the basic geometry collection for strip-map aperture synthesis.

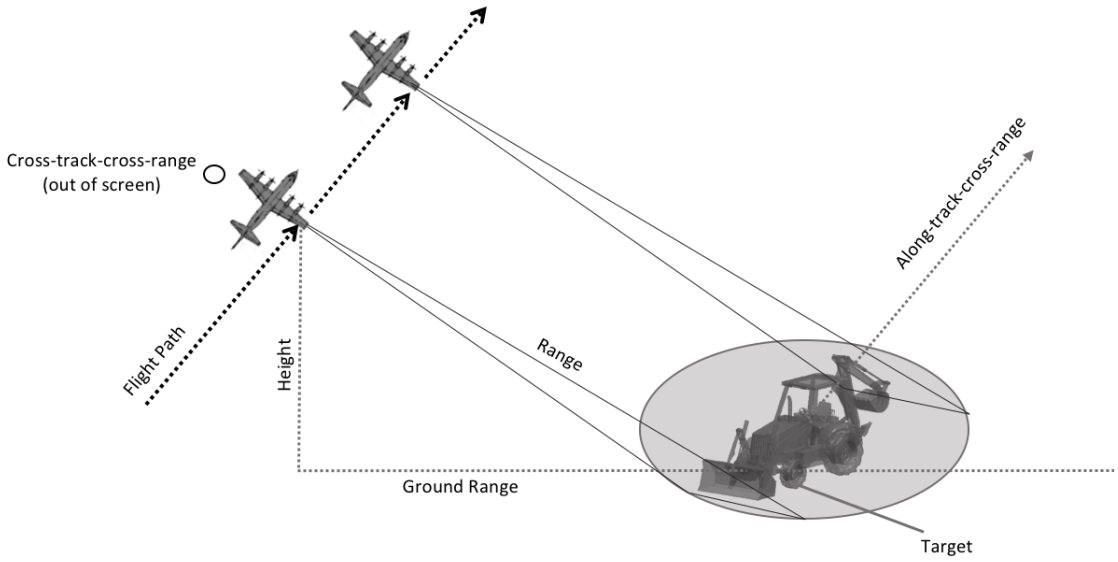


Figure 2.1: Example of a strip-map mode data collection

In contrast to the spotlight mode it turns out they are very different. However, in some situations spotlight mode algorithms are used to form images from data collected in a strip-map mode [11]. In spotlight mode, the beam of the sensor is steered to keep the target illuminated for a longer period of time. By doing so, longer SA will be achieved increasing the number of pulses transmitted by the sensor will also increase the resolution in the along-track-cross-range direction. In this research, we consider spotlight mode SAL as shown in Figure 2.2 to collect data and generate high resolution SAL images.

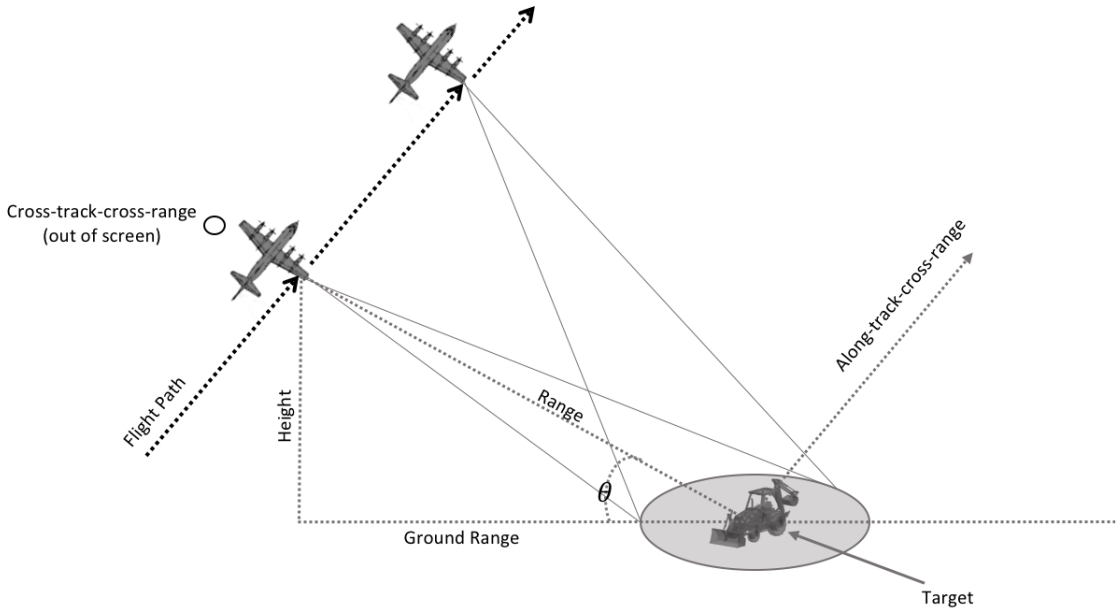


Figure 2.2: Example of a strip-map mode data collection

A general spotlight temporal SAL collection is illustrated Figure 2.3 [3], where the illuminating spot size $D_{spot}$ is determined by the diffraction limit of the transceiver optic, corresponding to the resolution of a conventional imager with the same aperture. The resolution in the direction of travel (azimuthal\along-track-cross-range, $\delta_x$) is determined by the wavelength and synthetic aperture length. The resolution in the orthogonal direction (range, $\delta_y$) is determined by the transmit waveform bandwidth, $B$.

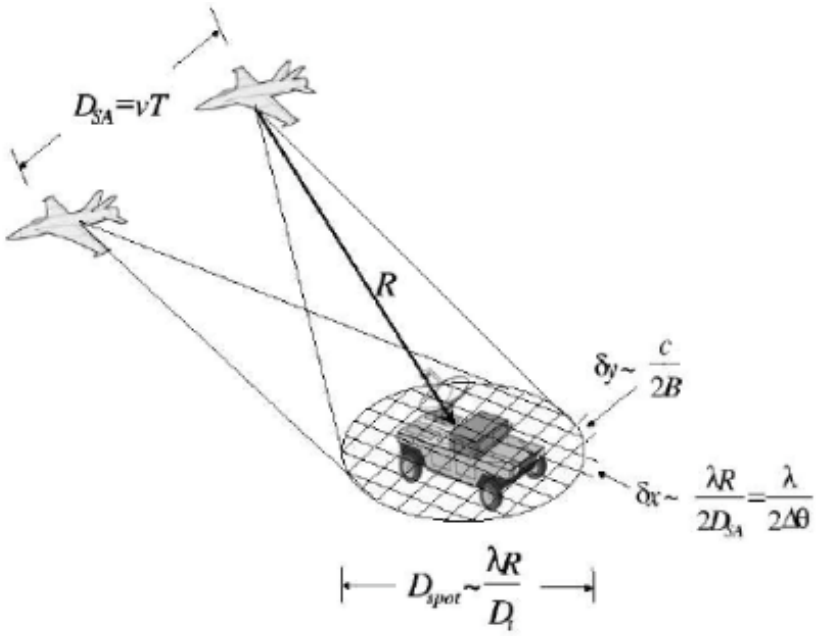


Figure 2.3: The SAL concept - This figure was taken from [3]

Figure 2.3 illustrate the SAL concept. The illuminating spot size $D_{spot}$ is determined by the diffraction limit of the transceiver optic, corresponding to the resolution of a conventional imager with the same aperture. The resolution in the direction of travel (azimuthal, $\delta_x$) is determined by the wavelength and synthetic aperture length. The resolution in the orthogonal direction (range, $\delta_y$) is determined by the transmit waveform bandwidth, B.

As shown in Figure 2.3 the SAL sensor is mounted on to an airborne platform moving with velocity v. Transmitting signals with wavelength $\lambda$ and bandwidth $B$ that illuminate a target and receiving the backscattered signals. The image resolution in the along-track-cross-range dimension is given by:

$$\delta_x = \frac{\lambda}{2 * \Delta\theta_{az}} \tag{2.1}$$

where, $\Delta\theta_{az}$ is the azimuth step-size as observed at the sensor view from range $R$, and it is

denoted as:

$$\Delta\theta_{az} = \frac{D_{SA}}{R} \tag{2.2}$$

The synthetic aperture length covered in the flight time $T$ is denoted as:

$$D_{SA} = v * T \tag{2.3}$$

The longer the $D_{SA}$ the finer the resolution azimuth resolution [3]. The range resolution for SAL is defined as:

$$\delta_y = \frac{c}{2 * B} \tag{2.4}$$

where $c = 3 * 10^8$ is the speed of light and $B$ is the bandwidth of the system.

Temporal SAL processes the returned signal from the illuminated target throughout the synthetic aperture baseline to form images. SAL mixes backscattered signals with a stable local oscillator ($LO$) and implements coherent (heterodyne) detection [3]. While detecting these signals, noise will be introduced to the SAL signals. [3] In limit of heterodyne detection, shot noise of the local oscillator will dominate and the signal is said to be shot noise limited (SNL). Shot noise is an additive noise it can be modeled as a Gaussian distribution [10]. The variance of the noise is inversely proportional to the CNR as defined in equation 3.14.

$$CNR = \frac{P_s}{P_n} \tag{2.5}$$

$P_s$ and $P_n$ are the signal power and the noise power, respectively. In this research, the signal power is defined as the mean of intensity of the SAL simulated image, and the noise power is defined as the additive mean Gaussian distributed intensity noise.

The short wavelength of SAL enables relatively narrow real aperture diffraction limited beam width. The relatively narrow real aperture resolutions allow for multiple slant planes to be created for a single target with reasonable range.

# CHAPTER 3

# SAL Simulation

In this chapter, we describe the method used to simulate SAL imagery with speckle from 3-D facet model. This method is tested by developing a simulation of slant plane SAL imagery in MATLAB, which will be given in Section 3.4. In Section 3.5, we discuss side-lobes suppression on the slant plane SAL imagery. Finally, in Section 3.6, we introduce and develop the shot noise model that will be applied to the SAL imagery.

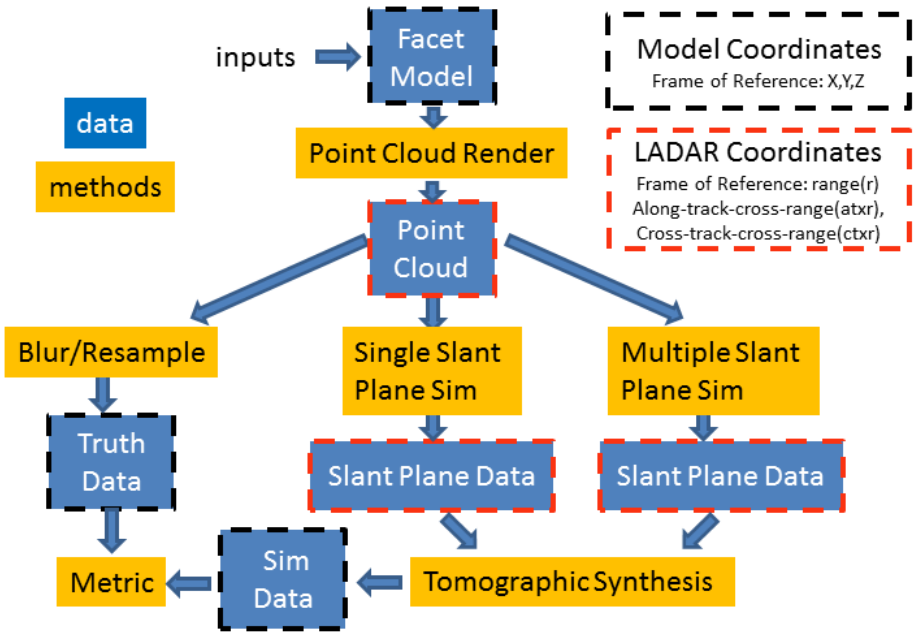


Figure 3.1: SAL Simulation Flow Diagram

## 3.1 Point Cloud

A point cloud is an set of information data in a orthogonal coordinate system. They often represent the outer surface of a target that a device, or a sensor has measured. Point clouds are used to study different features of a target, or reconstruct images of a target. In this research two targets were investigated, a non-structural target and a structural target. The point cloud of the non-structural target was generated by creating a grid with $6\ m$ field of

view (FOV) and 6 $m$ of range depth. We populate the grid with random points as shown in Figure 3.2. The point cloud is then observed at different elevation angles. At each elevation angle we compress the point cloud into slant plane and simulate the SAL image. This process is discussed in detail in Chapter 3.

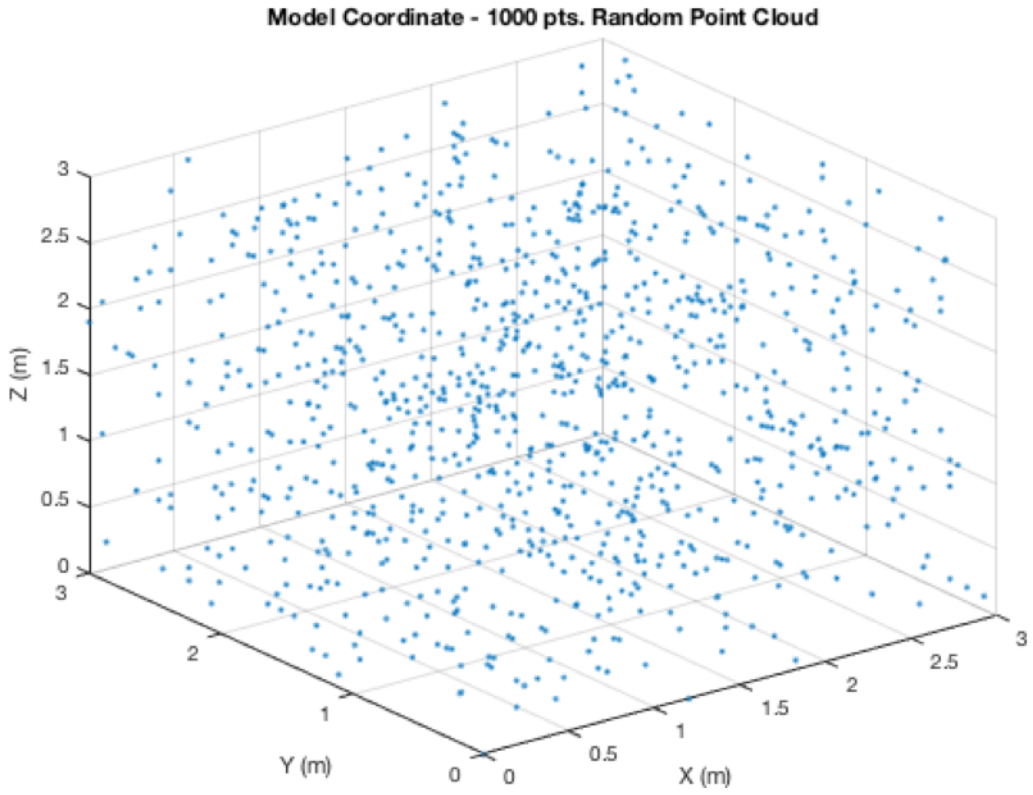


Figure 3.2: Model Coordinate of the Non-structural point Target

The second target that was used in this study is the backhoe data. This target has structured features, and its facet model is shown in Figure 3.3. Facet model composes the target with many small triangular facets, where each of these facet surface approximates the real target with fidelity proportional to the number of facets [6].

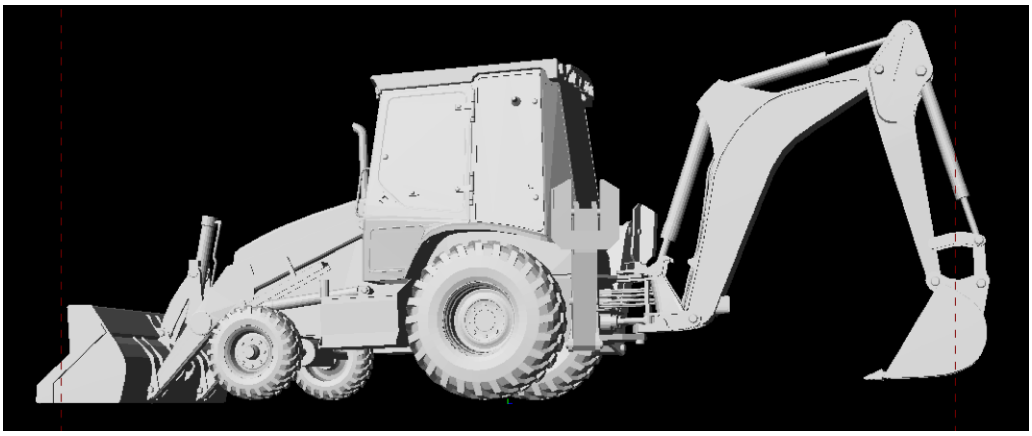

Figure 3.3: Facet Model of the backhoe target

The point cloud object of the facet model was generated using a point cloud generator tool, where the range, field of view (FOV), azimuth, elevation, tilt, the sensor resolution in the x-y direction and the facet model are defined by the user. The render tool outputs the bi-directional reflectivity distribution function (BRDF), surface normal, and X, Y, Z data that can be used to display the 3-D spatial representation of the model as shown in Figure 3.4. The BRDF outputs the Lambertian BRDF if the rays traced contact a facet, and outputs a ”-1” if the ray traced doesn’t contact a facet. From there we can filter out and simplify the data by only focusing on the rays traced that contact the target.

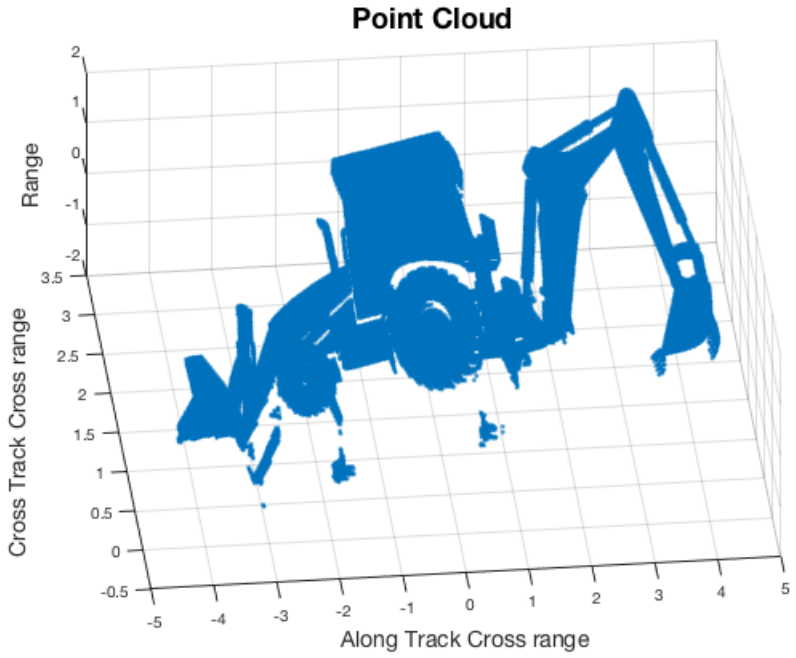


Figure 3.4: Point cloud of the backhoe facet model data

| Sensor Parameters | | | |
|---|---|---|---|
| Parameters name | Symbol | Values | Units |
| Azimuth angle | $\theta_{az}$ | -75 | $^\circ$ |
| Elevation angle | $\theta_{el}$ | 20 | $^\circ$ |
| Range | $R$ | 20000 | $m$ |
| Field of View | $FOV$ | 20 | $m$ |
| Azimuth step size | $\Delta\theta_{az}$ | 1 | $cm$ |
| Tilt | $\xi$ | 0 | $^\circ$ |

Table 3.1: Sensor parameters used to generate the point cloud of the backhoe data. The point cloud of the backhoe is generated at different elevation angles.

Table 3.1 represents the parameters used to generate the point cloud shown in Figure 3.4. This parameter can be varied to obtain the desired point cloud.

## 3.2 Geometry

### 3.2.1 Single Slant Plane Geometry

As mentioned earlier, we use spotlight mode for data collection for both single slant plane and multiple slant planes. The terminology single slant plane (SSP) refers to mounting a single detector on an airborne platform where the detector receives the backscattered signal from the target in the range dimension. This beam of rays was transmitted by a single transmitter, and will pass through a lens as shown in Figure 3.5. The lens aperture determines the diffraction limited spot size ($D_{LSS}$) to illuminate the entire target in the range and cross-track-cross-range dimension. The $D_{LSS}$ is inversely proportional to the size of the lens defined as:

$$D_{LSS} = 2.44 * \frac{R * \lambda}{D_{lens}} \tag{3.1}$$

where, $R$ is the range from the sensor to the target, $\lambda$ is the wavelength of the signal, and $D_{lens}$ is the diameter of the lens. For this geometry, we use a circular aperture, the area coverage rate (ACR) is defined as:

$$ACR = \frac{\pi * r^2}{\tau} \tag{3.2}$$

Where $r$ is the radius of the pupil and $\tau$ is the SAL resolution time. We synthesized on the along-track-cross-range to resolve that dimension. Figure 3.5 shows the geometry for the SSP on the range vs. cross-track-cross-range view.

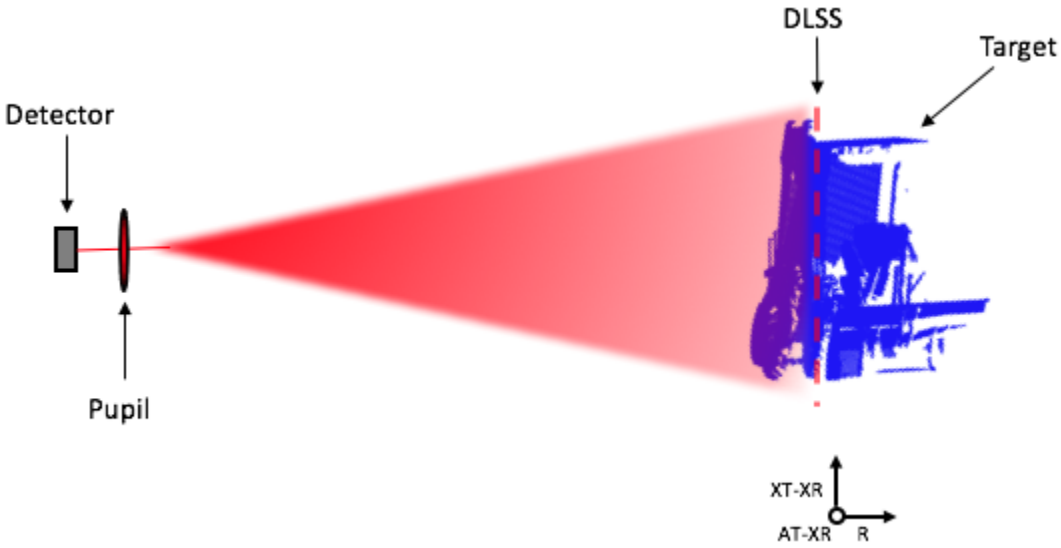


Figure 3.5: SSP geometry Range vs. Cross-Track-Cross-Range coordinates.

The point cloud of the facet model is rendered at different elevation angles, where at each look angle a unique point cloud is produced. Each point cloud is then compressed into a slant plane by accumulating the values on the cross-tract-cross-range as shown in table 3.2 and 3.3. The compressed point clouds will be used for the SAL simulation data. The SAL simulation method is described in detail in Chapter 3.

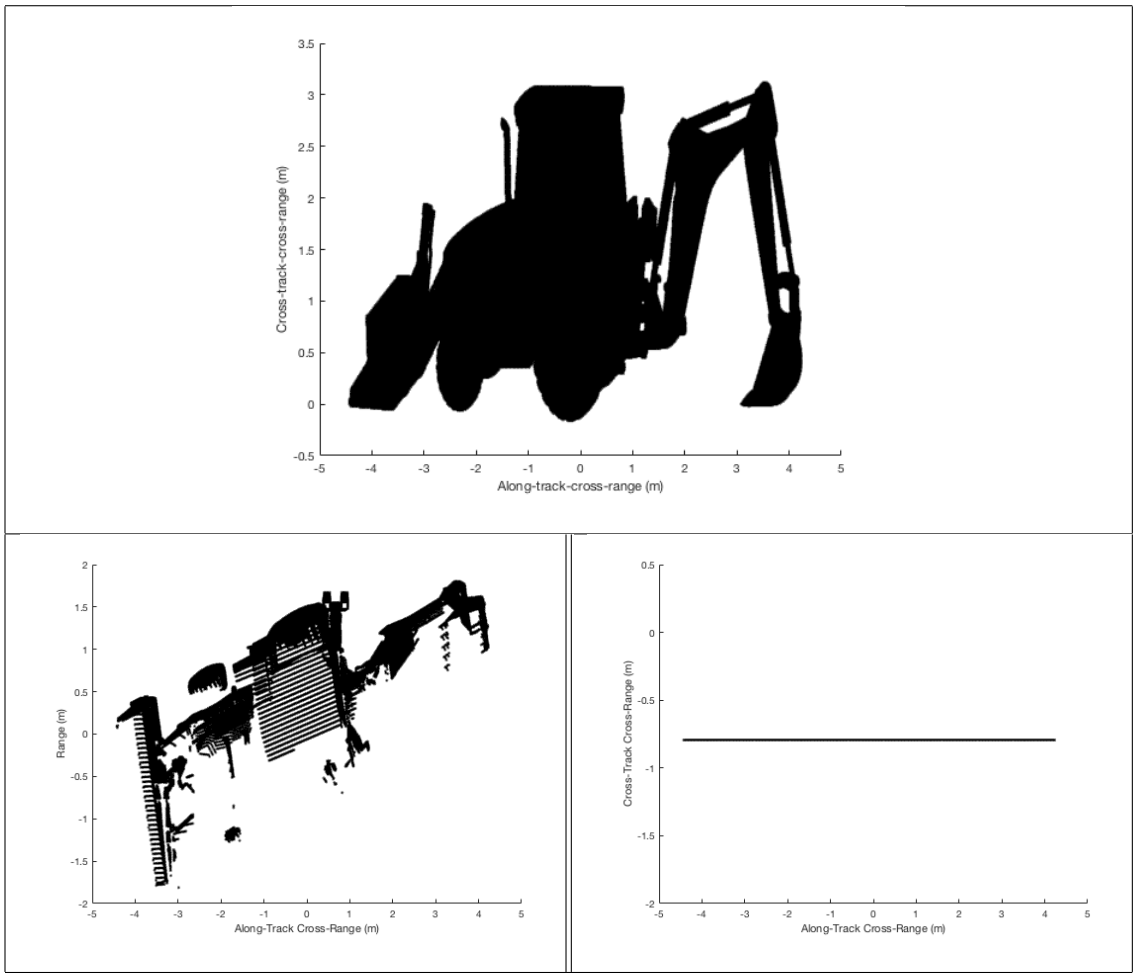


Table 3.2: Point cloud compressed at single slant plane. This point cloud was rendered at $10^{\circ}$ elevation angle.

The plot on the top is the sensor perspective of the point cloud for the backhoe data rendered at $10^{\circ}$ elevation angle. The bottom left plot is the Range vs. Along track cross range view. On the bottom right plot is the compressed point cloud shown in the cross-track-cross range vs. along track cross range view.

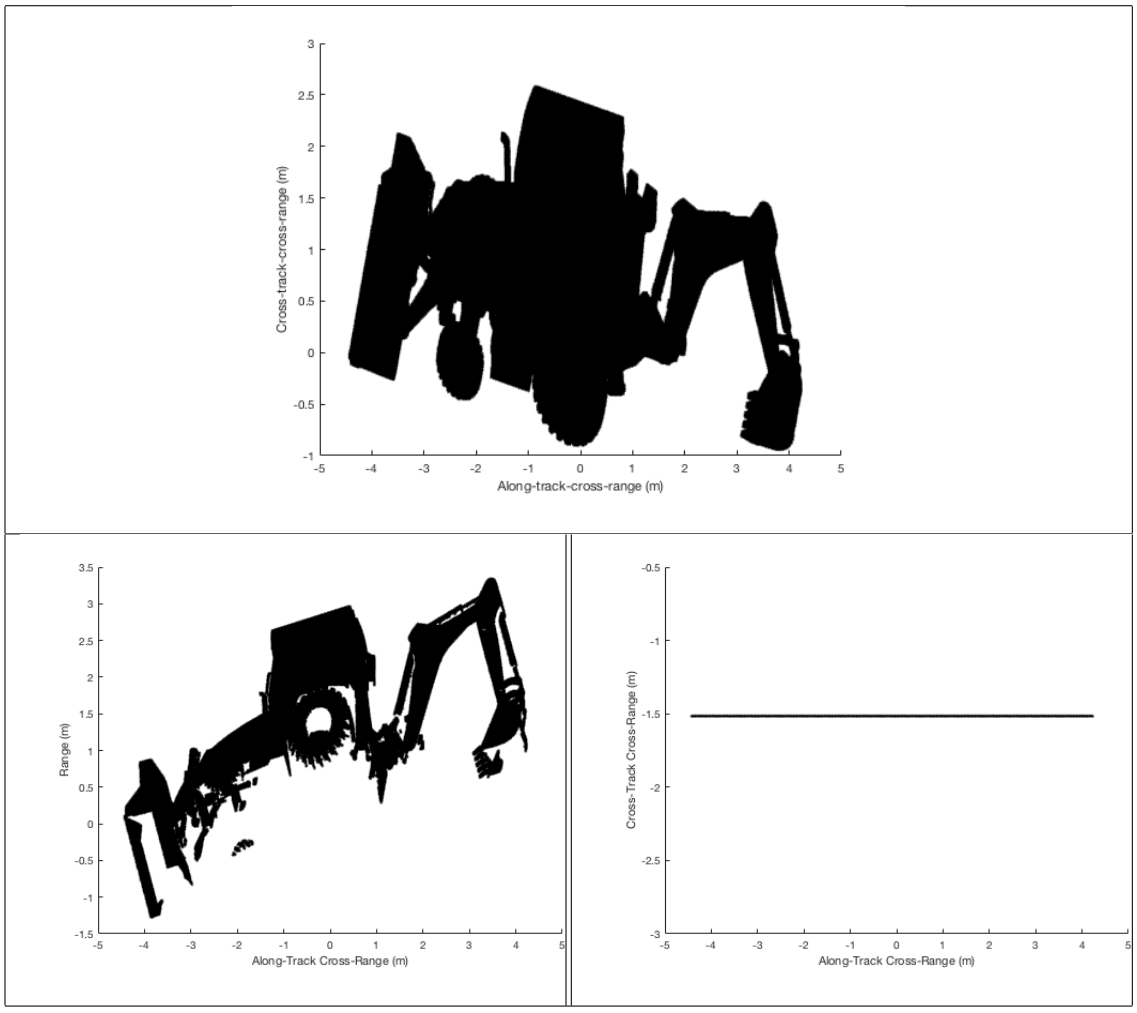


Table 3.3: Point cloud compressed at single slant plane. This point cloud was rendered at $50^\circ$ elevation angle.

The plot on the top is the sensor perspective of point cloud for the backhoe data rendered at $50^\circ$ elevation angle. The bottom left plot is the Range vs. Along track cross range view. On the bottom right plot is the compressed point cloud shown in the Cross-track-cross range vs. Along track cross range view.

### 3.2.2 Multiple Slant Plane Geometry

For the multiple slant planes (MSP) geometry, multiple detectors are mounted in the SAL receiver on the airborne platform. These detectors are set parallel to the cross-tract-cross-

range dimension, equally spaced and they can overlap. They are set in such a way that each detector FOV sees only part of the target, and as a whole, they see the whole target dimension in cross-track-cross-range. Unlike the SSP where the transmitted diffraction spot size is circular at the target, for the MSP the SAL transceiver FOV is elliptical at the target as shown in Figure 3.7. The ACR for each detector is defined as:

$$ACR = \frac{\pi * \frac{a}{2} * \frac{b}{2}}{\tau} \tag{3.3}$$

Where, $a$ is the length of the elliptical transceiver FOV, $b$ is the width of the elliptical transceiver FOV, and $\tau$ is the SAL resolution time. The spacing and height of the detectors are determined respectively as:

$$SP_{spacing} = \frac{a}{(Num_D - 1) * (1 - SP_{overlap}) + 1} \tag{3.4}$$

$$SP_{Height} = \frac{SP_{spacing}}{1 - SP_{overlap}} \tag{3.5}$$

Where, $Num_D$ is the number of detectors desired for MSP, and $SP_{overlap}$ is the fractional percentage overlap between the detectors. Assuming that these detectors are diffraction limited in the along-track dimension, and sub-diffracted limited in the cross-track dimension we can say that $b = SP_{spacing}$. Figure 3.6 gives a visual representation on how the MSP geometry works. Unlike the SSP, where there is a single detector illuminating the whole target, in this setup shown in figure 3.6 we have three detectors, equally spaced, and have 50% overlap between them. Each detector receives signal that passes through the pupil. Each detector illuminates part of the target, and collapses it into slant plane. Since in this setup we have 50% overlap between the detectors, certain parts of the target will be illuminated at least twice. These will allow us to have more information about the tar-

get, leading to better resolution on the cross-track-cross-range, as we will discuss in later sections. The transmit beam show in Figure 3.6 could be shaped by aperture to achieve diffraction pattern shown in Figure 3.7.

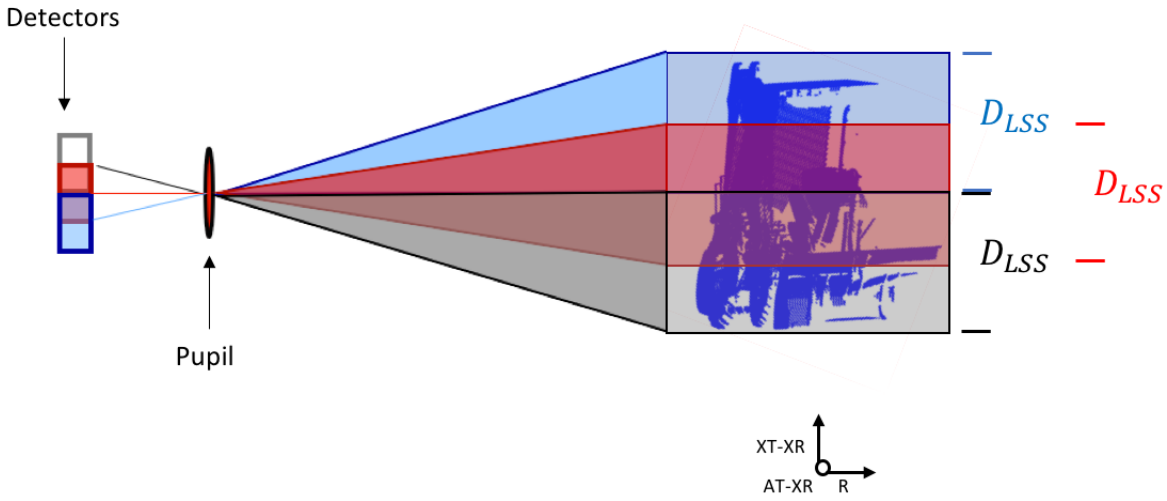


Figure 3.6: Example of MSP geometry with 3 detectors and 50% overlap between them. Range vs. Cross-Track-Cross-range coordinate.

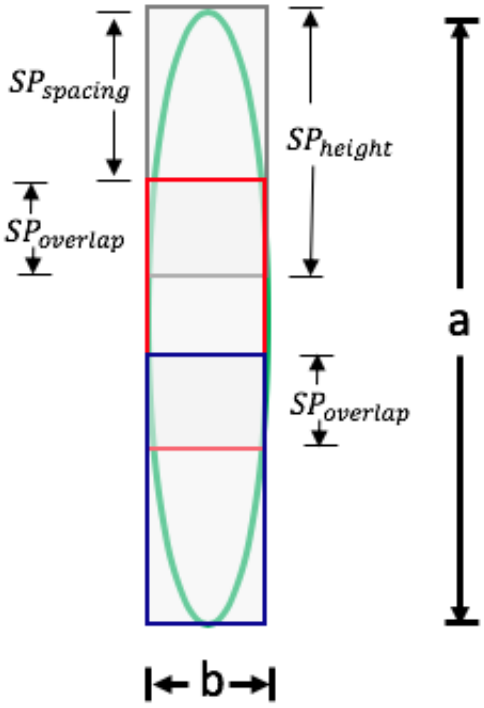


Figure 3.7: MSP diffraction limited transmit beam and receiver FOVs at target plan.

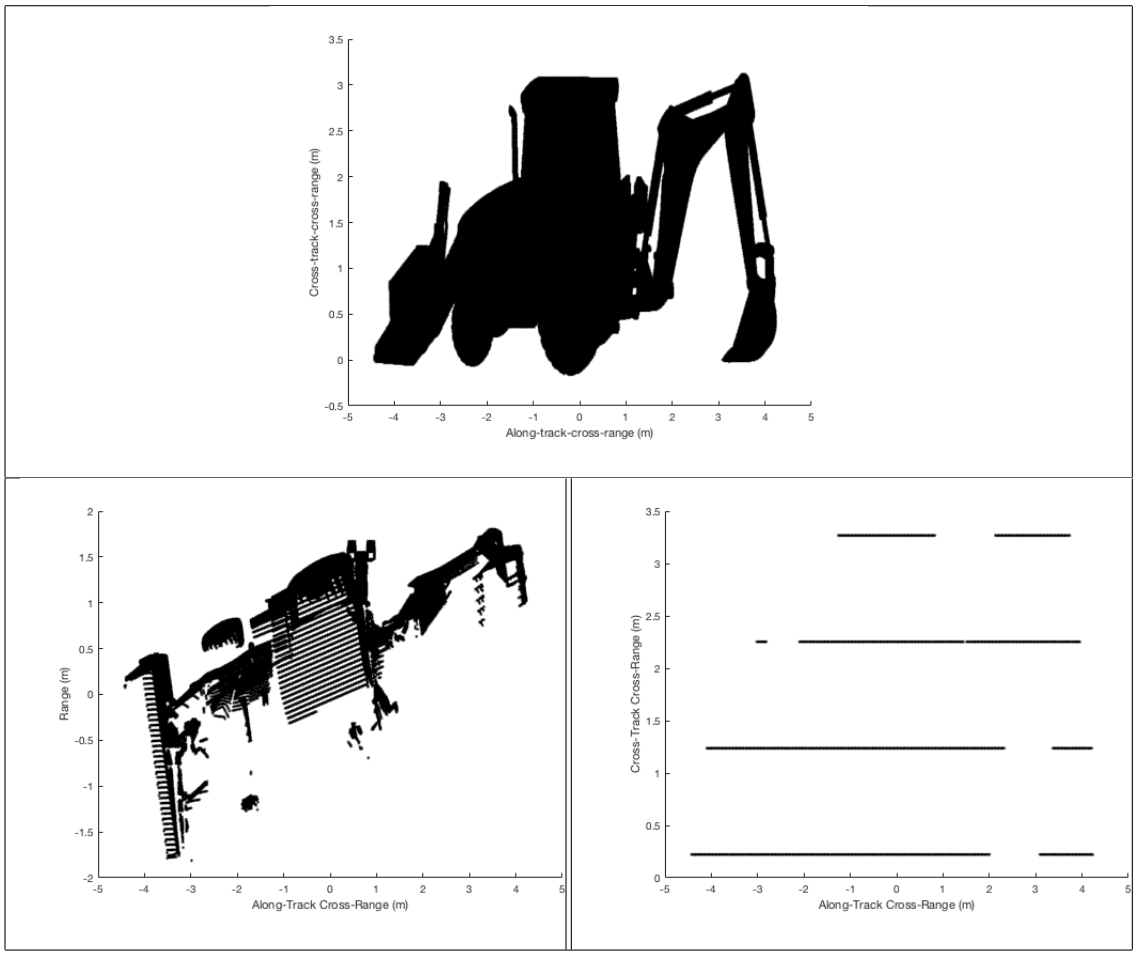


Table 3.4: Point cloud compressed at multiple slant plane. This point cloud was rendered at $10^{\circ}$ elevation angle.

In table 3.4 the plot on the top is the sensor perspective of point cloud for the backhoe data rendered at $10^{\circ}$ elevation angle. The bottom left is the Range vs. Along track cross range view. On the bottom right, the compressed point cloud is shown in the Cross-track-cross range vs. Along track cross range view. In this setup we have 50% overlap, and a spacing of 1 m between the detectors

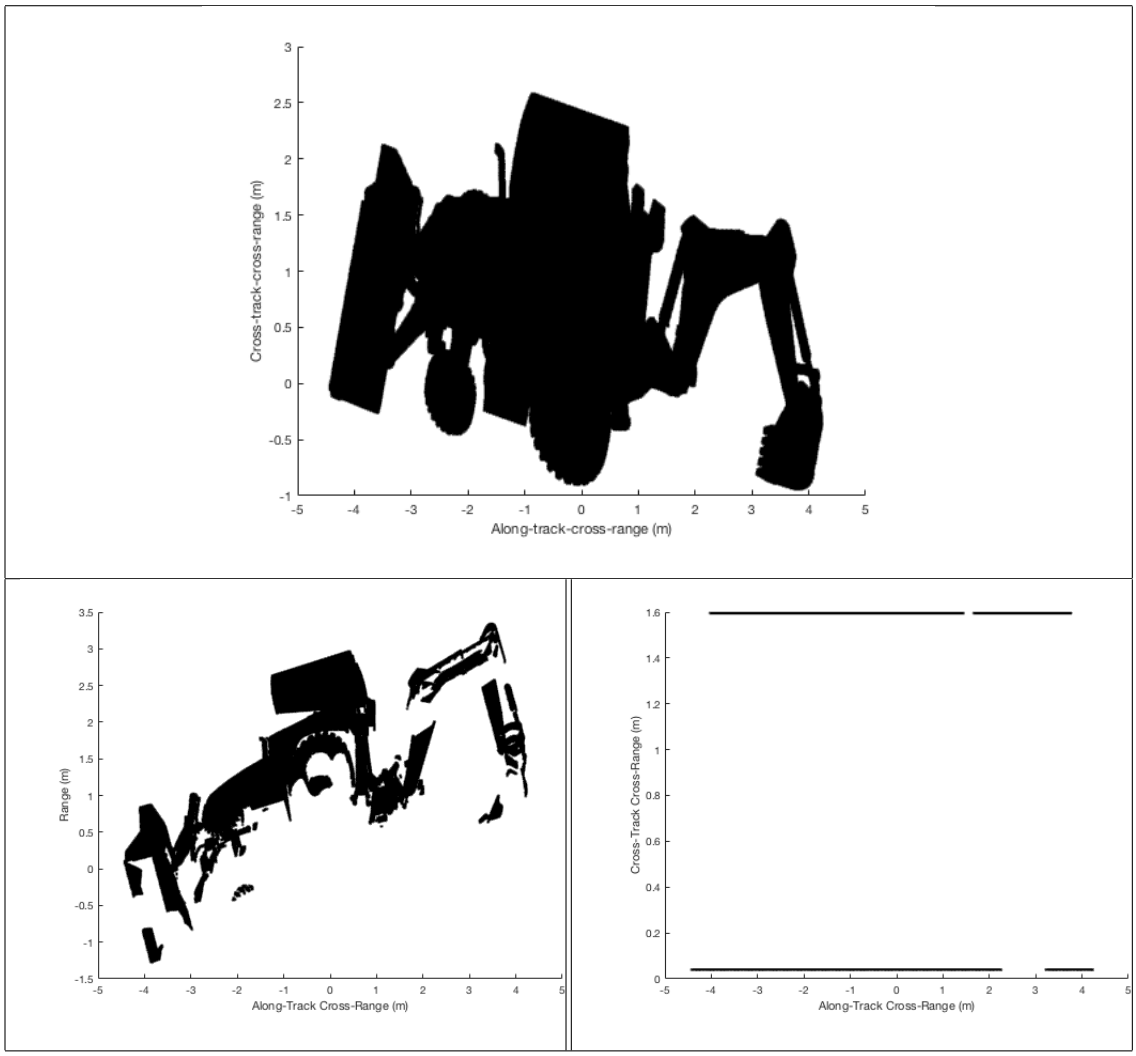


Table 3.5: Point cloud compressed at multiple slant plane. This point cloud was rendered at $50^\circ$ elevation angle.

Table 3.4 and 3.5 show how the point cloud was divided into multiple slant planes. The plot on the top on table 3.4 and 3.5 are the point clouds of the backhoe rendered at $10^\circ$ and $50^\circ$ elevation angle, respectively. The plots on the bottom left and right on tables 3.4 and 3.5 show the point cloud of the backhoe divided into multiple slant planes. Four monostatic setups were requires to the airborne platform to illuminate and receive data of the target as a whole. Note that the point cloud rendered at $50^\circ$ elevation angle is compressed into 2 slant planes instead of 4 slant planes. This is because at that observation angle, the height of the target observed by the sensor diminishes. Therefore, less transmitter is needed to

illuminate the whole target.

## 3.3 Trade-off between single Slant plane method and multiple slant plane method

| Single Slant Plane | | | |
|---|---|---|---|
| $SAL_{res}$ | | 0.1 | $m$ |
| $SAL_{res}$Area | | 0.01 | $m^2$ |
| $\boldsymbol{D_{lens}}$ | | **0.025** | **m** |
| $Fov, D_{lss}$ | | 10 | $m$ |
| $DLF$ | | 2.44 | $m$ |
| Lambertian Refl | | 100 | % |
| $DL_{ang}$ | $\frac{\lambda}{D_{lens}}$ | 3e-4 | r |
| **Rx** | | **1** | **nW** |

$$R = \frac{D_{LSS} * D_{lens}}{2.44 * \lambda} = 68.3\ Km$$

$$R_{loss} = \frac{\pi * r_{lens}}{2 * 2 * \pi * R^2} = 6.7 * 10^{-13} m$$

$$\mathrm{T}x = \frac{Rx}{R_{loss}} = 1.5\ KW$$

| Multiple Slant Plane | | | |
|---|---|---|---|
| $SAL_{res}$ | | 0.1 | $m$ |
| $SAL_{res}$Area | | 0.01 | $m^2$ |
| $\boldsymbol{D_{lens}}$ | | **0.025** | **m** |
| $Fov, D_{lss}$ | | 10 | $m$ |
| $DLF$ | | 2.44 | $m$ |
| $DL_{ang}$ | $\frac{\lambda}{D_{lens}}$ | 3e-4 | r |
| **Rx** | | **1** | **nW** |
| $Num_{detec}$ | | 10 | N/A |
| $overlap_{percent}$ | | 0.5 | |
| $a$ | $D_{lss}$ | 10 | m |

$$SPS = \frac{a}{n + 2 * overlap} = 1.81\ m$$

$$SPH = SPS\ * (1 + 2 * overlap) = 3.6364\ m$$

$$b = SPHeight * \left(1 - overlap_{percent}\right) = 1.81\ m$$

$$R = \frac{b * D_{lens}}{2.44 * \lambda} = 12.4\ Km$$

$$R_{loss} = 2.03 * 10^{-11} m$$

$$\mathrm{T}x = \frac{Rx}{R_{loss}} = 49.3\ W$$

Table 3.6: Trade-Off between single slant plane method and multiple slant method.

As mentioned earlier in Section 1.1, at long range image formation of the target can be done with a single coherent processing interval given sufficient illumination power due to the receiver field of view. However, as range decreases to fully reconstruct the target multiple coherent processing intervals and image stitching are required to image the desired target

area. Each coherent processing interval forms a SAL slant plane image. Table 3.6 shows an example of the trade-off that will be made when using the single slant plane method or multiple slant plane method with 10 overlapping detector fileds of view for the same system Field of View in the diffraction limited cross range dimension. In this example we set the received power ($R_x$), the diameter of the lens ($D_{lens}$) and the field of view (FOV) and minimum scattering area for resolution to be constant for both methods. Equation 3.1 was modified to solve for the range ($R$). As you can see from Table 3.6 for the single slant plane method, if we want to receive $1\ nW$ of power for a return area $0.01\ m^2$ with a $2.5\ cm$ lens, we will require to transmit $1.5\ kW$ of power at a range of $68.3\ km$ away from the target. As for the multiple slant plane method, if we want to receive the same amount of power using the same lens, it requires transmit power of $49.3\ W$ of power at a range of $12.4\ km$. From this example, we can see there is a trade-off between the range and the transmit power that we need to put into consideration when using these methods.

## 3.4 Slant Plane SAL Imagery

For simulation of the slant plane SAL imagery, the 3-D point cloud is compressed into slant plane, where the values on the cross-track-cross-range dimension are summed into a single value. As mentioned in Chapter 2 the point cloud of the backhoe data was generated in such a way that the along-track and cross-tract dimension are discretely sampled with 1 cm resolution. However, the range dimension is continuous. We interpolated the range dimension to a uniformly sample grid with 10 cm resolution to match the along-track-cross-range SAL resolution. The slant plane data is then multiplied by a uniform distribution of random phase to create random amplitudes (speckle) on the image. The uniform distribution random phase is defined as:

$$\psi = e^{-j*\phi} \tag{3.6}$$

where $\phi = 2 * \pi * rand(length(Z), 1)$. We accumulate the complex return signals into a single complex value. Since, we are interested in the backscattered signals from the transmitted beam that hits the target, we multiply the slant plane data by the Bidirectional Reflectivity Distribution Function (BRDF) for the respective points with the normal of the facet vector to yield the Lambertian reflectivity for the points. The BRDF will index in to the return signals that only hit the target. We then accumulate the range values with a sinc function and map the data to the uniformly sampled grid of 10 cm resolution grid as shown in Figure 3.8. The signal modeling for the SAL simulation imagery is defined in equation 3.7.

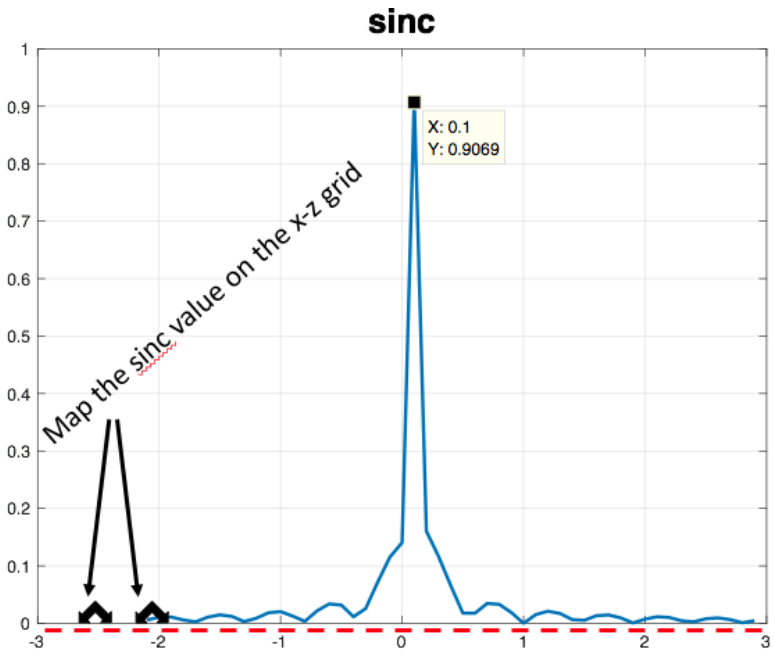


Figure 3.8: Example of mapping a continuous machine precision range value onto the uniformly sampled grid of 10 cm resolution. -3 to 3 pixels

$$S = BRDF * \psi * A * sinc(z - z_i) \tag{3.7}$$

$$IMG = \sum_{i=1}^{n} IMG(:, n) + S \tag{3.8}$$

Where $A = 1.22/\delta_r$ is the 3-dB full width half max of the $sinc$ function, $\delta_r$ is the range resolution, $z$ is the original continuous range values and $z_i$ is the new discrete range values and $IMG$ is the image after blurring the range dimension with the $sinc$ function to achieve the desired resolution of 10 cm. To complete the simulation of the slant plant SAL image, we took the Fourier transform of the image and apply a rectangular 1-D lowpass filter to the along-track dimension in the frequency domain to add a random amplitude or speckle to the data. We then inverse Fourier transform the image back to the spatial domain to create the slant plant SAL image of proper resolution as show on table 3.7, where the mean of the speckle is equal to the standard deviation of the intensity image [8].

$$H_r(f) = \begin{cases} 1, & \text{if } |x| \leq \frac{M-1}{2}. \\ 0, & \text{otherwise.} \end{cases} \tag{3.9}$$

$$I = \mathcal{F}(IMG * H_r) \tag{3.10}$$

$$SAL_{sim} = \mathcal{F}^{-1}(I) \tag{3.11}$$

$H_r$ is the rectangular window lowpass filter kernel, it is a vector with length equal to the length of the along-track dimension $M$. $H_r$ is equal to "1" at the bins we want to keep and "0" everywhere else. $SAL_{sim}$ is the simulated slant plane SAL imagery. It is a 2-D image with size N-by-M. $\mathcal{F}$ and $\mathcal{F}^{-1}$ are the symbols used for the Fourier transform, and inverse Fourier transform, respectively. The lowpass filtering process was performed in the frequency domain instead of the spatial domain; because instead of having to deal with complex convolution problems, we can transform the image and the kernel filter to

the frequency domain and multiply them together. Furthermore, it is computational faster in MATLAB to perform a multiplication in the Fourier transform instead of convolution in the spatial domain.

## 3.5 Taylor Window

To reduce the side lobes of the slant plane SAL imagery Taylor windowing was used. Taylor window is frequently used in SAR and SAL imaging systems, because it offers strong sidelobe reduction with minimal broadening on the mainlobe [15]. Additionally, the sidelobe reduction is selectable via the window parameters. For this experiment, the peak sidelobe level was set to -35 dB and the number of nearly constant level sidelobes adjacent to the mainlobe was chosen as 5, these are typical SAR and SAL parameters [5]. The filter kernel was chosen to equal the size of the $SAL_{sim}$ image $M$. The Taylor window weighting function is expressed as:

$$Tay(n) = 1 + \sum_{m=1}^{\bar{n}-1} F_m \cos(\frac{2\pi mn}{M-1}), |n| \leq \frac{M-1}{2} \tag{3.12}$$

In equation 3.12, $F_m = F(m, \bar{n}, \eta)$ is the Taylor coefficients of the mth order. $\bar{n}$ is the number of constant level sidelobes adjacent to the mainlobe, $\eta$ is the ratio of the mainlobe over sidelobes and M is the length of the window. The Taylor window equation was obtained from [7], and it's very similar to the MATLAB definition of Taylor window.

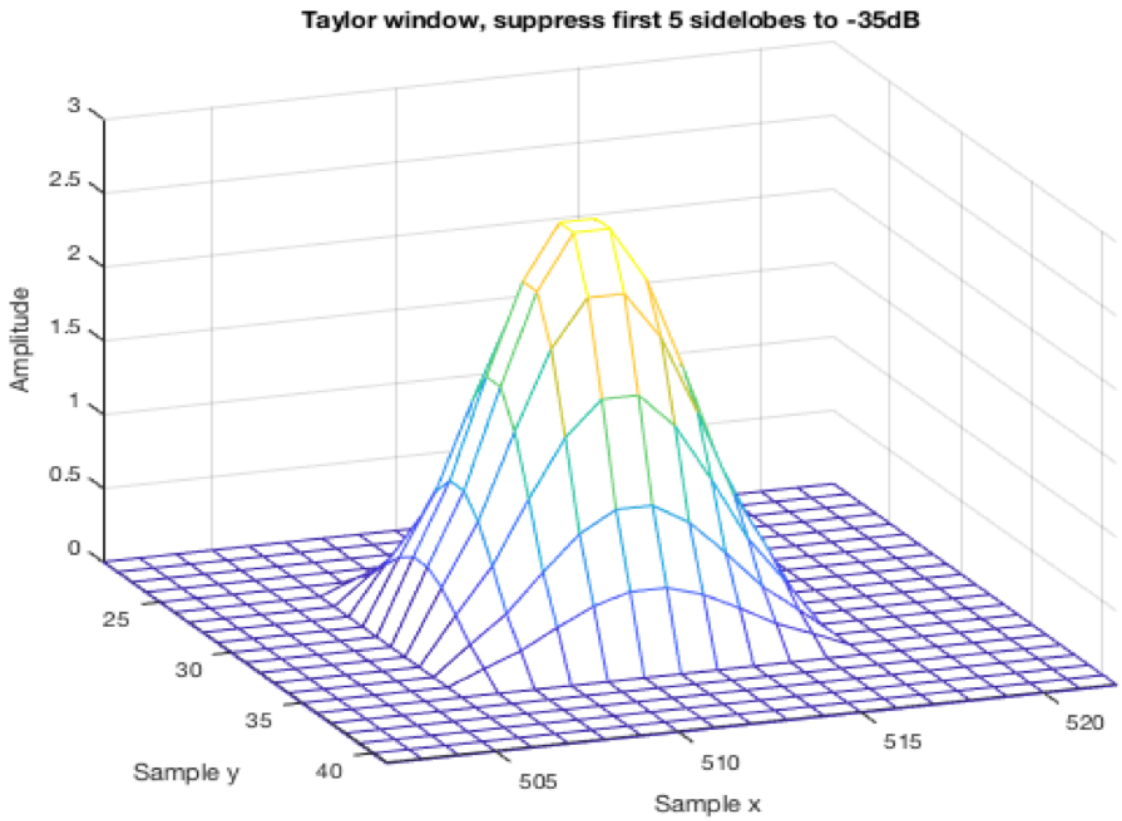


Figure 3.9: Taylor Window suppressing $\bar{n} = 5$ to -35 dB

Figure 3.9 is a representation of the Taylor window function used to reduce the sidelobes of the SAL simulation image. The parameters of this function are set to reduce the first 5 sidelobes of the SAL image. When performing Taylor windowing there will be a trade-off between the mainlobe and the sidelobes. As the sidelobes are being reduce the mainlobe of the signal will be broaden, and that will cause a blur on the image resolution. However, this blur is minimal, less than 20% for the Taylor window used and the sidelobes are suppressed significantly as shown in table 3.7. The Taylor windowing process was done before performing the tomographic reconstruction to make sure that the sidelobes won't correlate and cause some artifacts on 3-D image.

## 3.6 Shot Noise

In this section, we discuss the shot noise modeling for SAL imagery. Shot noise is present on SAL imagery due to noise in the detection process. Coherent detection through heterodyne mixing can nearly achieve shot noise limited detection with sufficient heterodyne local oscillator (LO) levels. As Gaussian jitter is always present in LADAR, the noise model presented here is based on a Gaussian distribution as shown in equation 3.13

$$W_n \sim \mathcal{N}(0,\, \sigma^2) \tag{3.13}$$

$$\sigma^2 = \sqrt{\frac{mean(I)}{2 * CNR}} \tag{3.14}$$

The noise distribution has a 0 mean ($\mu$), and the variance of the noise $\sigma^2$ is equal to the square root of the ratio of the mean intensity ($I$) of the SAL simulated image and twice the CNR. The size of the SAL simulation images is all the same. At each observation angle a random draw of the shot noise is generated. Therefore, when performing the tomographic reconstruction as described in Chapter 4 the variance of the noise is reduced by the square root of the number of observation angle.

## 3.7 Single Slant Plane SAL simulation Image

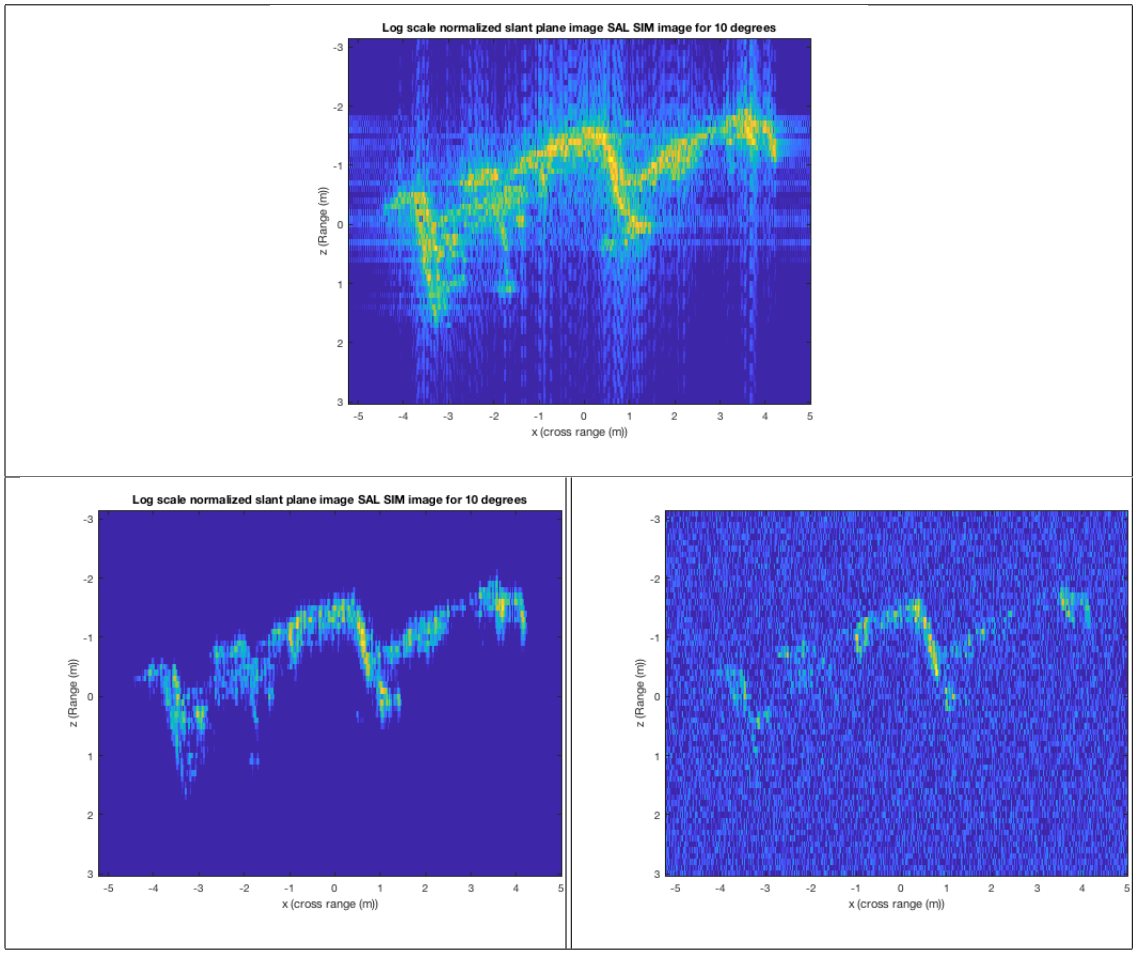


Table 3.7: SAL simulation images of the backhoe rendered at $10^{\circ}$ elevation angle using single slant plane method

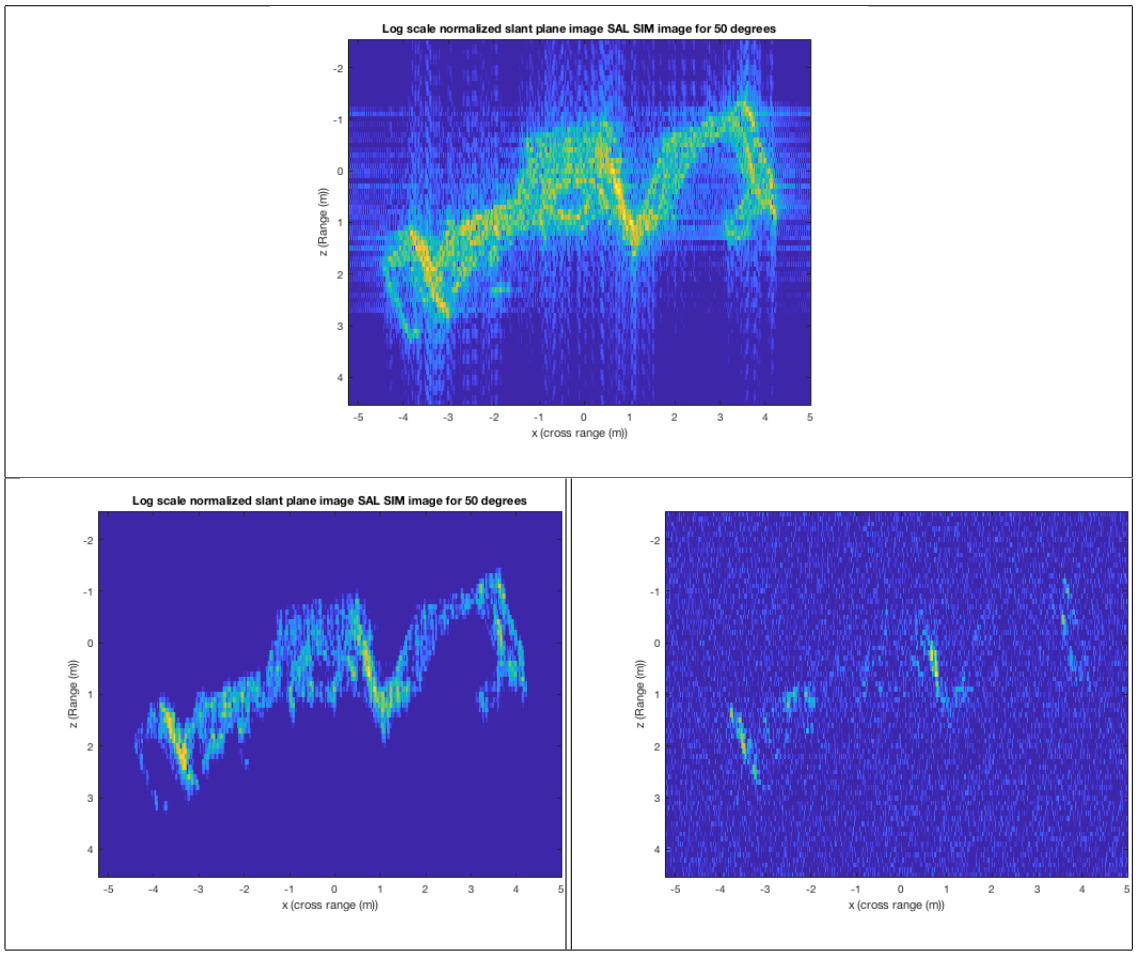


Table 3.8: SAL simulation images of the backhoe rendered at $50^\circ$ elevation angle using single slant plane method

These figures are the SAL simulation images of the backhoe data rendered at $10^\circ$ elevation angle on table 3.7, and $50^\circ$ elevation angle on table 3.8 using single slant plane method. The plot on the top in both table 3.7 and 3.8 is the noise-less SAL simulated image. We can see the side-lobes on both the range and cross-range dimension. Taylor window was applied the image to suppress the side-lobes as shown on the bottom left. The plot on the bottom right is the SAL simulated image after the additive Gaussian noise is added for a CNR of 10 dB

## 3.8 Multiple Slant Plane SAL simulation Image

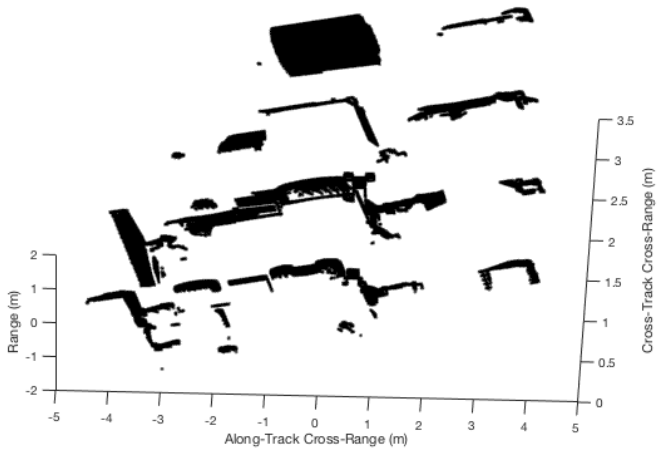


Figure 3.10: Compresses point cloud into 4 slant planes

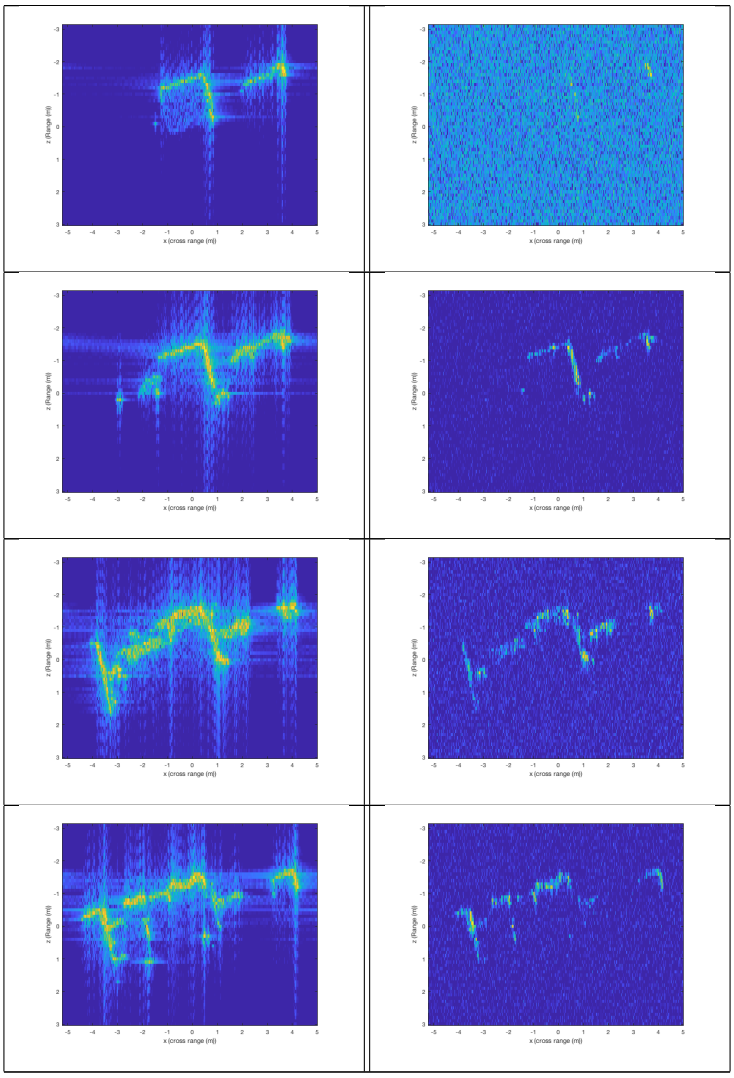

Table 3.9: SAL sim images of the backhoe rendered at $10^{\circ}$ elevation angle using multiple slant plane method

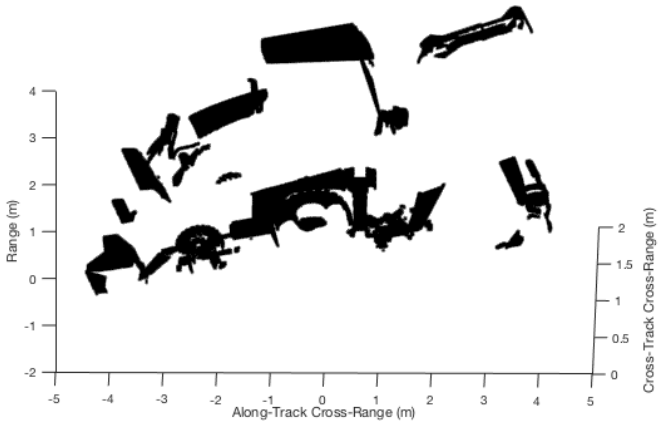


Figure 3.11: Compresses point cloud into 2 slant planes

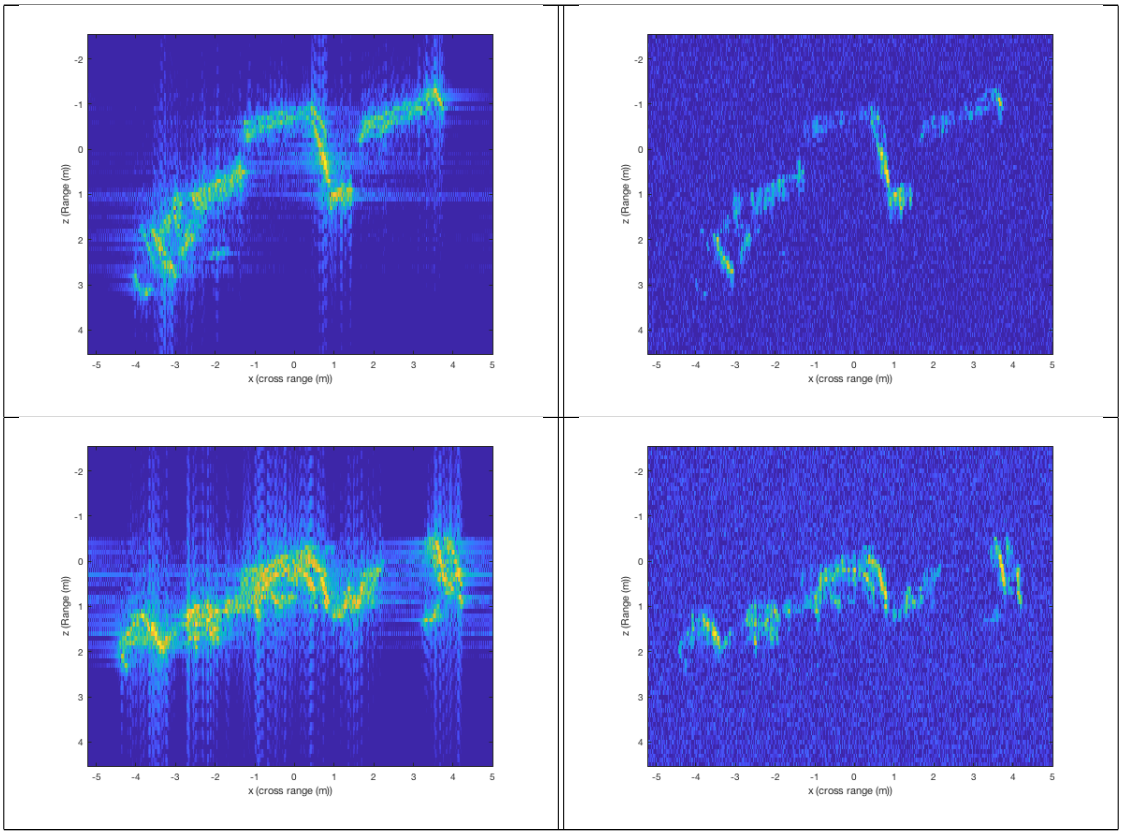


Table 3.10: SAL simulation images of the backhoe rendered at $10^{\circ}$ elevation angle using multiple slant plane method

These figures are the SAL simulation images of the backhoe data rendered at $10^\circ$ elevation angle on table 3.9, and $50^\circ$ elevation angle on table 3.10 using multiple slant plane method. The plots in the left columns in both table 3.9 and 3.10 is the noise-less SAL simulated image. We can see the side-lobes on both the range and cross-range dimension. Taylor window was applied the image to suppress the side-lobes as shown on the right columns. The plot on the bottom right is the SAL simulated image after the additive Gaussian noise is added for a CNR of 10 dB

# CHAPTER 4

# 3-D Image Reconstruction

In this chapter, we discuss the incoherent tomographic techniques and the backprojection algorithm which used to reconstruct 3-D images of targets. We also discuss the effect of angular diversity and number of observations on the reconstructed image. Furthermore, we investigate the way the speckle noise and the shot noise are affected as the number of detectors, angular diversity and number of observation angles are varied. Finally, we provide sample images for the 3-D reconstructed image for both the single and multiple slant plane reconstructions with and without slant plane overlap.

## 4.1 Tomographic Reconstruction

Computer-aided tomography (CAT) is a well-established technique for reconstructing high resolution images by processing data obtained from multiple observation angles of an object area [14]. The CAT scan is an x-ray technique allowing the imaging of 2-D cross-sectional view of a 3-D targets via digital processing of many 1-D projection views taken with different look angles [14]. The data collection geometry for the x-ray data, allowing the CAT reconstruction technique is shown in Figure 4.1

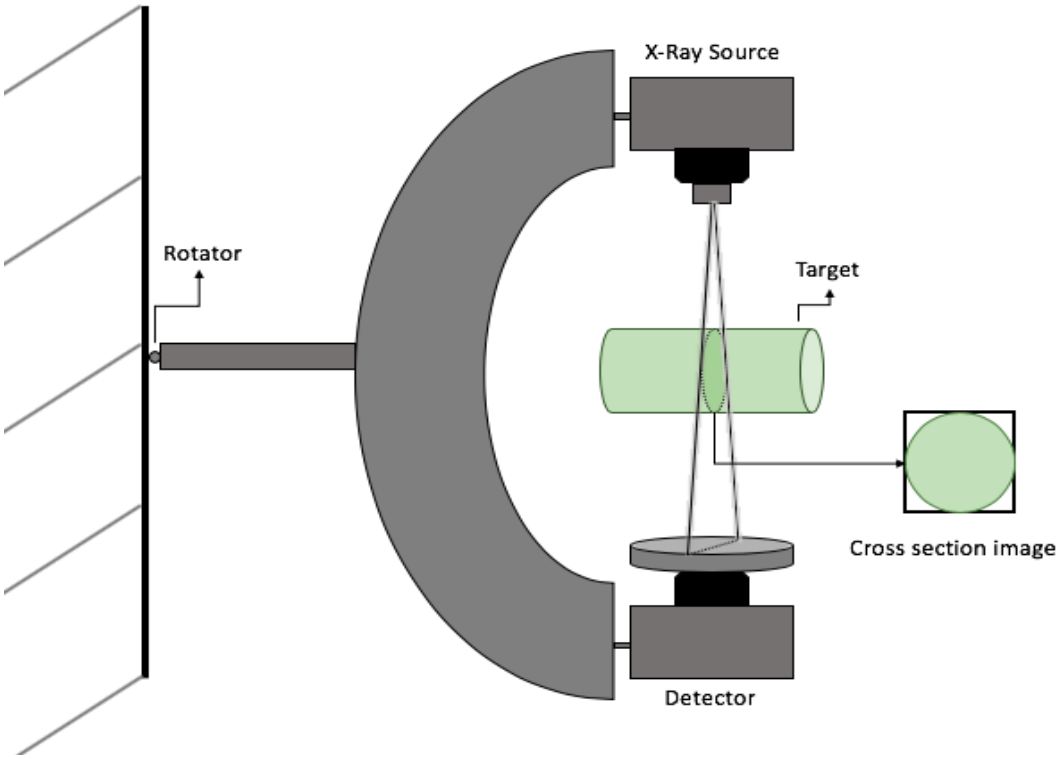


Figure 4.1: Procedure of x-ray CAT imaging.source: Author

It is shown [11] [14] that spotlight-mode SAR/SAL can be interpreted as a tomographic reconstruction problem, and the signal processing theory can be characterized in terms of the projection-slice theorem. The *projection slice* theorem states that the Fourier transform of the projection at angle $\theta$ is a "slice" of the 2-D transform $G(X, Y)$ taken at an angle $\theta$ with respect to the x-axis [14].

Assume $g(x, y)$ is the unknown signal that is to be reconstructed from its projections. The Fourier transform of $g$ is defined as:

$$G(X, Y) = \int_{-\infty}^{\infty} \int_{-\infty}^{\infty} g(x, y) e^{-j(xX+yY)} \mathrm{d}x\mathrm{d}y \tag{4.1}$$

The result of the transmitter and receiver translation is to take out a single projection, $P_\theta(u)$. The $(x, y)$ coordinate is related to the $(u, v)$ coordinate by rotating the x-axis coun-

terclockwise with respect to angle $\theta$ [11]. This orthonormal linear transformation is given as:

$$x = ucos\theta - vsin\theta \tag{4.2}$$

$$y = usin\theta + vcos\theta \tag{4.3}$$

This transformation is shown in Figure 4.1

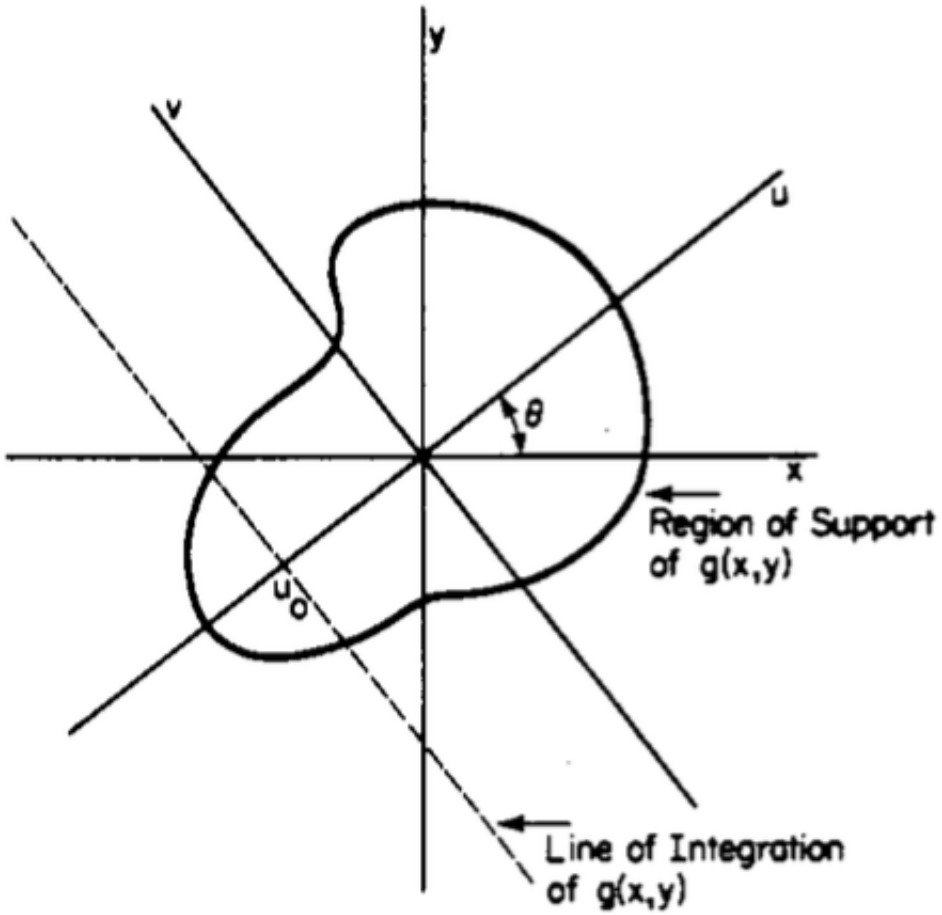


Figure 4.2: Line of integration for determining the projection. source: [14]

Using this geometry, the line of integration to find the projection $p_\theta(u)$ of the signal $g$ at angle $\theta$ is given as:

$$p_\theta(u) = \int_{-\infty}^{\infty} g(ucos\theta - vsin\theta, usin\theta + vcos\theta)\mathrm{d}v \tag{4.4}$$

$p_\theta(u)$ is series of line integrals at each values of angle $\theta$. The Fourier transform of $p_\theta(u)$ is given as:

$$P_\theta(U) = \int_{-\infty}^{\infty} p_\theta(u)e^{-juU}\mathrm{d}v \tag{4.5}$$

From this equation, we can see that the projection-slice theorem is simply:

$$P_\theta(U) = G(Ucos\theta, Usin\theta) \tag{4.6}$$

### 4.1.1 Backprojection Image Formation

There are several image formation techniques, however the most common ones are the back-projection algorithm and the direct Fourier algorithm also known as the polar format algorithm. The trade-off between these two algorithms is in the image quality and the computation complexity [9]. Both backprojection and polar format algorithm are computationally complex. However, the backprojection algorithm is more straight forward to implement [9]. Polar format algorithm is computationally less expensive due to its exploitation of the fast Fourier transform (FFT). Its computational complexity is in the order of $O(N^2 log_2 N)$. In the other hand, the back-projection algorithm is computationally more complex $O(N^3)$ [9]. However, it gives us the ability to add or subtract pulses in the image process [9]. Usually in the LADAR community, back-projection algorithm is used for image formation. Therefore, in this work we focused on backprojection algorithm instead of polar format algorithm to form images. The backprojection algorithm is defined in equation

$$g(\rho cos\phi, \rho sin\phi) = \frac{1}{4\pi^2}\int_0^{\theta} \mathrm{d}\theta \int_{-\infty}^{\infty} G(rcos\theta, rsin\theta)|r|\, e^{jr\rho cos(\phi-\theta)}\mathrm{d}r \tag{4.7}$$

Equation 4.6 stated that the Fourier transform of the projection at angle $\theta$ is a slice the of the 2-D transform $G(X, Y)$ taken at an angle $\theta$ with respect to the x-axis. Therefore, equation 4.7 can be rewritten as:

$$g(\rho cos\phi, \rho sin\phi) = \frac{1}{4\pi^2} \int_0^{\theta} \mathrm{d}\theta \int_{-\infty}^{\infty} P_\theta(r)|r|\, e^{jr\rho cos(\phi-\theta)} \mathrm{d}r \tag{4.8}$$

It has been proven [9] that equation 4.8 can be expressed in term of MATLAB's ifft as:

$$s(m, \tau_n) = K * fftshift[ifft(S(f_k, \tau_n))] * exp(\frac{j2\pi f_1(m-1)}{k\Delta f}) \tag{4.9}$$

where $s(m, \tau_n)$ is the reconstructed signal given the phase history $S(f_k, \tau_n)$, collected by $N_p$ pulses. $K$ is the frequencies sample for each pulse, $f_1$ is the minimum frequency for every pulse, $\Delta f$ is the frequency step size of the sensor, $m$ is the range bin and $\tau$ is the slow time sample.

When the SAL slant plane images are incoherently combined for tomographic reconstruction, the speckle noise and the shot noise of the slant plane images gets beat down by $\sqrt{n}$ for each projection, $n$ is the number of projection. This is because at each look angle the signal is correlated, while the noise is uncorrelated and this uncorrelated noise will average out as the number of realizations are increased.

## 4.2 Exemplary results for 3-D Reconstructed Image

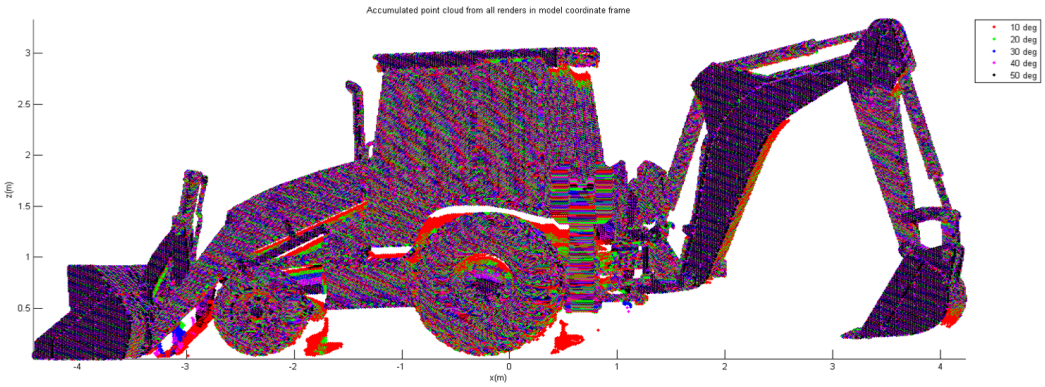


Figure 4.3: Color coded ”Super Point cloud”.

In order to measure the efficacy of the 3-D reconstructed image we need to compare it to the truth data. Image 4.3 is the accumulation of all the data points that was used for the tomographic reconstruction in the model coordinate frame. This point cloud was color coded to show the observation angles used to generate these points, because some points are only visible at some observation angles. This point cloud is termed as the ”super point cloud”, because it contains all the points that will be used to generate the tomographic reconstruction of the backhoe data. This super point cloud is Taylor window filtered to a 10 cm resolution grid and down sampled, and it will be used as the truth data as shown on table 4.4. The truth data is an intensity image with neither speckle nor shot noise.

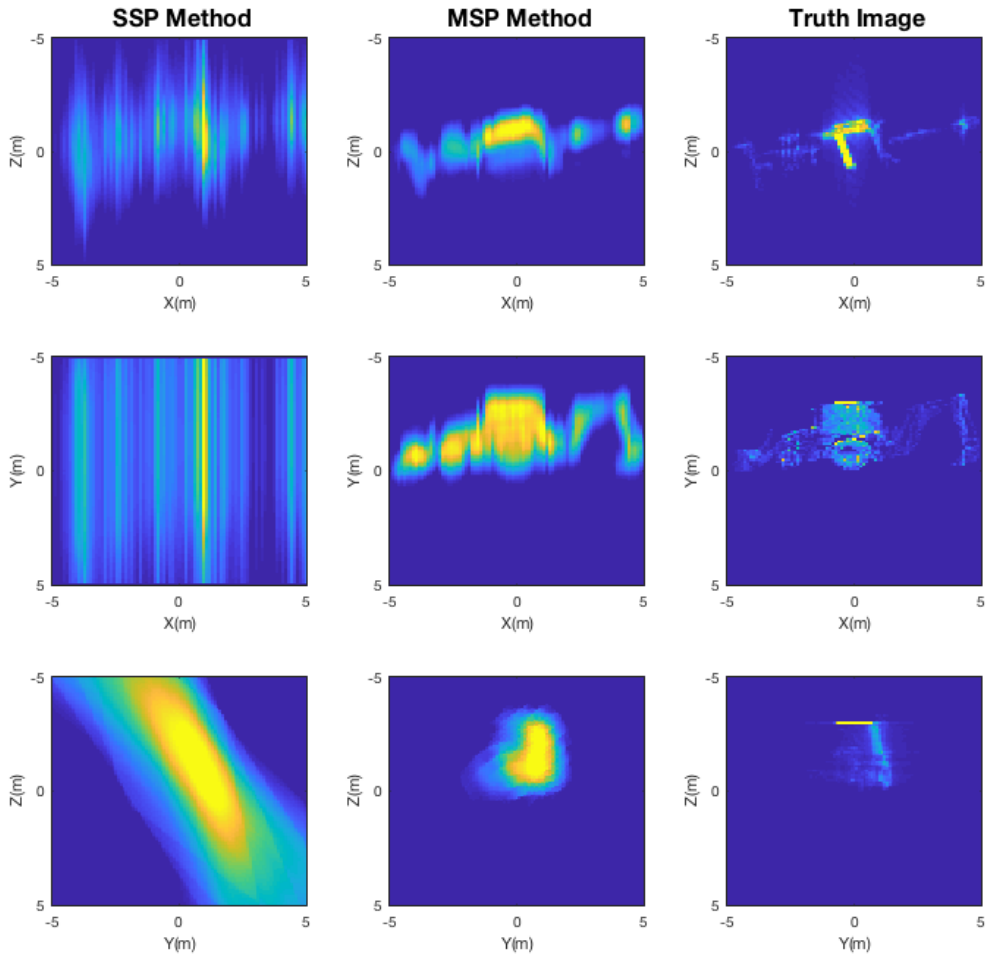


Figure 4.4: 2-D representative of the 3-D tomographic reconstruction of the backhoe shown in each plane in the model coordinate frame.

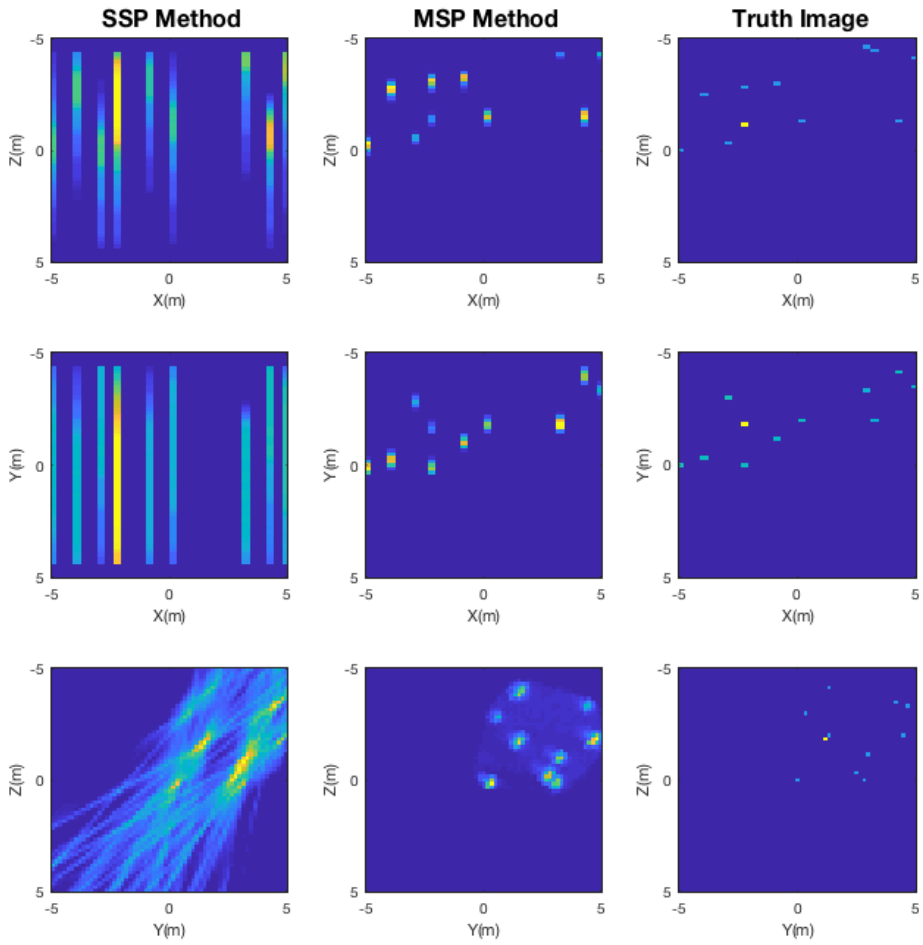


Figure 4.5: 2-D representative of the 3-D tomographic reconstruction of the Point Target shown in each plane in the model coordinate frame.

In Figures 4.4 and 4.5 we are showing a 2-D representation of the 3-D tomographic reconstruction image of the backhoe and point target data at each plane, respectively. The 2-D images were generated by summing along one-dimension of the 3-D reconstructed images. Five observation angles with $40^\circ$ angular diversity from $10^\circ$ to $50^\circ$ elevation angles were used to form these images. The images on the left are the resultant image when using the single slant plane method. The images in the middle are the resultant image when using

multiple slant plant image with 1 m slant plane spacing and 50% overlap. There was 50% overlap between the detectors. The images on the right are the truth intensity images after filtering and down-sampling the 1 cm super point cloud into the 10 cm 3-D grid.

In Figures 4.4 and 4.5, we observe that the 2-D rendering of the 3-D reconstructed image of the backhoe is qualitatively better resolved using the multiple slant planes compared to the single slant method. A quantitative metric will be used to evaluate these images in Section 6.1

# CHAPTER 5

# Metric of goodness

In this chapter, we explore the metrics for measuring the efficacy of the 3D tomographic reconstructions. The metrics that will be covered in this section are: the similarity metric and the joint information density metric. The similarity metric and the joint information density metric will be use as metric of goodness. Furthermore, we explored the Kullback-Leibler divergence and compared it to similarity metric.

## 5.1 Mutual Information

After the single and multiple slant plane tomographic reconstructions have been developed and simulated in MATLAB, methods for measuring the information content of this imagery need to be developed to determine how much valuable information do the SAL images have about the object in the scene, and how this information will change as the number of slant planes varied, and other degrees of freedoms such as elevation angle and noise. As a quantitative metric mutual information (MI) is used in this research. MI calculates the similarity between two random variables. In this research, MI was used to calculate the

similarity between two images.

$$I(X,Y) = H(X) + H(Y) - H(X,Y) \tag{5.1}$$

Where, $I(X,Y)$ is the mutual information between image $X$ (the truth image) and image $Y$ (the reconstructed image). $H(X)$ is the entropy of image $X$, $H(Y)$ is the entropy of image $Y$, and $H(X,Y)$ is the joint entropy between image $X$ and image $Y$. *Entropy* measures the amount of information in a random variable, in order word it measures the uncertainty of a random variable. The entropy is expressed in bits when the $log$ is to the base 2, and in nats when the log is base $e$. In this work, we take all logarithms to the base 2, and this is known as the Shannon entropy.

$$H(X) = -\sum_{i} P_i * \log_2(P_i) \tag{5.2}$$

$$H(Y) = -\sum_{j} P_j * \log_2(P_j) \tag{5.3}$$

$$H(X,Y) = -\sum_{i}\sum_{j} P_{ij} * \log_2(P_{ij}) \tag{5.4}$$

To aid interpretation we converted the mutual information metric from bits to a similarity metric in percentage by taking the ratio of $I(X,Y)$ and $I(X,X)$ and multiplied it by 100 as shown in equation 5.5. Where $I(X,X)$ is equal to the Shannon entropy of $X$ ($H(X)$)

$$SIP = \frac{I(X,Y)}{I(X,X)} * 100 \tag{5.5}$$

$SIP$ is the similarity in percentage between the truth and reconstructed image. This similarity metric will be used to quantify how good the reconstructed images represent the

truth image.

Since we are investigating the information content of the image and noise is information. This means that not all the information content in the image is useful information. Therefore, tracking the amount of join information density (JID) in the images will help us have a better interpretation on how the similarity is affected by noise. JID track the amount of useful information of the image as the CNR is being varied. In equation 5.6 we define the JID

$$JID = \frac{I(X,Y)}{I(Y,Y)} * 100 \tag{5.6}$$

where JID is the ratio of the mutual information of the truth and the reconstructed image to the mutual information of the reconstructed image by itself.

## 5.2 Entropy Study

In image processing, entropy measures the amount of information or the uncertainty of an image. In this study we measured the entropy of the 2-D SAL images of the target to be projected onto the tomographic plane, and observed the way the entropy is changing as the level of noise, and the location of the sensor is varied. Figure 5.3, and Figure 5.4 show the trend of the entropy as the level of CNR is being varied. The different colored lines of these plots represent the 2-D SAL image of the target at different elevation angles. From these plots we observed that as noise decreases the entropy of the image decreases as well; this is because noise is information. Furthermore, from these figures, we observed that the entropy of the 2-D SAL images change at each observation angle for the unstructured target; this is because at each look angle a random instance of noise is generated for the SAL image at the observation angle.

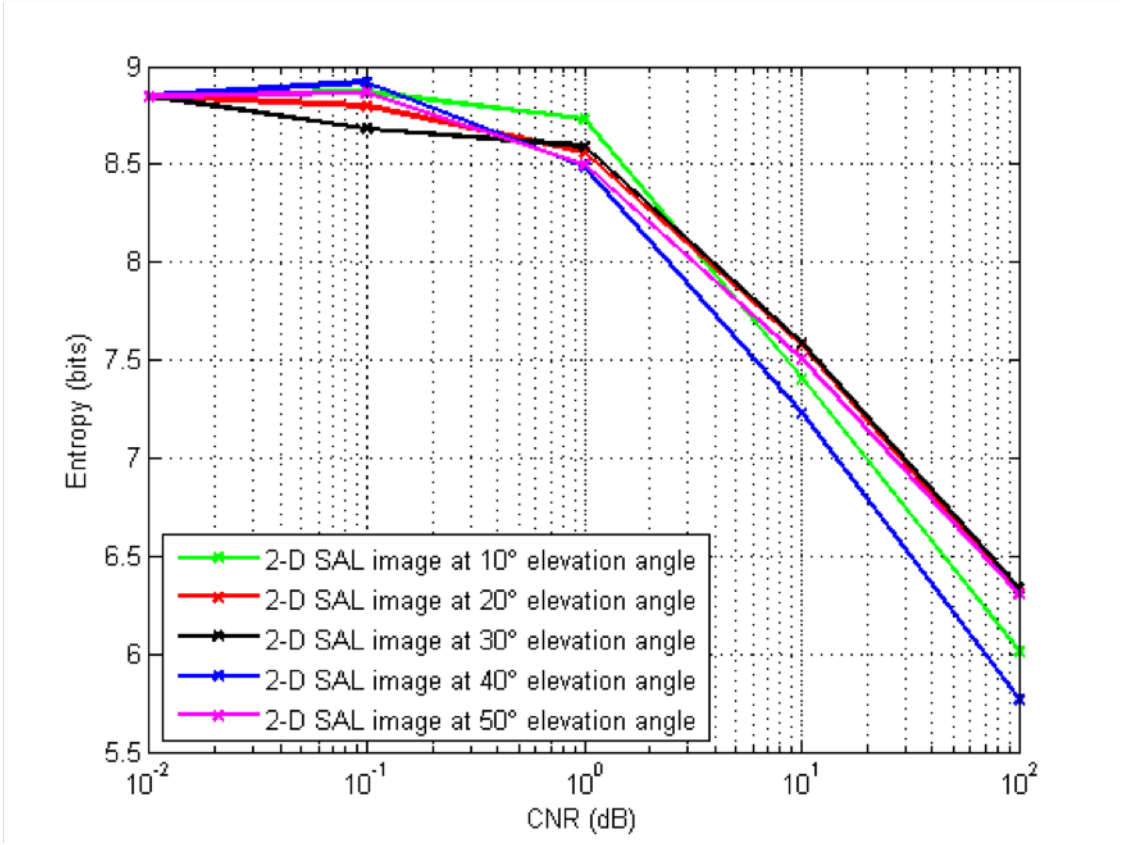


Figure 5.1: Unstructured Target Single Slant Plant: Entropy vs. CNR study.

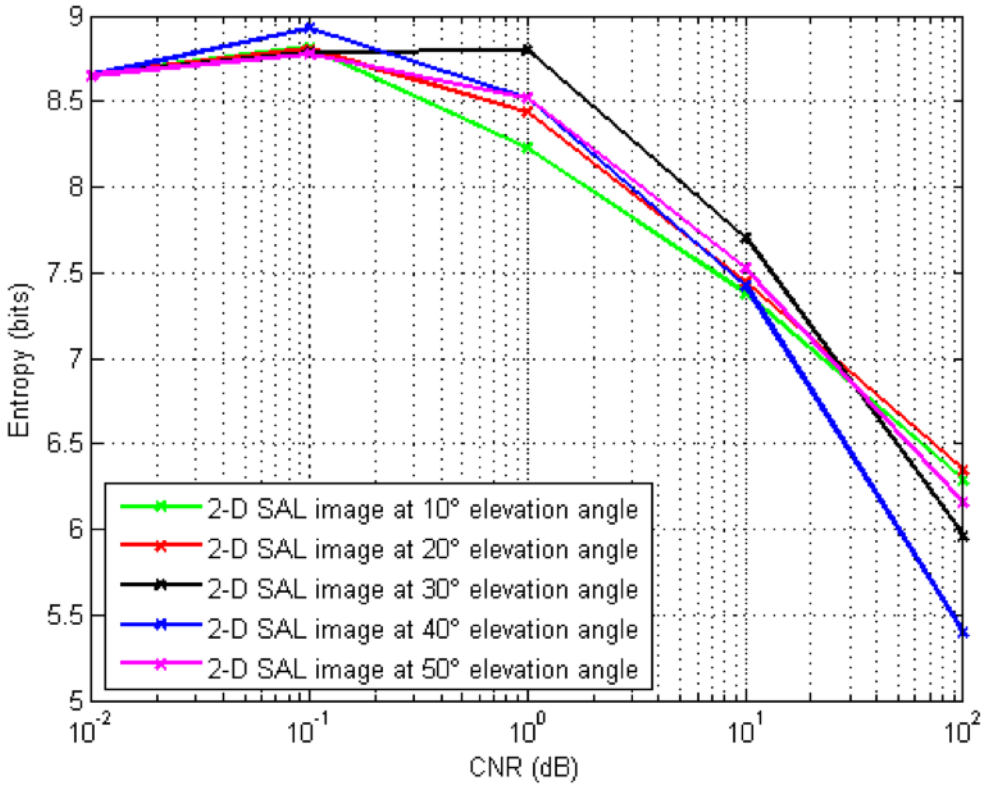


Figure 5.2: Unstructured Target Multiple Slant Plant: Entropy vs. CNR study.

For the multiple slant plane, we summed all the slant plane at each observation angle and calculate the entropy. We notice that the entropy for the multiple slant plane and single plane reconstruction are similar in this case; this is because for the multiple slant plane method the SAL images were generated using the 0% overlap method. In this method, every point in the point cloud is just sampled once. Therefore, when we sum all the slant planes we should get the same amount of information as the single slant plane method. In this case there is a little difference, because a new random draw of noise is generated for each SAL image.

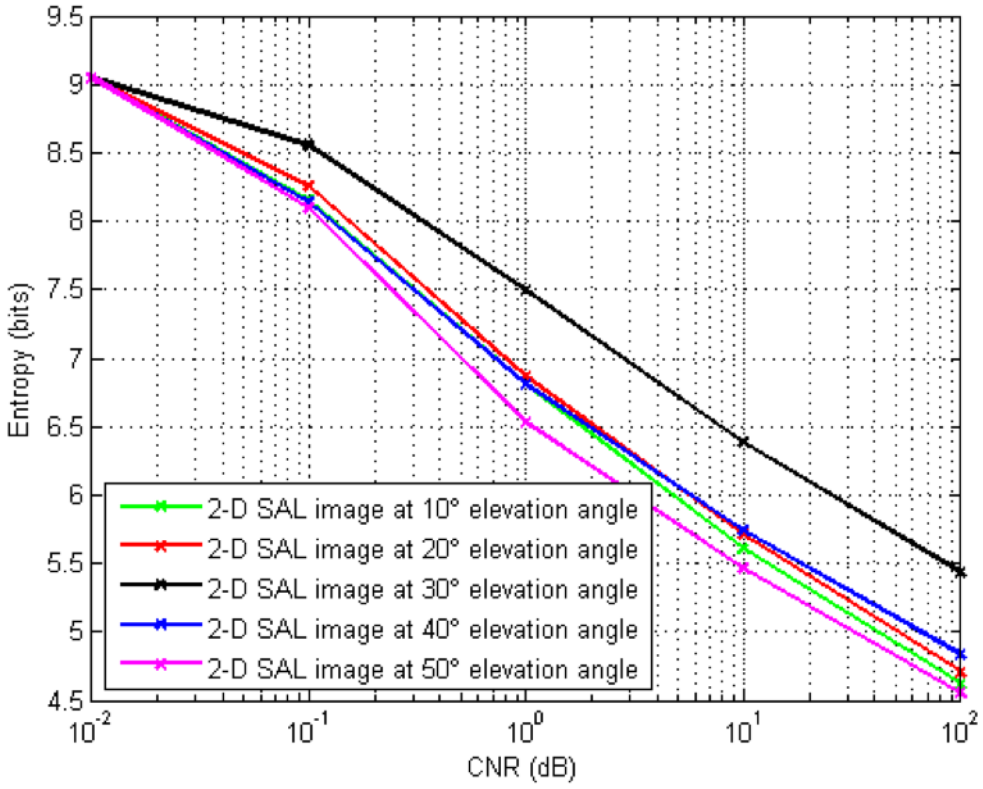


Figure 5.3: Structured Target Single Slant Plant: Entropy vs. CNR study.

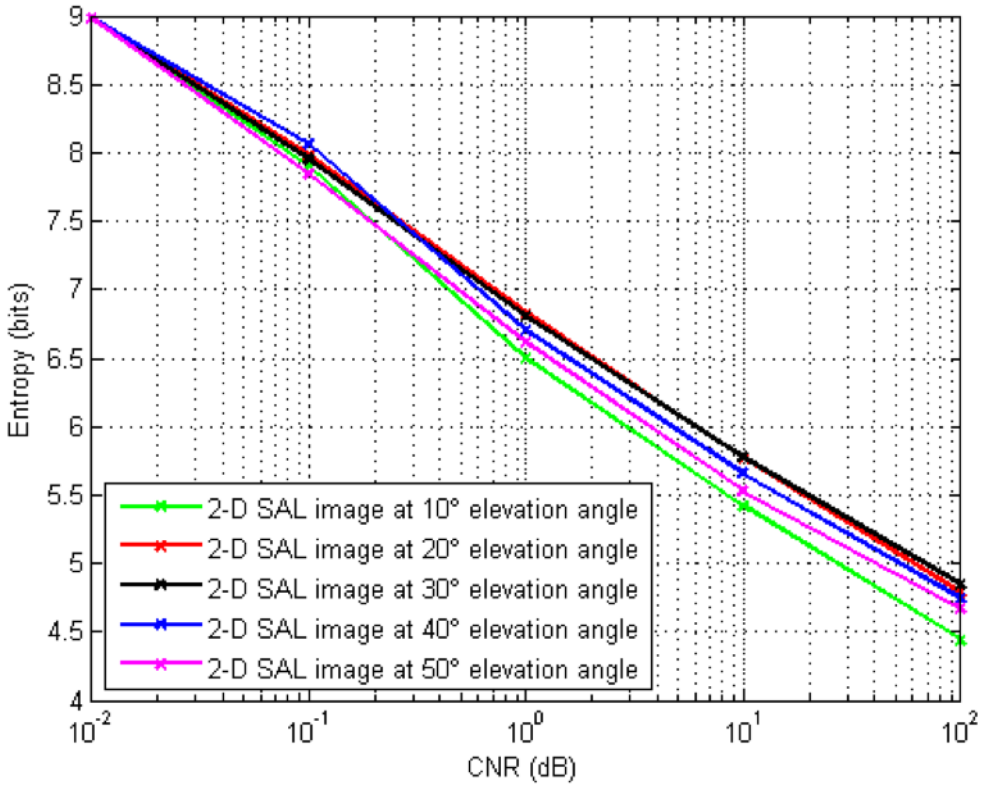


Figure 5.4: Structured Target Multiple Slant Plant: Entropy vs. CNR study.

## 5.3 Study on Mutual Information in intensity image vs speckle vs shot noise image and registration study

As noted in Section 4.2, the truth images for both the point target and the backhoe data are intensity images without noise. While the reconstructed images have both multiplicative noise (speckle noise) and additive noise (shot noise). Therefore, in this section we study the maximum amount of mutual information one can achieve when comparing a pure intensity image with a speckle image and a shot noise image. In this study, we used the build-in "cameraman" in MATLAB, which is an intensity image and set it be the truth image ($X$).

A speckle image $Y_{speckle}$ and a shot noise image $Y_{shot}$ of the cameraman are generated as expressed in equations 5.8 and 5.9, respectively. The CNR is the same as defined equation 2.5, it is the ratio of the signal power to the noise power.

$$X = cameraman.tif \tag{5.7}$$

$$Y_{speckle} = X * \frac{randn(size(X))}{\sqrt{n}} \tag{5.8}$$

$$Y_{shot} = X + \sigma^2 * \frac{randn(size(X))}{CNR * \sqrt{n}} \tag{5.9}$$

Where, $\sigma^2$ is tied to the mean of the intensity image $X$. From $Y_{speckle}$, we can see that the speckle noise gets beat down by square-root of the number of iterations $n$. The number of iterations will represent to the number of observation angles or number of projections when performing tomographic reconstruction. From $Y_{shot}$, we can see that the noise factor depends on both the CNR and the number of iterations.

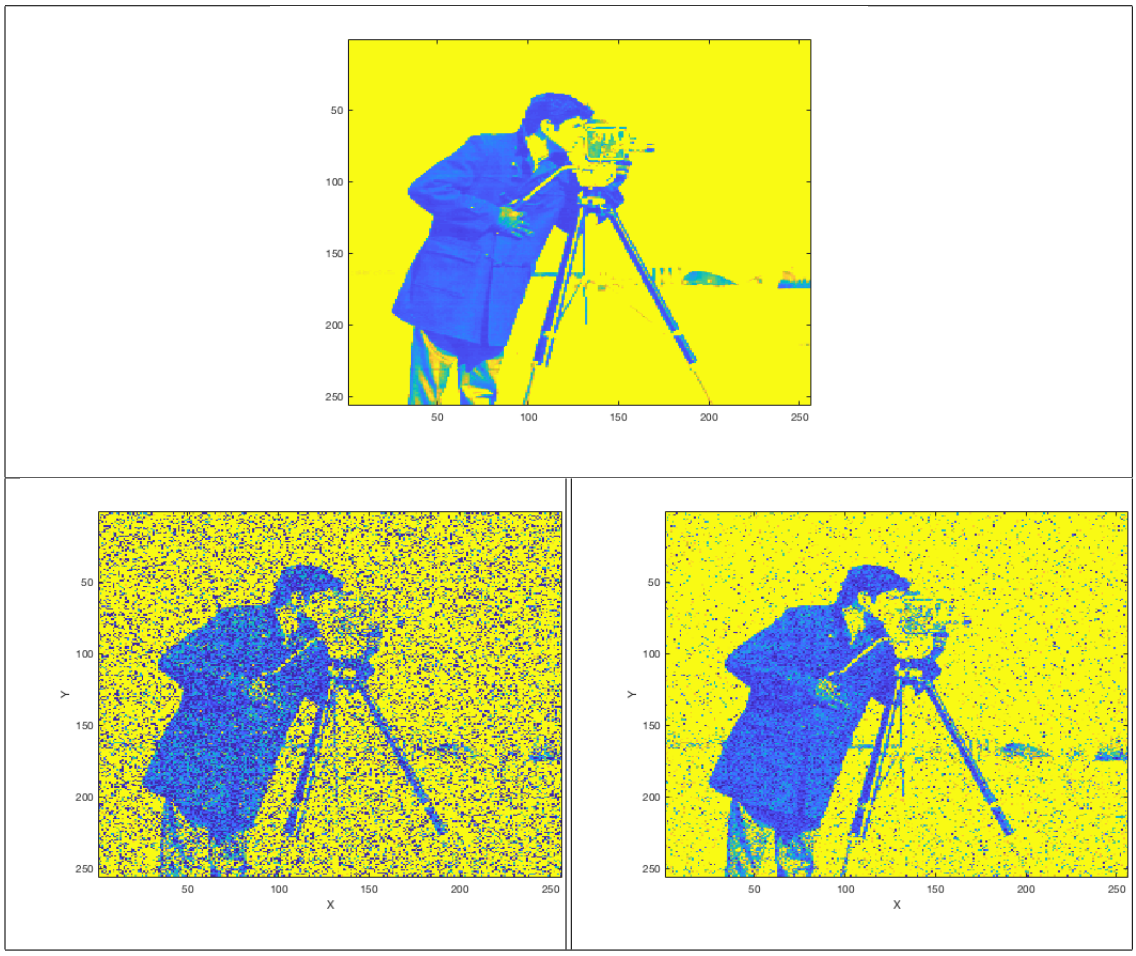


Table 5.1: Effect of speckle noise when comparing a noiseless intensity image with a speckle image

To measure the total amount of mutual information achievable between a noiseless intensity image, and a speckle image. We use the built-in MATLAB image ”cameraman.tif” to be the original image as shown on top of Table 5.1. We then took the original image and multiply it by a random Gaussian distribution function, we then divided by the square-root of the number of iterations or observation angles as shown in equation 5.8 to generate speckle noise to the original image which is a multiplicative noise. The speckle images are shown on the bottom of table 5.1. The image on the bottom left represents the speckle image of the cameraman for 1 iteration, and the image on the bottom right represents the speckle image of the cameraman after 5 iterations. Figure 5.5 shows the maximum sim-

ilarity in percentage we can achieve when comparing a noiseless intensity image with a noisy speckle image. From Figure 5.5 we see that as the number of speckle averaging increases the similarity between the truth and the reconstructed image increases as well. This is because as the number of speckle averaging increases the signal correlates, and the noise decorrelates and averages out. As we go to infinity the two images become identical and the similarity approaches 100%. **Note** this similarity depends on the total information in the image.

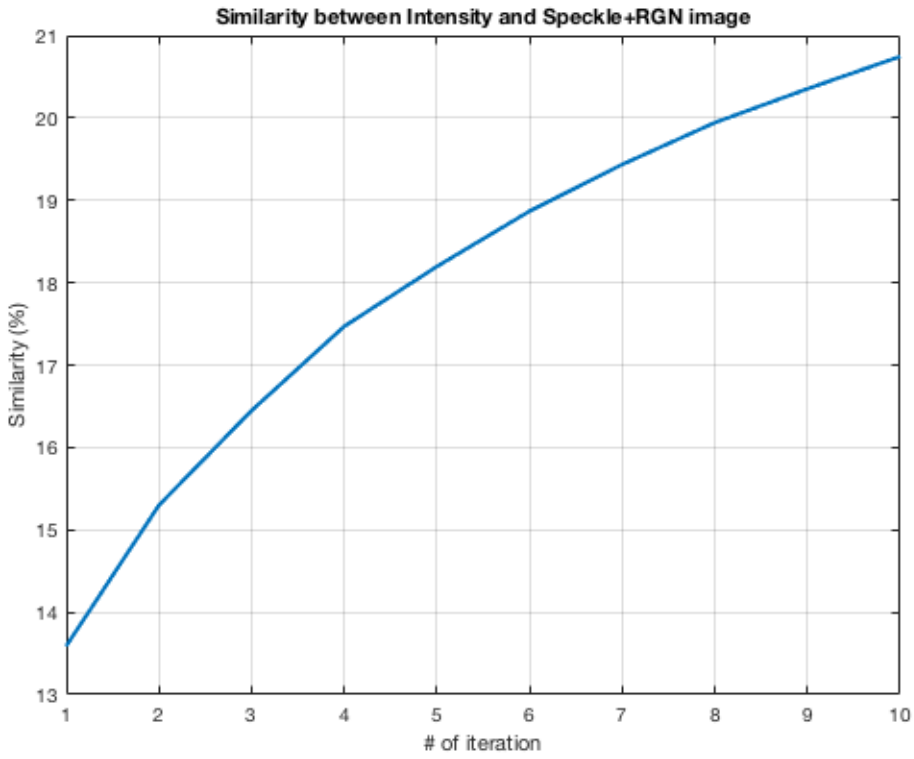


Figure 5.5: Noiseless Intensity image vs. Speckle averaging

Another study was done to measure the total amount of mutual information one can achieve when comparing a noiseless intensity image with an image corrupted with shot noise image. Shot noise is additive noise and can be modeled with a Gaussian distribution function. Sample images are shown in table 5.2. From Figure 5.3, we observed that the

similarity between the two images increases as the number of averaging increases. For the shot noise image, the similarity also depends on the level of CNR, in this example we use CNR of 1 dB on the shot noise image.

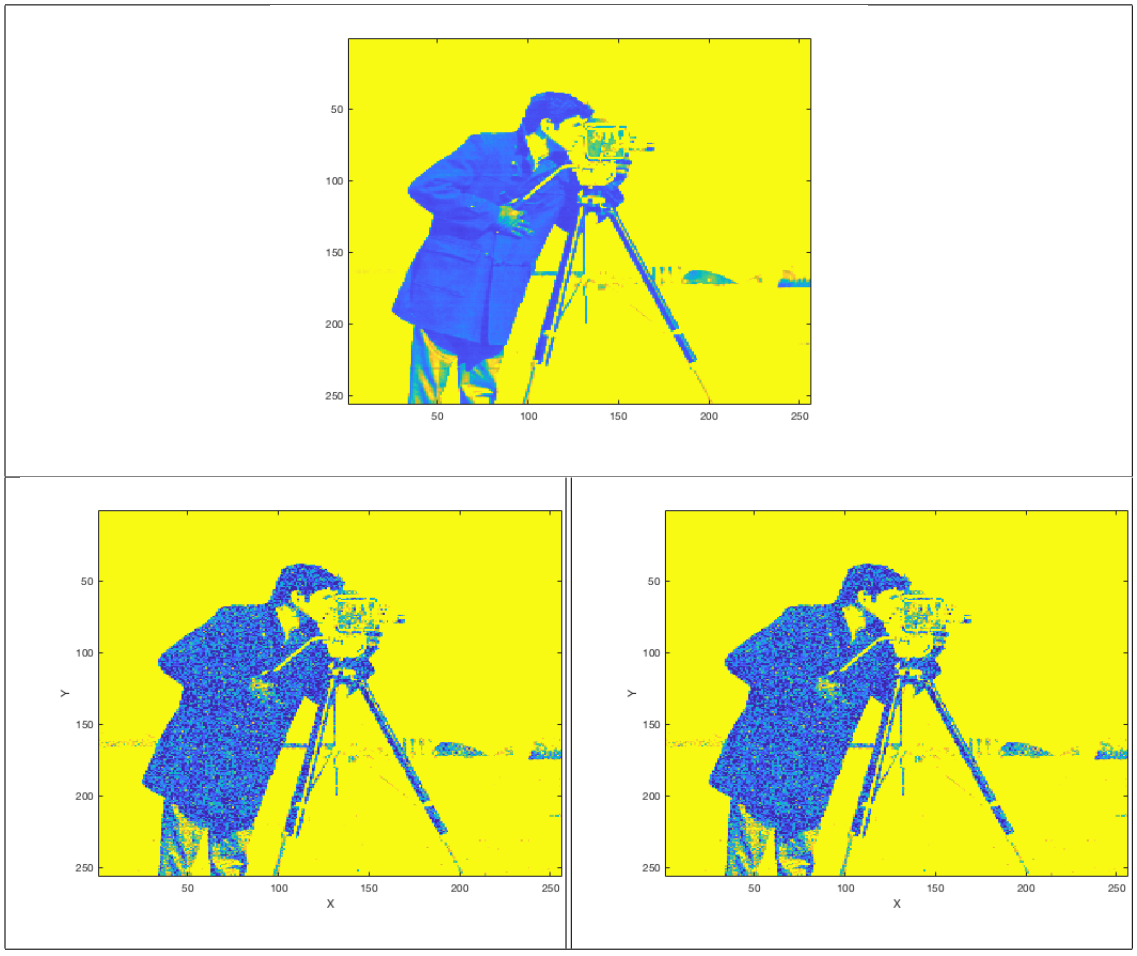


Table 5.2: Effect of speckle noise when comparing a noiseless intensity image with a speckle image

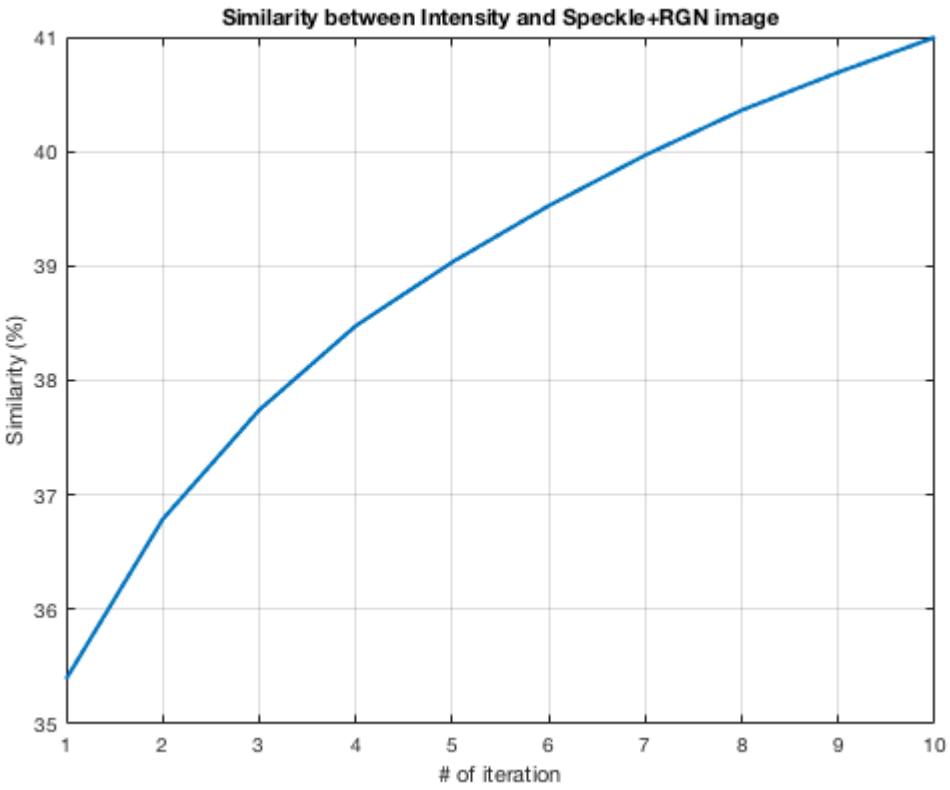


Figure 5.6: Noiseless Intensity image vs. Shot noise averaging

### 5.3.1 Registration Study

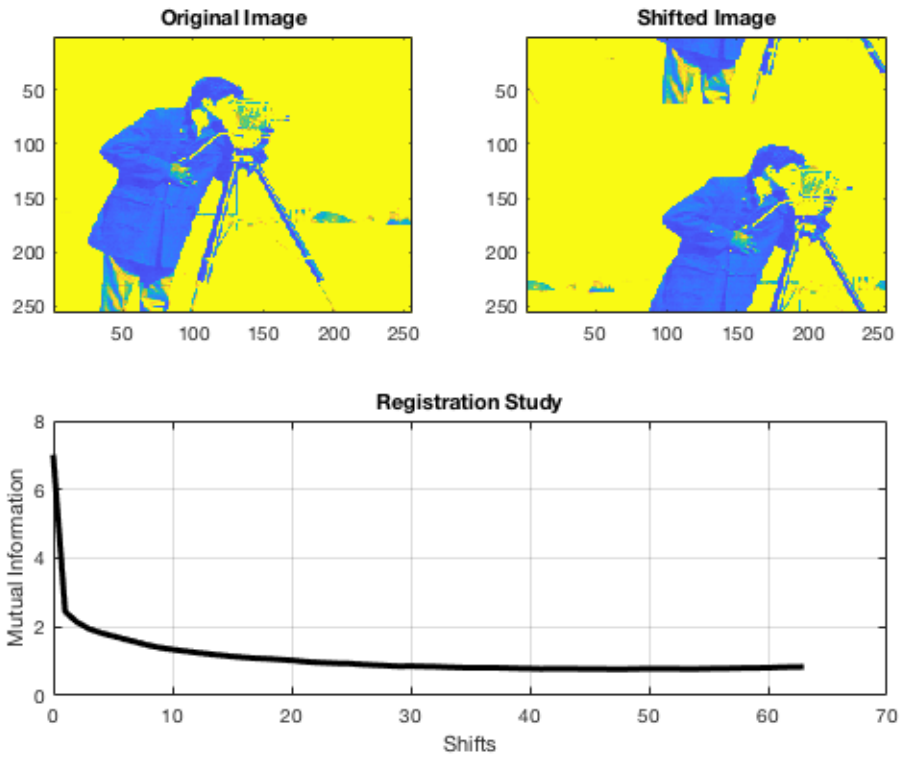


Figure 5.7: Effect of mutual information when the two images are not properly registered.

Figure 5.3.1 shows the effect of the mutual information when the images to be compared are not properly registered. We can see from these results that precise registration is required in order to calculate the mutual information between the images. We can also observe from Figure 5.3.1 that the mutual information takes account of the spatial location of the information. The two images in Figure 5.3.1 have the same amount of entropy. However, the spatial location of the information are different, we can see that the mutual information decreases as the spatial location of the information is different. The entropy of the image does not change. Therefore, the similarity metric has shift dependence and the 2 images must be accurately registered for the use of the similarity metric.

## 5.4 Sample Image

In this section, we show some sample image of the 3-D tomographic reconstruction of the backhoe data. These images are shown in the Z vs Y dimension at X (along-track-cross-range) position. To quantify these results, we calculate the mutual information between the reconstructed image and the truth image as show in Figure 5.8.

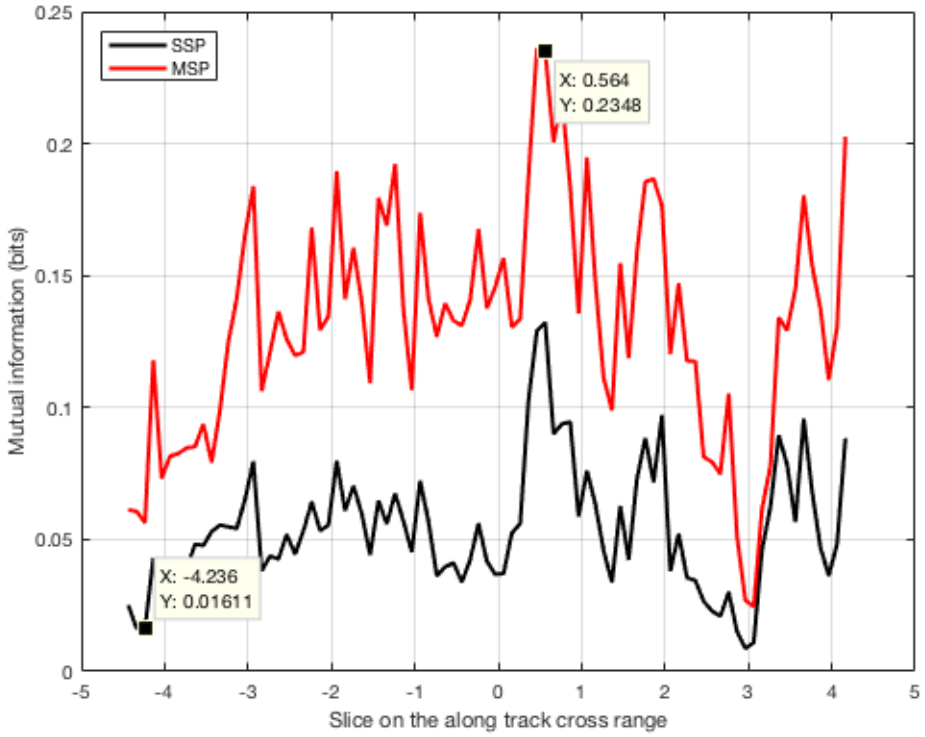


Figure 5.8: Mutual Information between truth image and reconstructed image for each slice of the 3-D backhoe image.

In Figure 5.8, the black line represents the mutual information between the truth and the reconstructed image using single slant plane method, and the red line represents the mutual information of the two images using multiple slant plane method. Higher mutual information gain is obtained on the reconstructed image when using multiple slant plane

method. Note that this is the mutual information of each slices of the volume, and the mutual information of the whole 3-D volume is much greater than 0.1 bits

Figure 5.9 we show a slice of the synthesized plane for backhoe data where the mutual information is high for both tomographic reconstructions, and in Figure 5.10 we show a slice of the backhoe data where the mutual information is low. For each of the figures 5.9 and 5.10, the plot on the left represents the slice of the resultant image using the single slant plane method. The middle plot represents a slice of the resultant image using the multiple slant plane method, and the image on the right is a slice of the truth image of the backhoe

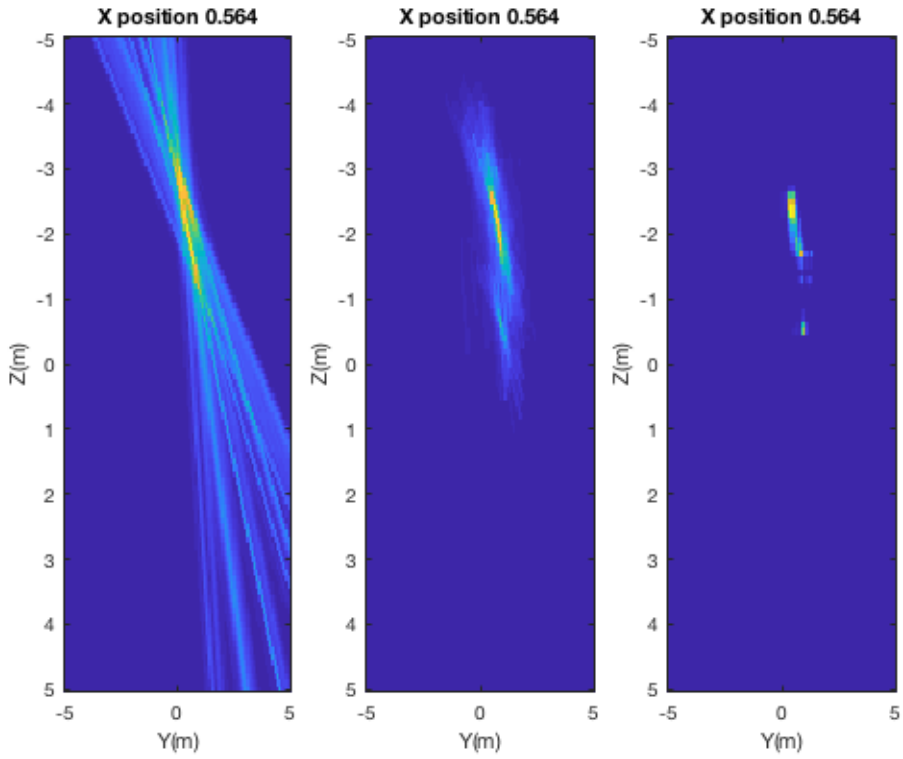


Figure 5.9: A slice of the 3-D tomographic reconstruction of the backhoe at along track position of 0.564

Figure 5.9 shows a slice of the 3-D reconstruction volume of the backhoe in the synthesized plane of model coordinates (Y,Z). This slice is at along-track-cross-range (X) position

of 0.564 m, where in this position we have the maximum amount of mutual information shown in image 5.8. These images are slices of the reconstructed image for single slant plane method on the left, multiple slant plane method in the middle and truth image on the right. For better visualization these images were generated without noise. We projected five angles with $40^\circ$ angular diversity using observations at $10^\circ$, $20^\circ$, $30^\circ$, $40^\circ$ and $50^\circ$ elevation angle

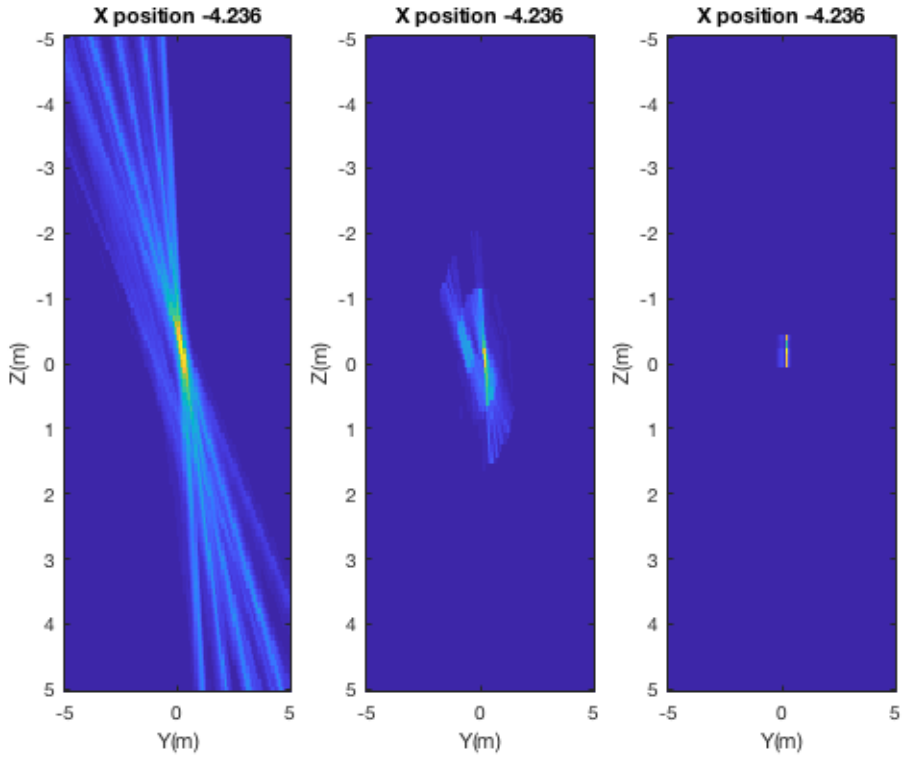


Figure 5.10: A slice of the 3-D tomographic reconstruction of the backhoe at along track position of -4.236 m

Figure 5.10 shows a slice of the 3-D reconstruction volume of the backhoe in the synthesized plane of model coordinates (Y,Z). This slice is at along-track-cross-range (X) position of -4.236 m, where in this position we have the minimum amount of mutual information as shown in image 5.8. These images are slices of the reconstructed image for

single slant plane method on the right, multiple slant plane method in the middle and truth image on the right using the same data as Figure 5.9.

### 5.4.1 2-D representation of the 3-D tomographic reconstruction

In this section, we show the 2-D representation of the 3-D reconstructed image of the backhoe data. From the following images we can qualitatively, and quantitatively compared the reconstructed images of the different methods.

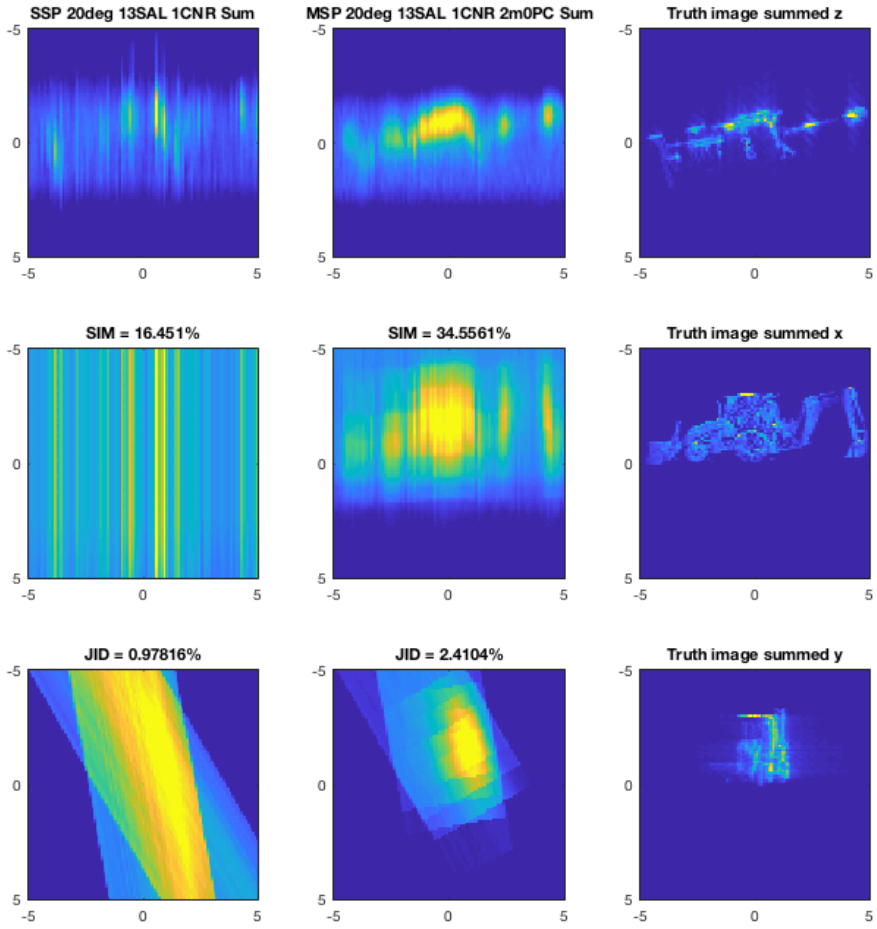


Figure 5.11: 2-D representative of the 3-D tomographic reconstruction of the backhoe shown in each plane.

In Figure 5.11 we are showing a 2-D representation of the 3-D tomographic reconstruction image of the backhoe data at each plane. The 2-D images were generated by summing along one dimension of the 3-D reconstruction. Two observation angles with $20^{\circ}$ angular diversity was used to form these images. The two observation angles were at $10^{\circ}$ and $30\circ$ elevation. The images on the left are the resultant image when using the single slant plane method. The images in the middle are the resultant image when using multiple

slant plant method. There was no overlap between the detectors, and the slant plane heights of the detectors are 2 m. The images on the right are the truth intensity image after filtering and down-sampling the 1 cm super point cloud into the 10 cm 3-D grid.

From Figure 5.11 we observe that the 2-D rendering of the 3-D reconstructed image of the backhoe is qualitatively better resolved using the multiple slant planes compared to the single slant method. The similarity (SIM) and the join information density (JID) are displayed on in Figure 5.11.

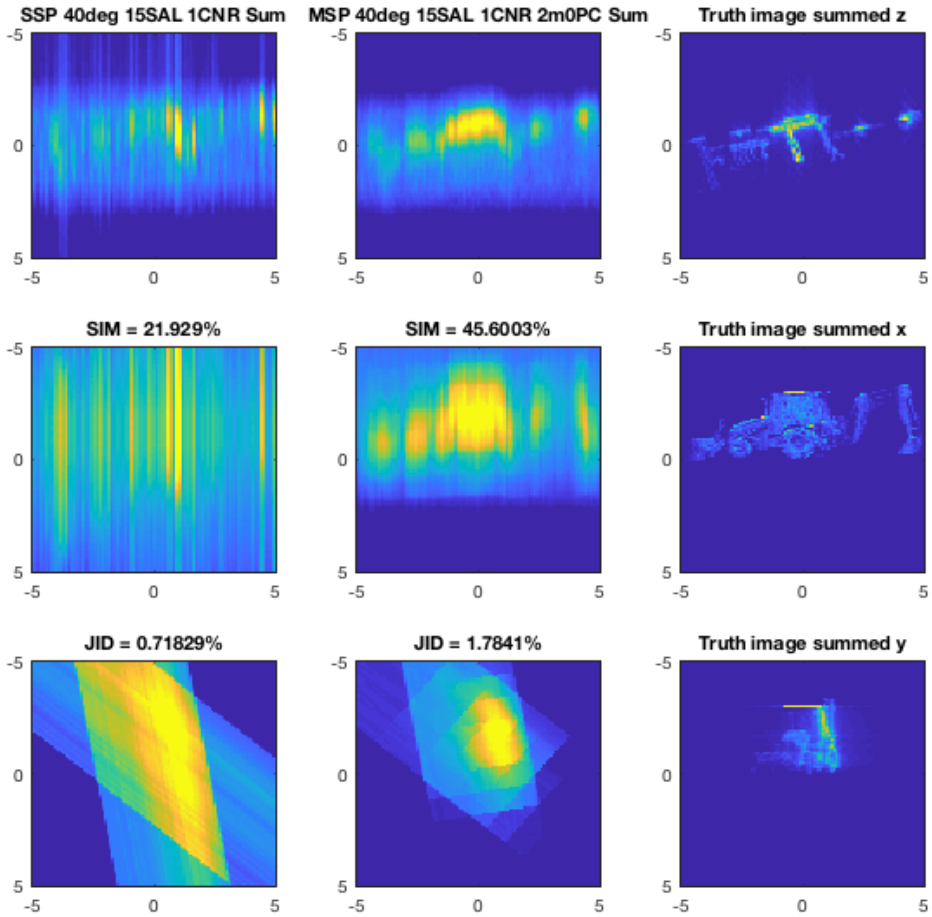


Figure 5.12: 2-D representative of the 3-D tomographic reconstruction of the backhoe using two projections with 40◦ angular diversity and 1dB CNR.

In Figure 5.12 the angular diversity between the projections is increased from 20° to 40◦. It shows that increasing the angular diversity will help increase the similarity.

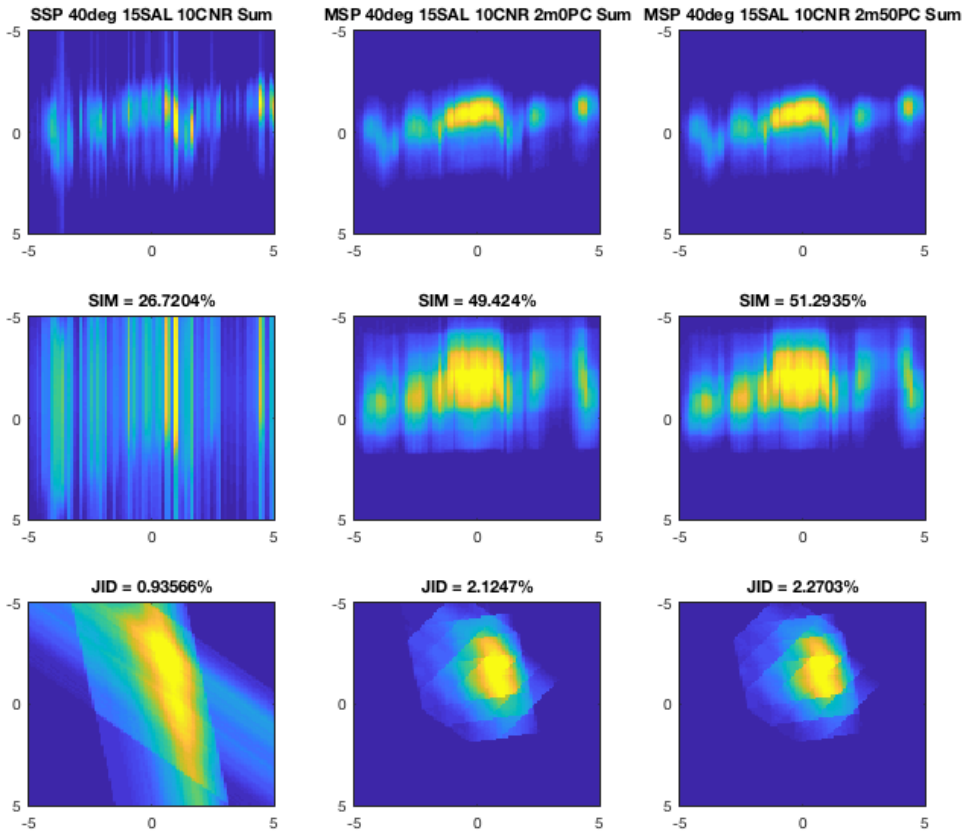


Figure 5.13: 2-D representative of the 3-D tomographic reconstruction of the backhoe using two projections with $40\circ$ angular diversity and 1dB CNR.

In Figure 5.13 we increased the CNR from $1dB$ to $10dB$. The images on the left are the resultant image when using the single slant plane method. The images in the middle are the resultant image when using multiple slant plant method with no overlap between the detectors and 2m slant plane height. The images on the right are the resultant image when using multiple slant plant method with 50% overlap between the detectors and 2m slant plane height. From this figure, we observe that as the noise level in the reconstructed image decreases, its similarity between the truth image increases.

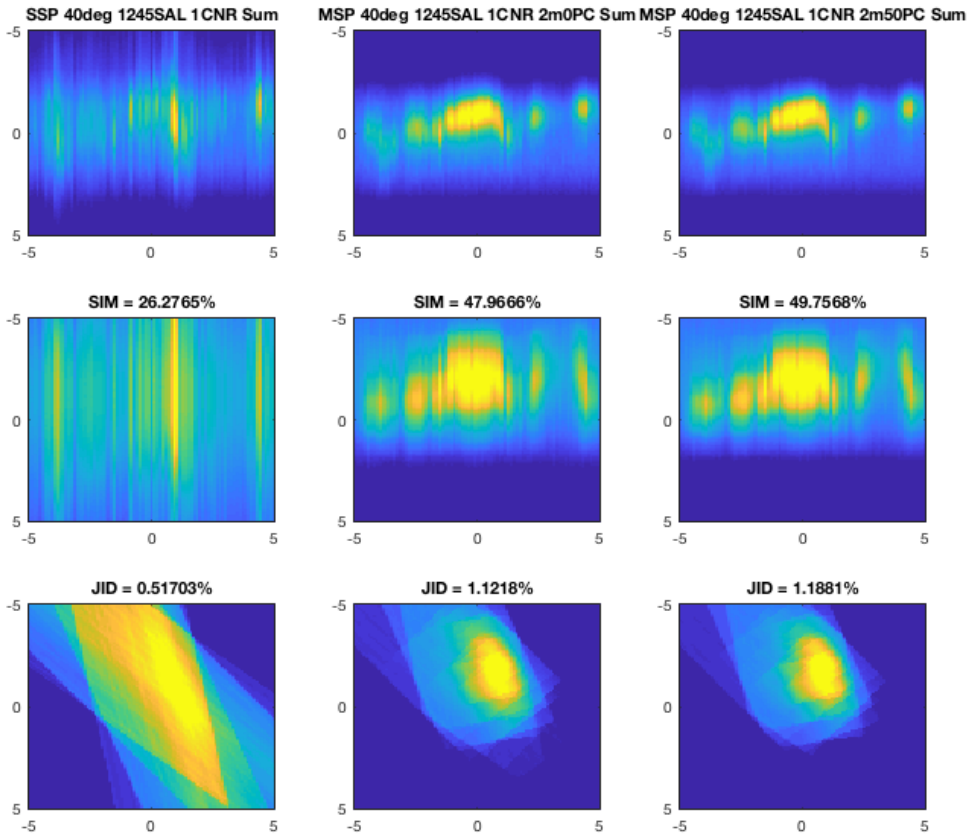


Figure 5.14: 2-D representative of the 3-D tomographic reconstruction of the backhoe using four projections with $40^{\circ}$ angular diversity and 1dB CNR.

In Figure 5.14 we increased the number of observation angles from two observation angles to five observation angles, and a CNR of $1dB$. When comparing Figure 5.12 and figure 5.14, we can see that when we increased the number of observation angles the similarity increases, but mostly on the multiple slant plane method. However, for the single slant plane method number observation angles don't have a big effect on the similarity.

### 5.4.2 Kullback-Leibler divergence

To back-up the results obtained with the similarity metric, we introduce the Kullback-Leibler divergence. Kullback-Leibler divergence also known as relative entropy is a measure of the distance between two probability mass function [4]. It is call Kullback-Leibler divergence instead of Kullback-Leibler distance, because it is not symmetric [4]. Since Kullback-Leibler divergence is not symmetry, therefor it is not a true metric. However, it has most properties of a metric. It is commonly used to a measure the relation between two random variables using their probabilities distributions [4]. The Kullback-Leibler divergence between two probability mass functions p(x) and q(x) is defined as

$$D(p||q) = \sum_{x \in X} p(x) * \log \frac{p(x)}{q(x)} \tag{5.10}$$

$$D(p||p) = 0 \tag{5.11}$$

$$D(p||q) \geqslant 0 \tag{5.12}$$

Where $D(p||q)$ is the Kullback-Leibler divergence between the two probability mass functions $p$ and $q$. In Figure 5.15, 5.16 and 5.17 we are showing a 2-D representation of the 3-D tomographic reconstruction image of the backhoe data at each plane. The 2-D images were generated by summing along one dimension of the 3-D reconstructed images. These images were generated using four projections angle with an angular of $40°$. For each of these figures, the left columns represent the 3-D reconstructed image using the single slant plane method, the middle columns represent the 3-D reconstructed image using the multiple slant plane method without overlap between the detectors, and the right columns represent the 3-D reconstructed image using the multiple slant plane method with $50\%$ overlap between the detectors. We displayed the similarity and the Kullback-Leibler

divergence results for each reconstructed image. From these results we can see that the Kullback-Leibler divergence results agreed with the similarity results. We observed from these figures that when we increase the CNR, we have a higher similarity and the Kullback-Leibler divergence deacreases.

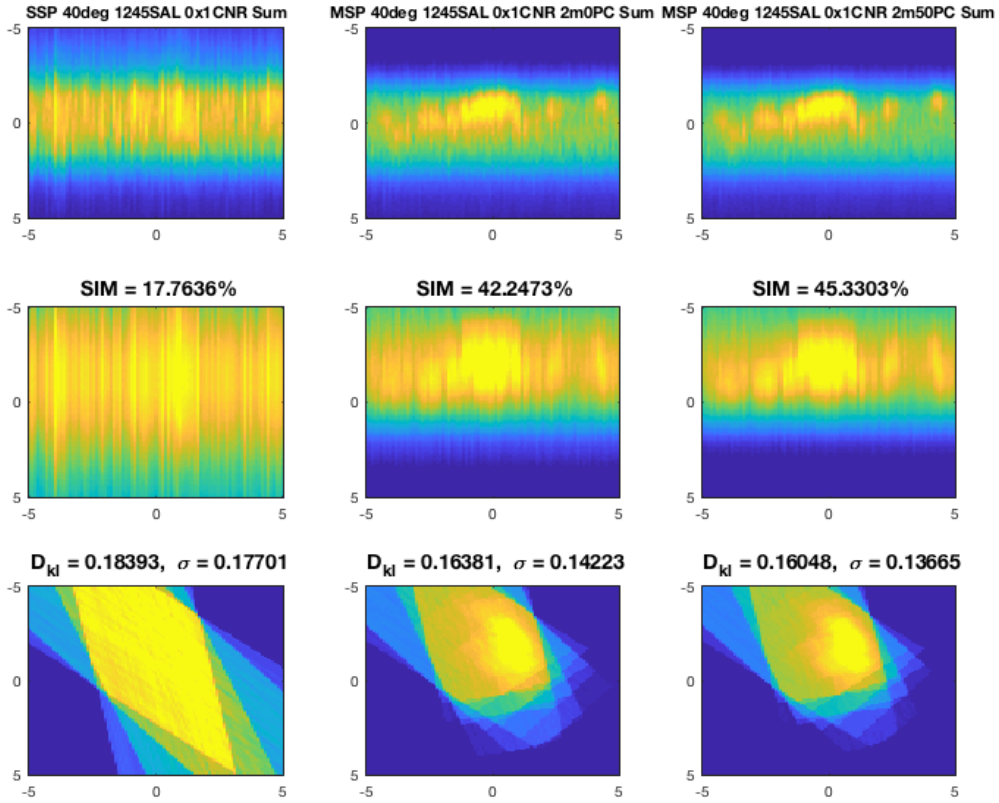


Figure 5.15: 2-D representative of the 3-D tomographic reconstruction of the backhoe using four projections with $40^\circ$ angular diversity and 0.1dB CNR.

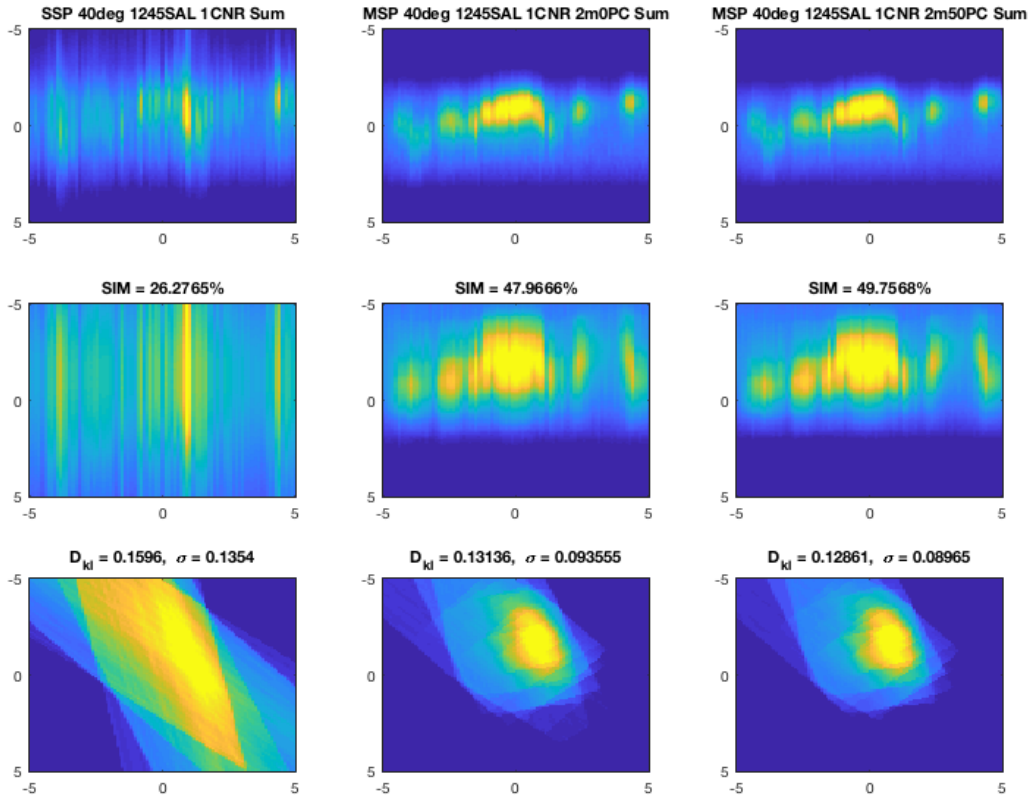


Figure 5.16: 2-D representative of the 3-D tomographic reconstruction of the backhoe using four projections with $40^{\circ}$ angular diversity and 1dB CNR.

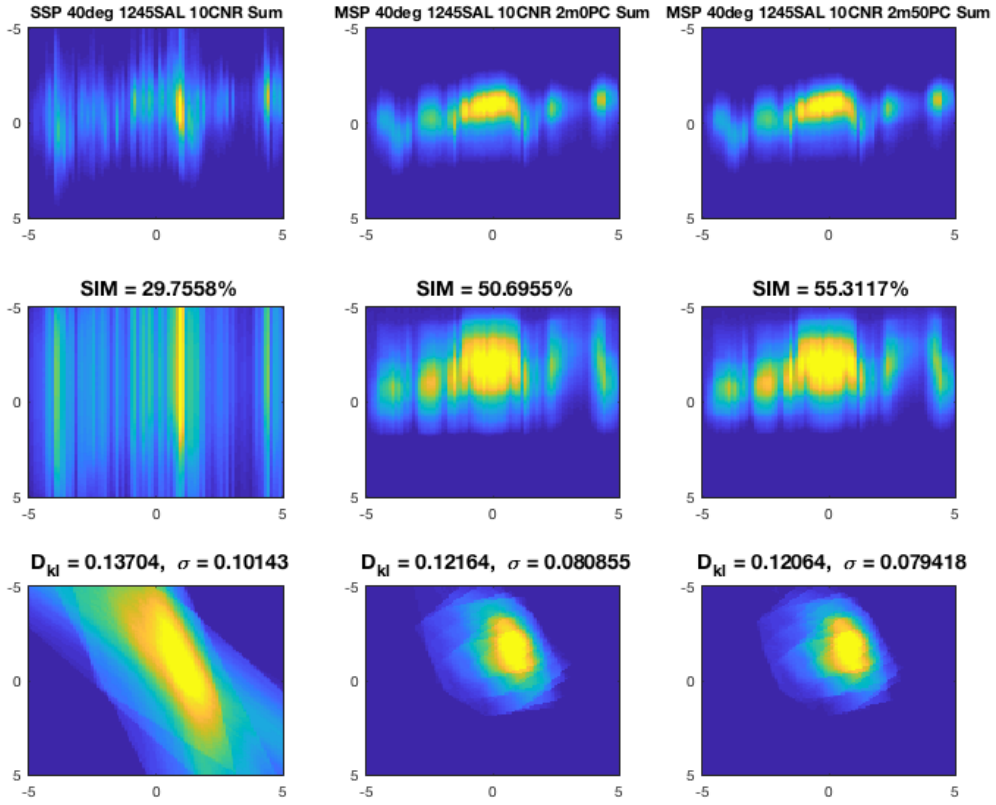


Figure 5.17: 2-D representative of the 3-D tomographic reconstruction of the backhoe using four projections with $40^{\circ}$ angular diversity and 10dB CNR.

# CHAPTER 6

# Results and Conclusion

In this chapter, we discuss the results obtained in this thesis, and give a detailed conclusion and suggestion for future work.

## 6.1 Results and Discussion

To quantify observed changes in the reconstruction images, the similarity metric and the joint information density metric defined in equations 5.5 and 5.6, respectively are used. As defined earlier the similarity metric calculates the amount of mutual information between two random variables; and the joint information density calculated the amount of useful information in the reconstructed volume.

In this results section, we run various experiment to show how each parameter such as, angular diversity, number of observation, overlap between the detectors, noise level and slant plane spacing affects the reconstructed image. These experiments were done for both the unstructured target and structured target shown in Figure 3.2 and 4.3. The structured target presents structured information preferring certain look angles whereas the unstructured target does not. For the unstructured target at each observation angles all points of the point cloud are visible to the sensor receiver. The targets are rendered at five

observation angles, ranging between $10^\circ$ to $60^\circ$ elevation angle with increment of $10^\circ$.

**Similarity vs. angular diversity experiment for the structured target results**

In this experiment, we study the way the similarity between the truth and the reconstructed image is affected as the angular diversity between the observation angles is varied. Two projections angle was used for each reconstructed image ranging between $10^\circ$ to $60^\circ$. At each angular diversity, the SAL image of the target is created for all possible combinations using the single slant plane and multiple slant plane methods with and without overlap. We then project the data with incoherent tomographic synthesis into image planes to reconstruct a 3-D image of the target. At each observation angle, we observe different features of the target that may contain different information. Therefore, the amount of information in the 3-D synthesized object changes. In this experiment, we average the similarity for all synthesized 2-D images of the 3-D objects for all possible combinations of angles between $10^\circ$: to $60^\circ$ degrees for the given angular diversity.

Figure 6.1 shows the similarity versus angular diversity plot. The black line represents similarities at each angular diversity when using the single slant plane method to reconstruct the data. The solid blue line represents similarities at each angular diversity when using the multiple slant plane method with $50\%$ overlap and $1m$ slant plane spacing to reconstruct the data. The dashed blue line represents similarities at each angular diversity when using the multiple slant plane method with $0\%$ overlap and $1m$ slant plane spacing to reconstruct the data. From Figure 6.1, we observe that the similarity between the truth image, and the reconstructed image increases as the angular diversity is increased. Furthermore, from Figure 6.1, we can see that higher similarity is obtained when using the multiple slant plane method. The similarity is even higher when we have $0\%$ overlap between the detectors.

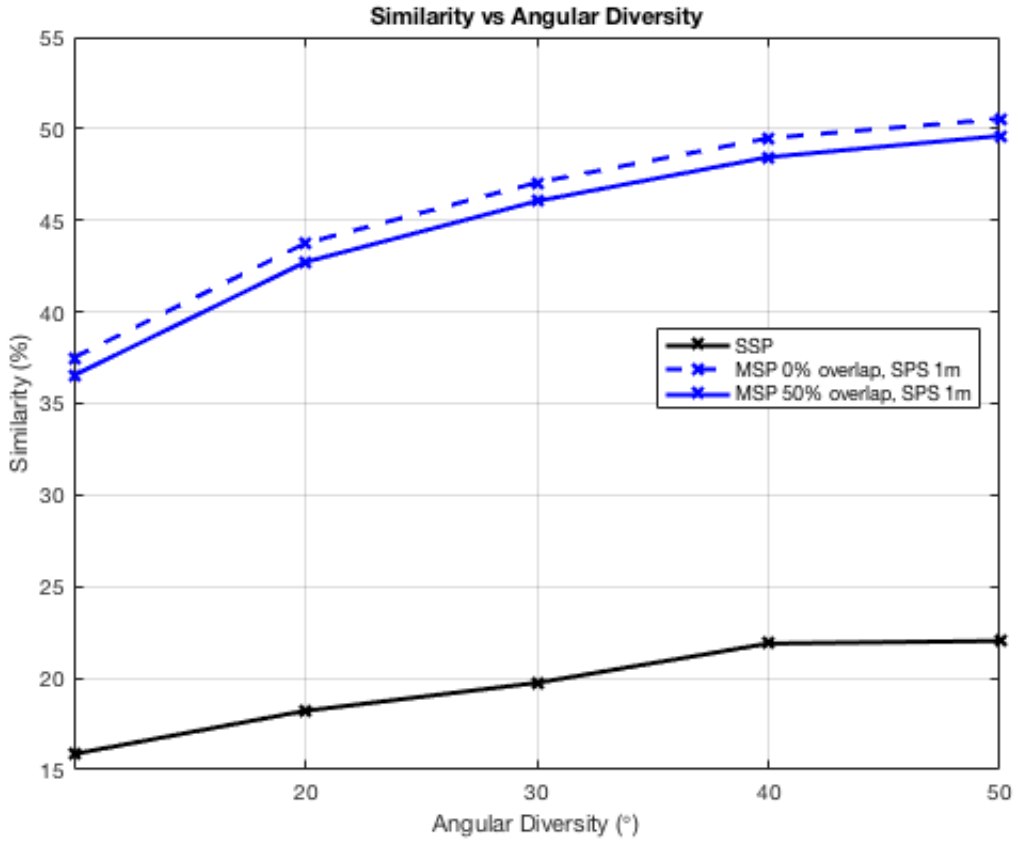


Figure 6.1: Backhoe Target: Similarity vs. Angular Diversity ,1dB CNR.

For the following experiment, we investigated the effect of slant plane spacing between the detectors on the similarity for the multiple slant plane method. Two projections angle was used for each reconstructed image ranging between $10^{\circ}$ to $60^{\circ}$. At each angular diversity, the SAL image of the target is created for all possible combinations using the multiple slant plane method. Figure 6.2 shows the effect of the slant plane spacing on the similarity between the truth image and the reconstructed image. The black line represents similarities at each angular diversity when using the single slant plane method to reconstruct the data. It is the same as in Figure 6.1. The green, blue and red lines represent similarities at each angular diversity when using the multiple slant plane method with $50\%$

overlap and $\frac{1}{2}m$, $1m$ and $2m$ slant plane spacing, respectively. We observed from Figure 6.2 we observed that the smaller the spacing between the slant planes are the higher the similarity. This is because the smaller the slant plane spacing, the smaller the slant plane height and the more transmitters and detectors are required to illuminate the whole target and receive the return signals.

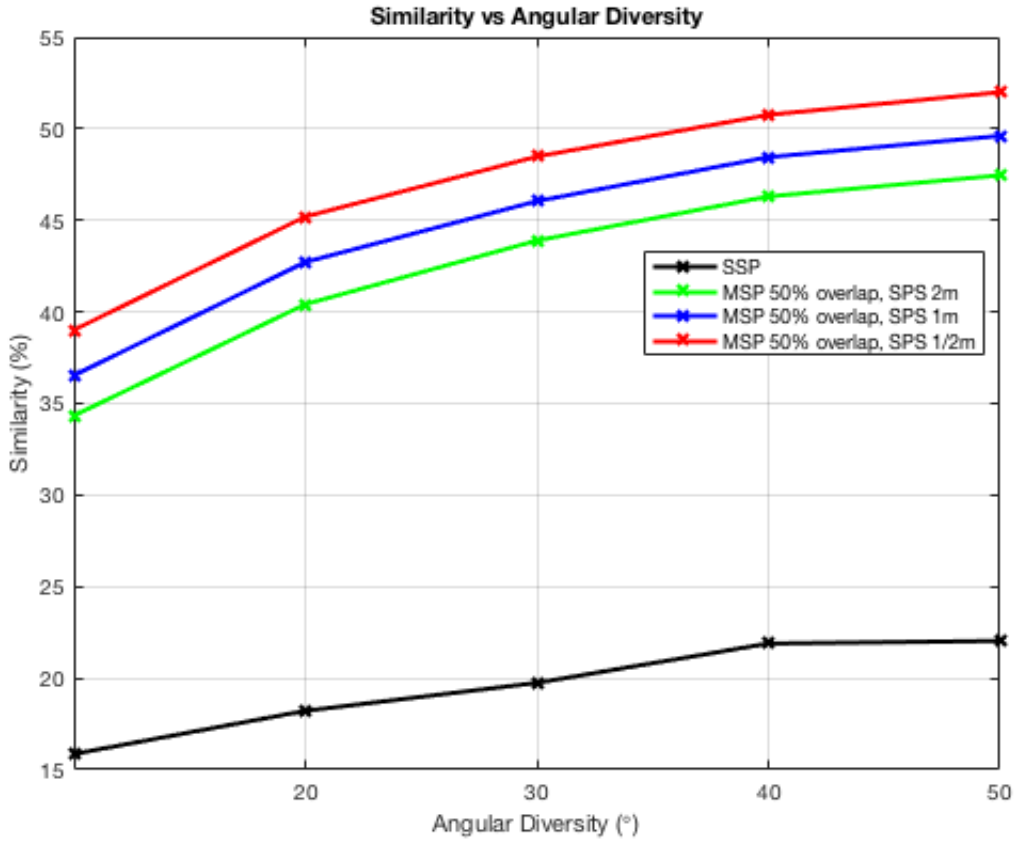


Figure 6.2: Similarity vs. Angular Diversity, 1dB CNR.

**Similarity vs. angular diversity experiment for the unstructured target results**

The same studies that was done for the backhoe target were done for the random point target. Figure 6.3 shows the effect of angular diversity on the random point target data.

Angular diversity doesn't have much effect on the random point target data, because the point target used in this research was generated in such a way that at each observation angles all the points in the data are visible to the sensor. At each angular diversity or observation angles the sensor sees the same points. Therefore, none new information is added when we look at the data at different angle. We also observed that the multiple slant plant method gives as higher similarity.

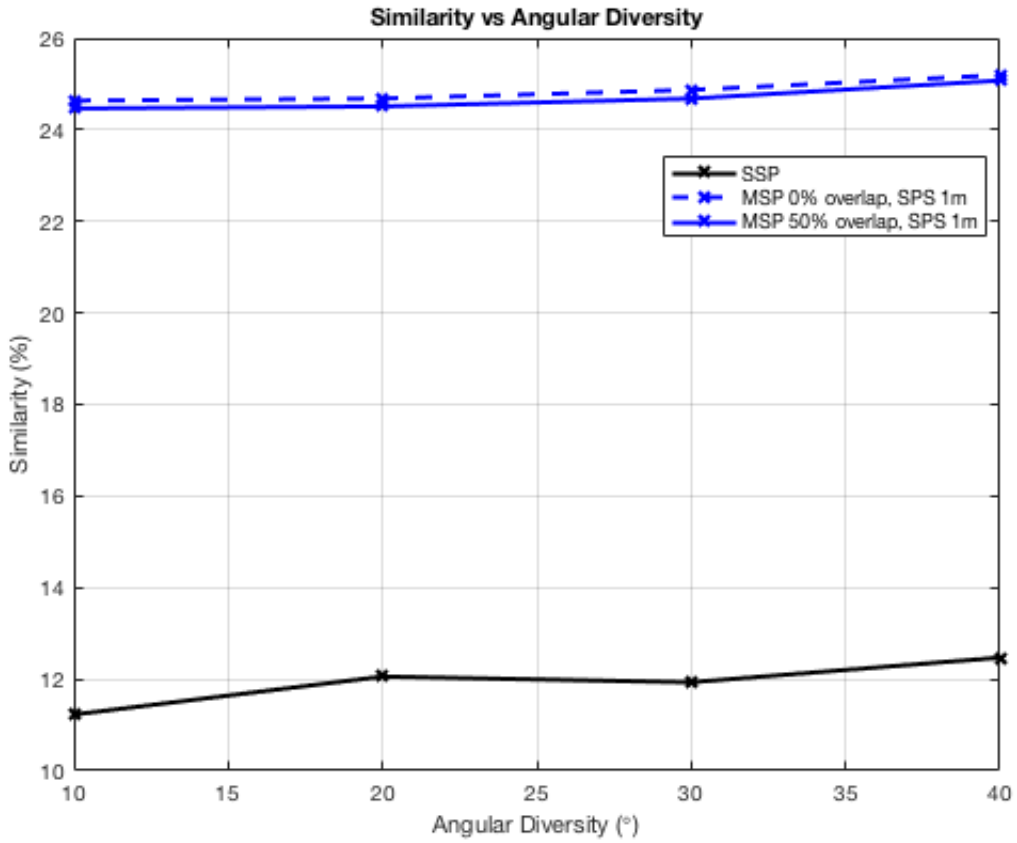


Figure 6.3: Backhoe Target: Similarity vs. Angular Diversity, 1dB CNR.

In Figure 6.4, we study the effect of the slant plane spacing on the point target as we did on the backhoe data. The black line represents similarities at each angular diversity when using the single slant plane method to reconstruct the data. The green, blue and red

lines represent similarities at each angular diversity when using the multiple slant plane method with $50\%$ overlap and $\frac{1}{2}m$, $1m$ and $2m$ slant plane spacing, respectively. We observed from Figure 6.4 observed that the smaller the spacing between the slant planes are the higher the similarity. We can see that for the point target, slant plane spacing has more effect than angular diversity

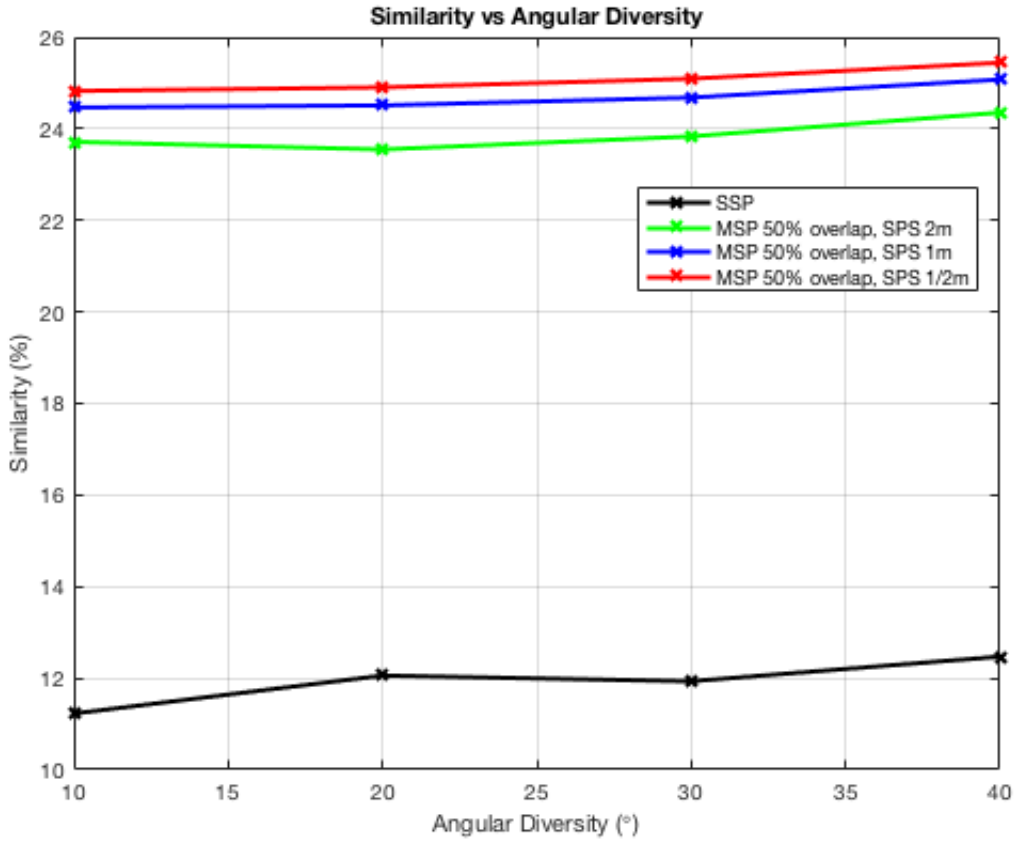


Figure 6.4: Backhoe Target: Similarity vs. Angular Diversity, 1dB CNR.

**Similarity vs. CNR experiment for the structured target results**

In this experiment, we investigate the effect of CNR on the similarity between the truth image and the reconstructed image. After simulating the 2-D SAL image of the target, a random additive Gaussian noise was added to the SAL image before projected it into the synthesized plane of the 3-D grid. The variance of the noise is inversely proportional to the CNR as show in Equation 3.14. We ran this experiment with various levels of CNR to observe the way the similarity is affected.

In Figure 6.5 we have the similarity versus angular diversity versus CNR for single slant plane method on top, multiple slant plane method with $0\%$ overlap in the middle and multiple slant plane with $50\%$ overlap at the bottom. Each colored line represents a different angular diversity as shown in the legend. From these results we can see that noises on the reconstructed image have a big effect on the resolution. We observe that as noise decreases similarity between truth image and the reconstructed image increases.

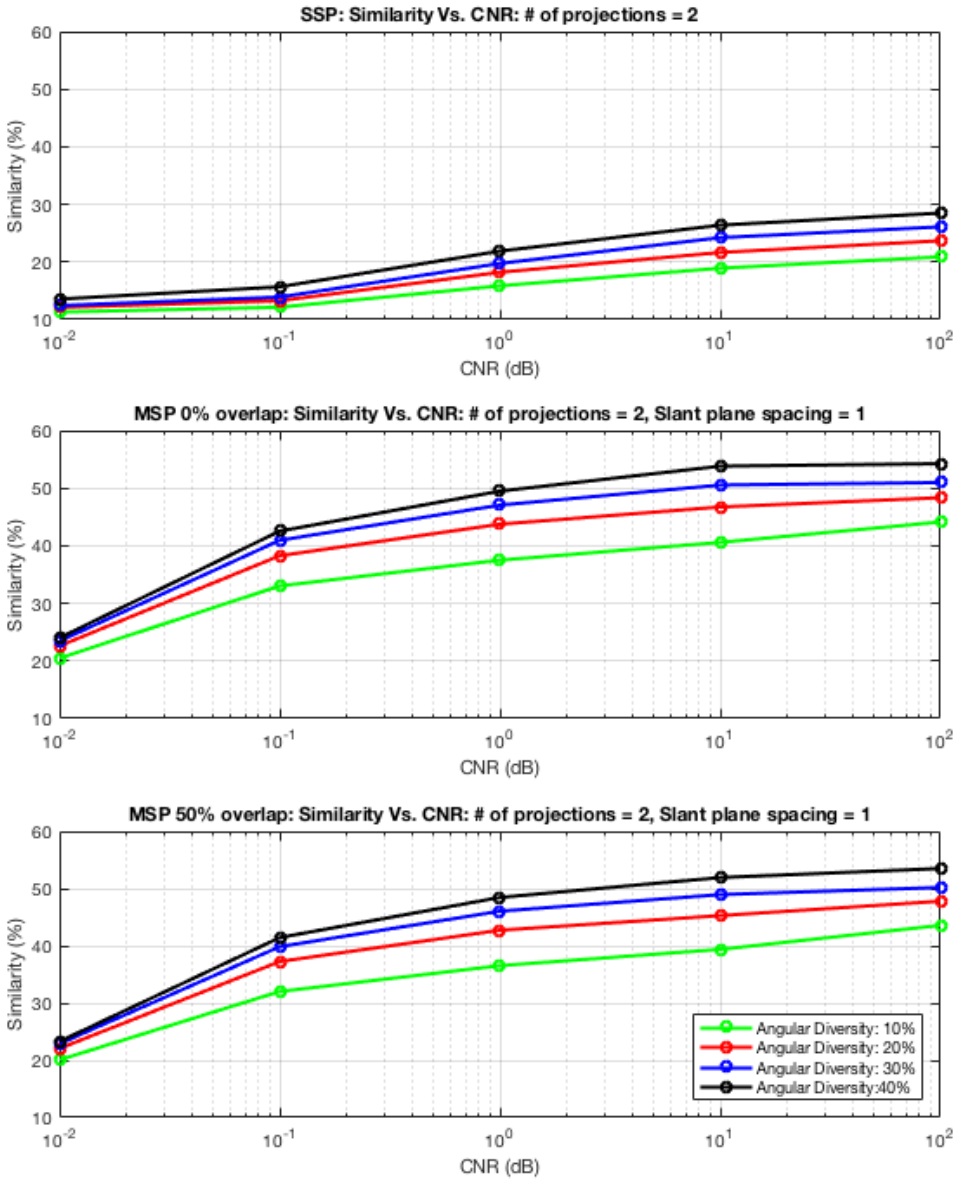


Figure 6.5: Backhoe Target: Similarity vs. CNR vs. Angular Diversity.

We know that all the information in the image is not useful, because it's a noisy image. We track the amount of useful information as show in Figure 6.6. From Figure 6.6, we observe that as we increase the CNR the amount of useful information or the joint information

density between the two images increases. This is because, when we project energy in the grid space, the information in the data goes up as a function of angular diversity.

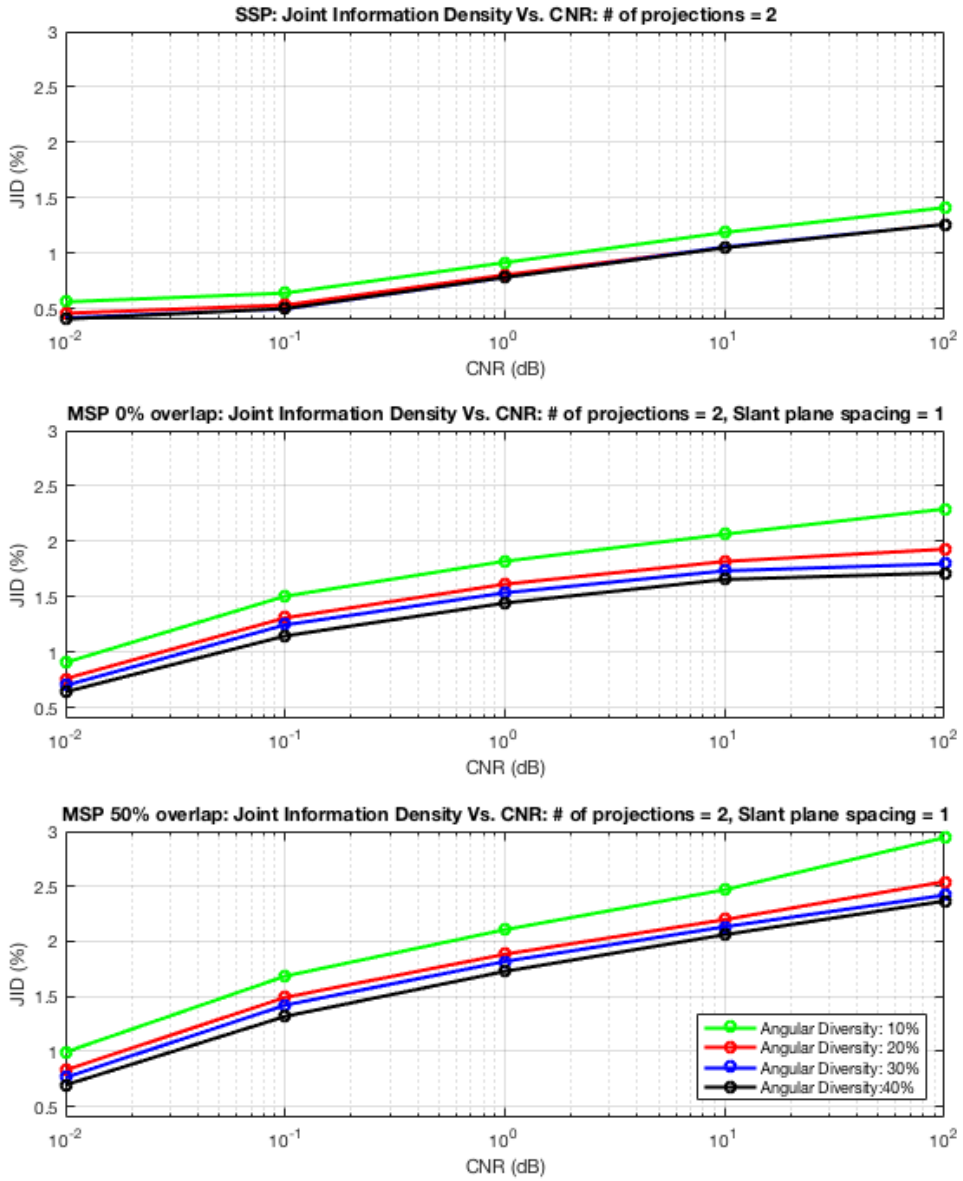


Figure 6.6: Backhoe Target: Joint Information Density vs. CNR vs. Angular Diversity.

**Similarity vs. CNR experiment for the unstructured target results**

The same similarity versus CNR study that was done for the backhoe target was done for the random point target. In Figure 6.7 we have the similarity vs. CNR result for single slant plane method on top, multiple slant plane method with 0% overlap in the middle and multiple slant plane with 50% overlap at the bottom. Each colored line represents a different angular diversity as shown in the legend. From these results we can see that noises on the reconstructed image have an effect on the similarity, but not as great of an effect when we compared to the structured target. Furthermore, we can see the angular diversity slightly helps in the case for the unstructured target.

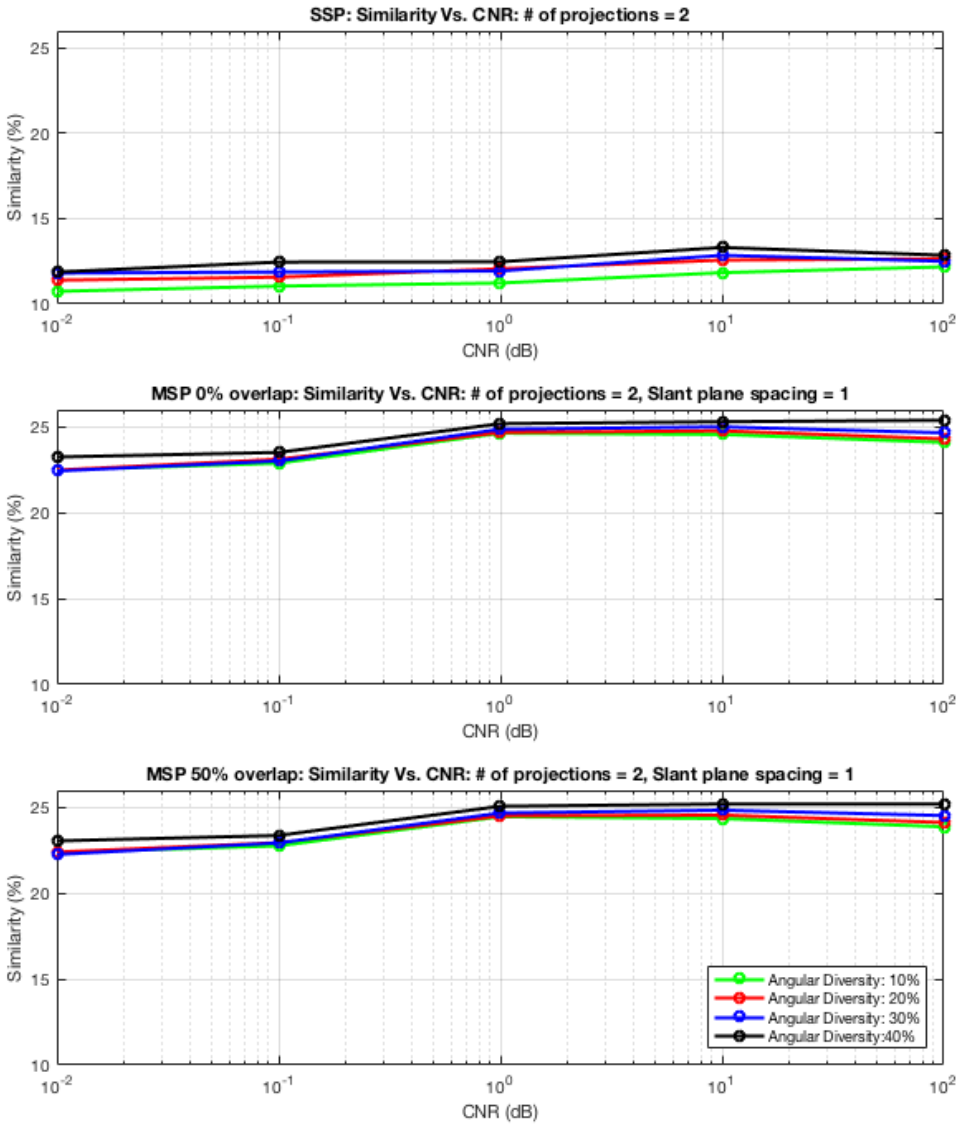


Figure 6.7: Point Target: Similarity vs. Angular Diversity vs. CNR.

In Figure 6.8, we tracked the joint information density, and we observed that as we increase the CNR the joint information density between the two images increases.

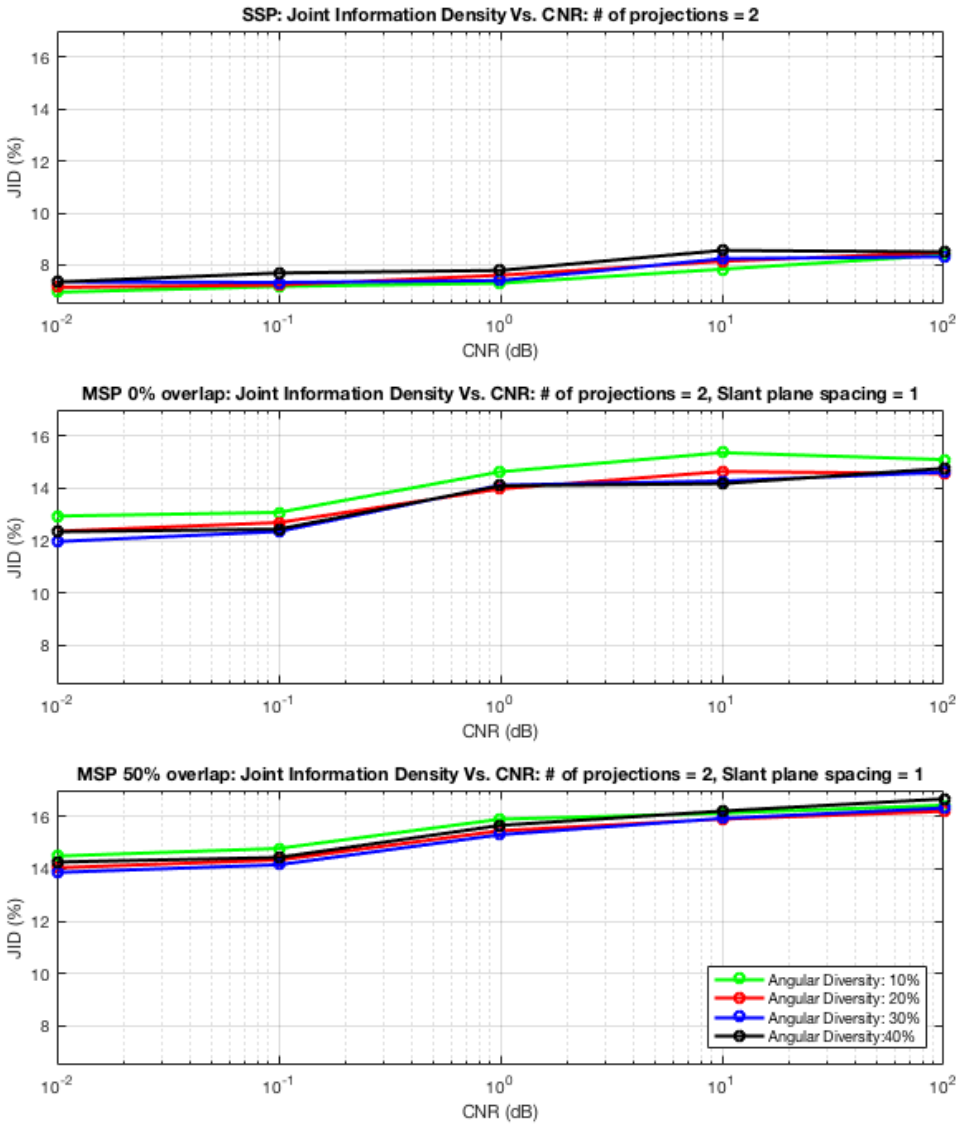


Figure 6.8: Point Target: Joint Information Density vs. Angular Diversity vs. CNR.

### 6.1.1 Kullback-Leibler divergence for the structured target

In this section we investigate the Kullback-Leibler divergence, and did similar experiments that was done for the similarity metric. The main purpose of this section is to show that the Kullback-Leibler divergence agrees with the similarity metric and track against qualitative assessments.

**Kullback-Leibler divergence vs. CNR experiment for the structured target results**

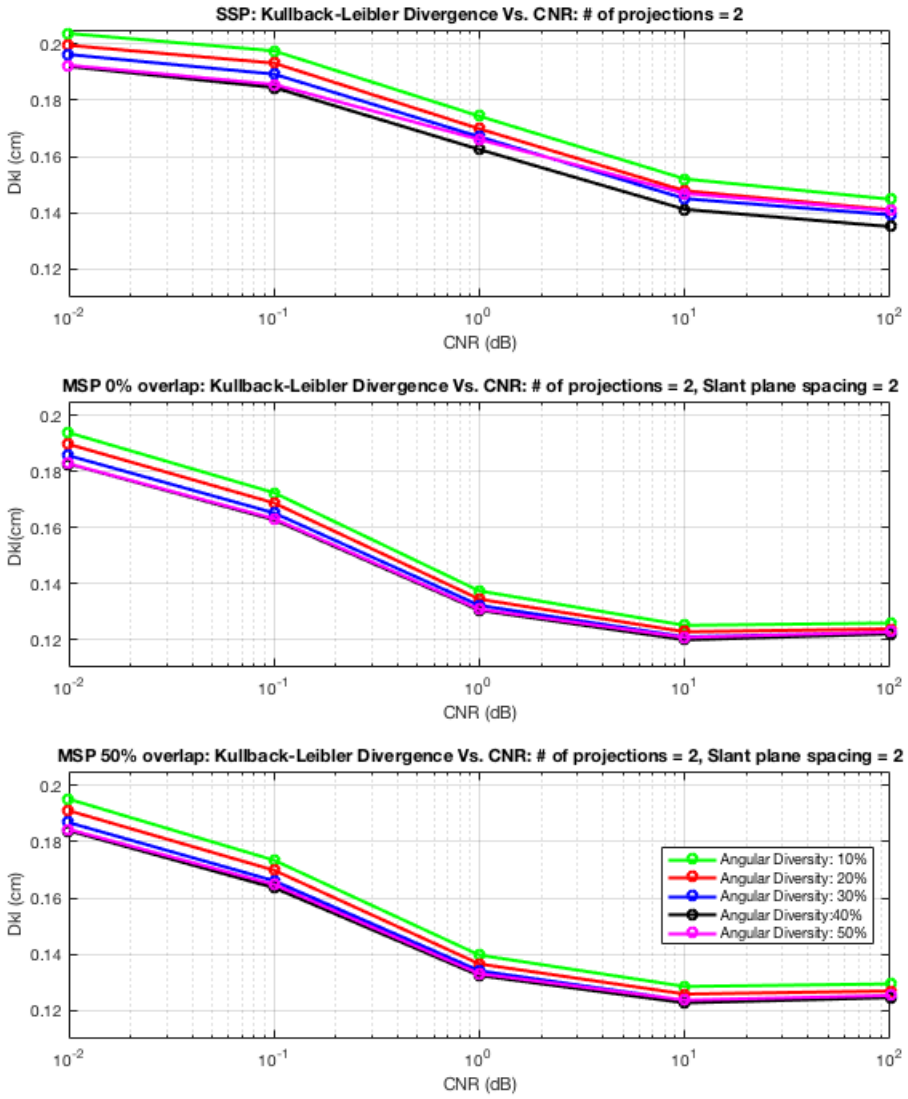


Figure 6.9: Kullback Leibler divergence vs. CNR.

In Figure 6.9 we have the Kullback-Leibler divergence vs. CNR for single slant plane method on top, multiple slant plane method with $0\%$ overlap in the middle and multiple slant plane with $50\%$ overlap at the bottom. Each colored line represents a different angular diversity as shown in the legend. From these results we can see that as we increase the CNR the Kullback-Leibler divergence decrease, meaning that we have a better reconstruction.

The lower the Kullback-Leibler divergence is, the better the reconstruction.

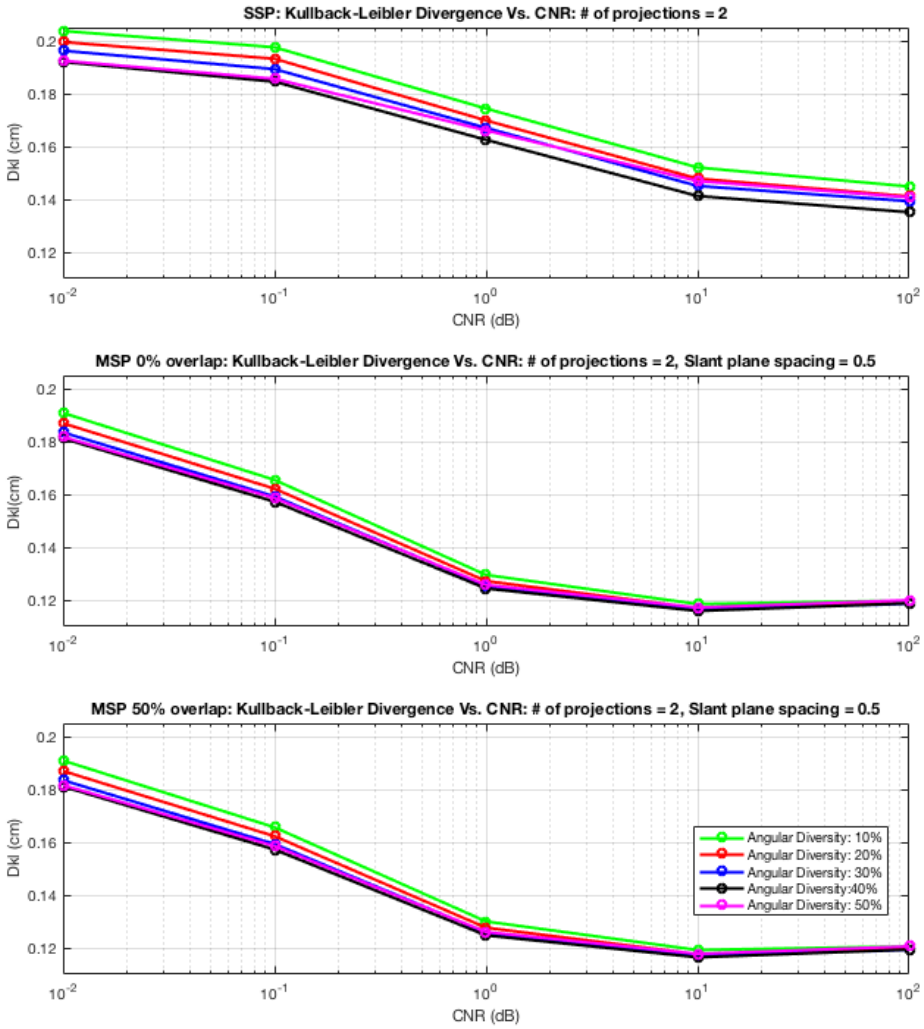


Figure 6.10: Kullback Leibler divergence vs. CNR.

In Figure 6.10, we change the slant plane height from $2m$ to $\frac{1}{2}m$. We observe that the Kullback-Leibler divergence decreases. This indicates that when the slant plane height is decreased, the reconstructed image is better resolve. From Figure 6.9, and Figure 6.10 we see that the Kullback-Leibler divergence and the Similarity metric agreed.

**Kullback-Leibler divergence vs. CNR experiment for the unstructured target results**

The same study was done for the unstructured target, and these results we sees that Kullback-Leibler divergence agrees with the similarity metric.

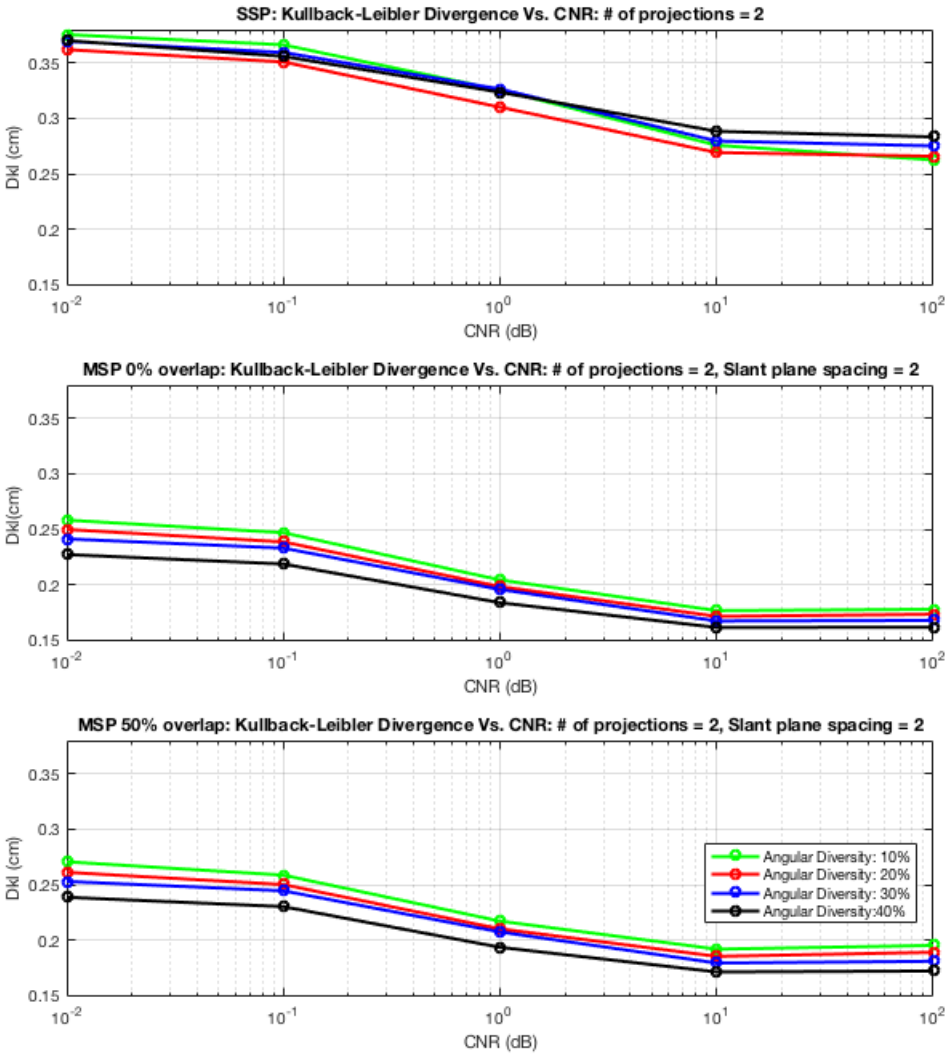


Figure 6.11: Kullback Leibler divergence vs. CNR.

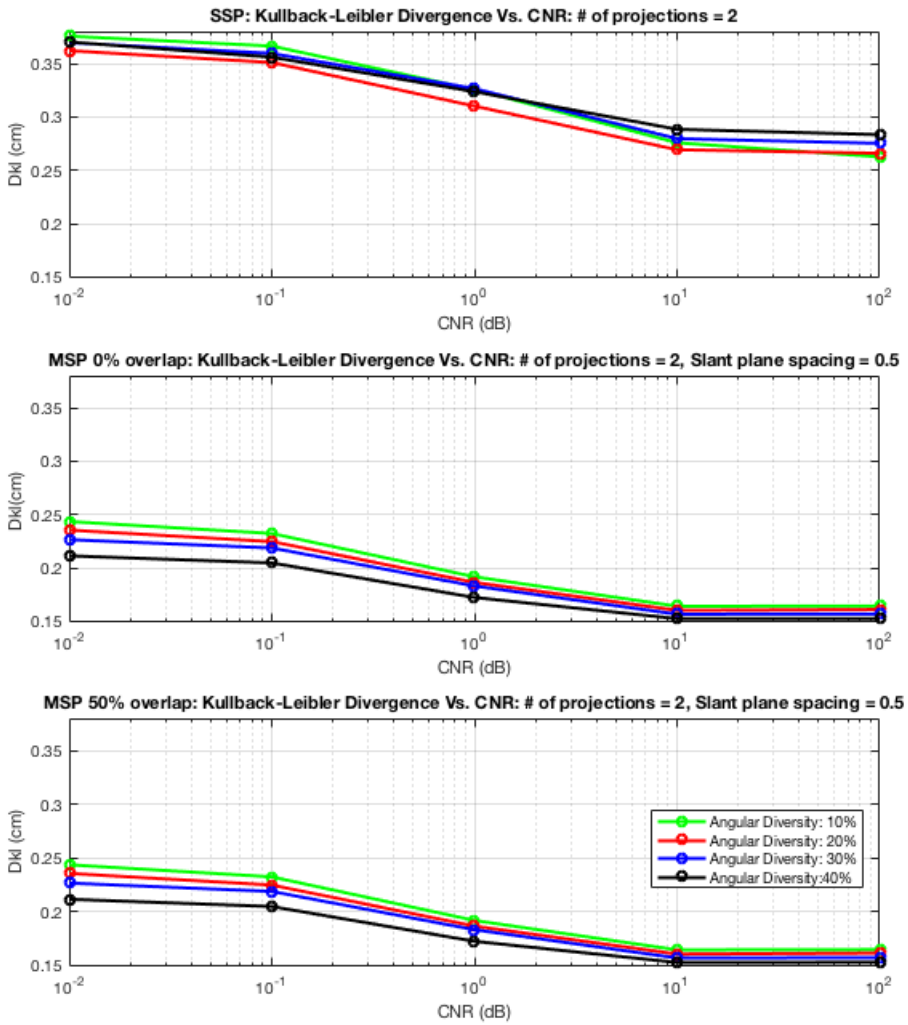


Figure 6.12: Kullback Leibler divergence vs. CNR.

## 6.2 Conclusion

SAL is a coherent imaging technique that exploits angular diversity between aperture position and target position to synthesize an aperture much larger than the physical antenna aperture along the baseline created by the angular diversity. The SAL's relatively narrow

real aperture resolution allows for multiple slant planes to be created for a single target with reasonable range/aperture combinations. It can also be displayed as a 3-D image with asymmetric resolutions, diffraction limited in the dimension orthogonal to the SAL baseline. Tomographic reconstruction of slant plane data with multiple observations and increased angular diversity can be used to better resolve the diffraction limited dimension of the data.

We use incoherent tomographic reconstruction and develop metrics to measure the efficacy of the reconstructions. Giving sufficient CNR, slant plane spacing has the greatest impact on the fidelity of the reconstructions, because it resolves individual SAL images with better diffraction limited resolution. Angular diversity between the SAL images, has the next greatest impact in the fidelity of the reconstructions. Number of projections and slant plane overlap have lesser impacts on the fidelity of the reconstructions.

The metrics that were developed in this work are the similarity metric and the joint information density metric. The similarity metric measures the similarities between two random variables. It is the ratio of the mutual information of the truth and the reconstructed image, and the entropy of the truth. It is also spatially depended, requiring registration of the images prior to calculating the metric. The joint information density tracks the amount of useful information in the data when varying the CNR. It is the ratio of the mutual information of the truth and the reconstructed image, and the entropy of the reconstructed image. Furthermore, we implemented the Kullback-Leibler divergence and compared it to the similarity metric. From this work we see that the similarity metric and the Kullback-Leibler divergence agreed.

The slant plane spacing has the greatest effect on the fidelity of the tomographic reconstruction. As the slant plant spacing is decreased, more slant planes are required to receive the backscattered signals of the entire target. Because this is a diffraction limit effect, we would be required to be at a closer range or use a larger receiver aperture. Decreased slant plane spacing increases the amount of information in the slant plane data for

a given elevation angle or observation.

Angular diversity between the SAL slant planes, has the next greatest impact in the fidelity of the reconstructions. When the angular diversity is increased, more unique information is being projected into the tomographic synthesize plane, enhancing the resolution on the diffraction limited dimension. Although, multiple observations within the angular diversity increases efficacy in tomographic reconstruction, however, the effect is minimal. Therefore, increasing the angular diversity while decreasing the number of projection angles helps reduce the cost to reconstruct the target.

Incoherent tomographic reconstruction of slant plane data can be used to enhance resolution on the reconstruct 3-D images of target. Depending on the cost and the resolution required, parameters such as slant plane spacing, angular diversity, CNR and number of projections can be defined to achieve the desired results.

## 6.3 Future Work

Future work on this topic could include extending the tomographic reconstructions to non-planner reconstructions, evaluating automation target recognition (ATR) algorithms against the developed metrics, and extending this work with coherent polar format reconstructions.

The tomographic reconstruction can be extended to non-planner collections, by varying both the elevation and azimuth angles. Also evaluating the similarity metric, joint information density metric and Kullback-Leibler divergence with ATR algorithms results for target identification, feature extraction and segmentation could show the benefit of these metrics. Furthermore, this work can be extended with coherent polar format algorithms to perform 3-D image reconstructions as mentioned in Jackowatz [11].

# Bibliography


[1] Z.W. Barber and J. R. Dahl. Synthetic aperture ladar imaging demonstrations and information at very low returns levels. *Optical Society of America*, 53(24):5531, 2014.

[2] R. Bobb. Doppler shift analysis for a holographic aperture ladar system doppler shift analysis for a holographic aperture ladar system. Master's thesis, University of Dayton, May 2012.

[3] C. Changqing, Z. Xiaodong, F. Zhejun, and S. Lei. Study on key techniques for synthetic aperture ladar system. *SPIE*, 6829, 2007.

[4] T.M. Cover and J.A. Thomas. *Element of Information Theory*. John Wiley and Sons, Inc., Hoboken, New Jersey, 2nd edition, 2006.

[5] A. Doerry. Catalog of window taper functions for sidelobe control. Technical Report 133, Sandia National Laboratories, April 2017.

[6] A. F. García-Fernández, O. A. Yeste-Ojeda, and J. Grajal. Facet model of moving targets for isar imaging and radar back-scattering simulation. *IEEE TRANSACTIONS ON AEROSPACE AND ELECTRONIC SYSTEMS*, 46(3):1455–1456, July 2010.

[7] R. Ghavamirad, H. babashah, and M. Sebt. Nonlinear fm waveform design to reduction of sidelobe level in autocorrelation function. *Iranian Conference on Electrical Engineering (ICEE)*, 25, 2017.

[8] W.J. Goodman. *Speckle Phenomena in Optics: Theory and Applications*. Roberts and Company Publishers, 2006.

[9] L.A. Gorham and L.J. Moore. Sar image formation toolbox for matlab. *Proc. SPIE*, 7699:7699–13, April 2010.

[10] K.H. Greenewald. Prediction of optimal bayesian classification performance for ladar atr. mater thesis, Wright State Univesity, 3640 Colonel Glenn Hwy, Dayton, OH 45435, August 2012.

[11] C V Jakowatz, D E Wahl, P H Eichel, D C Ghiglia, and P A Thompson. *Spotlight-Mode Synthetic Aperture Radar: A Signal Processing Approach*. JAN 1996.

[12] G. Li, N. Wang, R. Wang, Zhang K., and Y Wu. Imaging method for airborne sal data. 53(5):351, March 2017.

[13] C. D. Meinhart and S. T. Wereley. The theoty of diffraction-limited resolution in microparticle image velocimetry. *Research Gate*, pages 1049–1051, 2003.

[14] D.C. Munson, J.D. O'Brien, and W.K. Jenkins. A tomographic formulationof spotlight-mode synthetic aperture radar. *IEEE*, 71(8):917, August 1983.

[15] S. Ramahrishnan, V. Demarcus, J Le Ny, N. Patwari, and J. Gussy. Synthetic aperture radar imaging using spectral estimation techniques. Technical report, University of Michigan, April 2002.

[16] P.A. Roos, R.R. Randy, T. Berg, B. Kaylor, Z. Baber, and Randall B.W. Ultrabroad-band optical chirp linearization for precision metrology applications. *Optical Society of America*, 34(23):3693, December 2009.

[17] M. Rose. A history of the laser: A trip through the light fantastic. *Photonics Spectra*, May 2010.

[18] M. Skolnik. History of radar. *Enclyclopaedia Britannica*, April 2018.

[19] J. Stafford. *Range Compressed Holographic Aperture Ladar*. Dissertation, Unversity of Dayton, 300 College Park, Dayton, OH 45469, December 2016.